Linear and Nonlinear Optical Characterisation of Silicon Nanowire Structures

by

Sharon Mary McNicholas

A thesis submitted to the University of Dublin in satisfaction of the requirement for the degree of

Doctor of Philosophy

School of Physics,
University of Dublin, Trinity College.

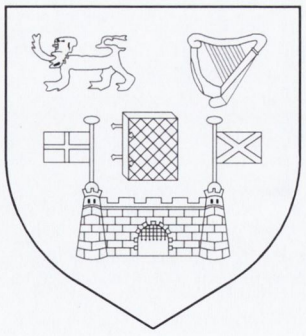

March 2008

Declaration

This thesis has not been submitted as an exercise for a degree at this or any other University and it is entirely my own work. I agree that the Library may lend or copy this thesis upon request; this permission covers only single copies made for study purposes, subject to normal conditions of acknowledgement. The copyright belongs jointly to the University of Dublin and Sharon Mary McNicholas.

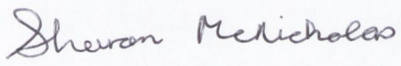

Sharon Mary McNicholas

Summary

The morphological and optical properties of various silicon nanowire structures were investigated. Photoluminescence was produced by all of the nanostructures and was attributed to a variety of different mechanisms.

Optical limiting capabilities were also demonstrated by the silicon nanostructures in isopropanol dispersions. The observed optical limiting has a strong contribution from non-linear scattering. It is likely that the non-linear scattering arises due to plasmas, which are formed by laser induced breakdown of the nanostructure's silicon oxide outer shells.

The nanowires that contained nanospherical inclusions showed additional interesting linear and non-linear optical properties. They exhibited an unusually strong, broad emission band in the violet region, that occurred for a wide range of excitation energies. This emission was attributed to a form of vibronic coupling, and may lead to biological cell imaging applications. They also exhibited enhanced optical limiting capabilities.

Acknowledgments

I would like to thank Prof. Werner Blau for his advice and for providing funding over the course of my Ph.D. studies. I would also like to gratefully acknowledge the support given to me by my parents through-out my college years.

Many thanks to Dr. Paul McNicholas for his statistical advice regarding the morphology and PL lifetime studies, and for lending me his expertise in LaTeX coding[1]. I would like to extend my gratitude to Dr. Shweta Chaure for her assistance in structuring my research, and to Dr. Satheesh Krishnamurthy for his analytical assistance and for his collaboration on research papers.

Sincere thanks to Dr. Hugh Byrne for arranging Raman and PL lifetime studies, and the procurement of additional TEM images when the TEM facility in Trinity College became non-operational. Thanks to Ms. Anne Shanahan for assisting me with Raman measurements and additional TEM images. My gratitude also goes to Dr. Alan Ryder for allowing me to perform PL lifetime measurements at his group's research facility.

Many thanks to Mr. James Doyle for familiarising me with the z-scan and the angular dependent scattering techniques. My appreciation goes to Dr. Valeria Nicolosi for her expertise in procuring some very nice HRTEM images. I would like to thank Mr. Alan Colli (and his supervisor Dr. Andrea Ferrari) for providing me with some very interesting samples, for EFTEM, EELS and additional HRTEM data.

My appreciation also to Dr. Eimhín Ní Mhuircheartaigh and Dr. John McCarthy for their support and encouragement. Thanks to Ms. Anna Drury for her assistance in proof reading this thesis. Finally, I would again like to thank my husband Paul for his enduring support and encouragement over the years.

[1] LaTeX was used to produce this document.

Publication List

The following publications have arisen from the work detailed herein. Please note that the articles were published under the author's maiden name, Sharon Mary King.

King, S. M., Chaure, S., Doyle, J., Colli, A., Ferrari, A. & Blau W. J., 'Scattering induced optical limiting in Si/SiO_2 nanostructure dispersions', *Optics Communications* **276** 305–309 (2007).

King, S. M., Chaure, S., Krisnamurthy, S., Colli, A., Ferrari, A. & Blau W. J., 'Optical characterisation of oxide encapsulated silicon nanowires of various morphologies', *Journal of Nanoscience and Nanotechnology* **8** (2008).

The following publication was a collaborative work.

Ní Mhuircheartaigh, E., Giordani, S., MacKernan, D., King, S. M., Rickard, D., Val Verde, L. M., Senge, M. O., & Blau W. J., 'Molecular engineering of nonplanar porphyrin and carbon nanotube assemblies: A linear and nonlinear spectroscopic and modeling study' (2007). Submitted.

Contents

List of Figures

List of Tables

Chapter 1

Introduction

1.1 Nanotechnology

1.1.1 History of Nanotechnology

Nanotechnology can be described as science on the nanometer scale, which is one billionth of a meter [1]. In practice, nanotechnology generally refers to the manipulation of materials and/or devices, less than 100 nm in size. Nanotechnology had unknowingly been utilised before the twentieth century, for example in making steel and vulcanized rubber. These processes rely on the properties of stochastically-formed atomic ensembles on the nanoscale. The first thought experiment in nanotechnology was carried out in 1867 by James Clerk Maxwell and involved an entity known as Maxwell's Demon which had the ability to handle individual molecules. Irving Langmuir and Katharine B. Blodgett introduced the concept of a monolayer in the 1920's, for which Langmuir won a Nobel Prize in chemistry [2].

Richard Feynman gave the now famous talk "There's Plenty of Room at the Bottom," at the American Physical Society meeting at Caltech on December 29,

1959 (the transcript of this talk is available [3]). Feynman introduced the idea of "scaling down" whereby nanoscale manipulation would be achieved by using one set of tools to build and operate another smaller set, and so on down to the nanoscale. He proposed that gravity would become less important, whereas Van der Waals attraction and surface tension would become more important as the scale became increasingly smaller. The now famous "Moore's Law" came about from an observation made by Gordon Moore in 1965 [2]. The law states that the number of transistors on an integrated circuit for minimum component cost doubles every 24 months.

The term "nanotechnology" came into use due to a paper written in 1974 by Norio Taniguchi. At first it was used just to describe processes on the atomic or molecular scale, but today it is used in relation to features up to 100 nm in size. In the same year, Tuomo Suntola patented atomic layer deposition for the production of thin films [2].

In the 1980s K. Eric Drexler wrote his influencial book "Engines of Creation; The Coming Era of Nanotechnology". In this book Drexler promotes the idea of nanomachines and "nanobots" that can manipulate individual atoms [4]. The feasibility of his predictions is debated. Nobel prize winner Richard Smalley called Drexler's approach to molecular assemblers "nieve". As well as debating the physics, Smalley also objects to unrealistic speculation regarding nanotechnology as it could cause misgivings in the public regarding its safety. They carried out a public debate on the topic in a series of open letters which were published in Chemical and Engineering News [5].

1.1.2 Applications of Nanotechnology

Medicine

Nanomaterials are being studied for use in cell imaging and targeting for the destruction of cells. Nanomaterials can be functionalised to interact with biological agents. The fact that some nanomaterials can fluoresce and/or absorb heat makes them auspicious components for the detection and destruction of cells such as cancer cells. Also, since the materials are on the nanoscale they can interact efficiently with the human body. For example, gold nanoparticles can be ligated to attach to cancerous cells. When the nanoparticles are heated using a laser of appropriate wavelength, they undergo surface plasmon resonance and the generated heat selectively destroys the cancerous cells, leaving the healthy cells almost completely undamaged [6].

"Lab-on-a-chip" technology is also under developement. Materials can become more sensitive to changes in their environment when they are on the nanoscale. Nanostructures can be functionalised to become sensitive to the presence of enzymes, proteins, or DNA sequences. Gold nanoparticles tagged with short segments of DNA can be made sensitive to a specific genetic sequence in a sample [7].

Side effects for a patent can be minimised if only the needed amount of drug is delivered, and delivered to the effected area directly. Active targeting is achieved by functionalising nanoparticles with ligands such as peptides, carbohydrates, antibodies, nucleic acid aptamers and small molecules [8]. Carbon nanotubes are being studied as a tool for a gene delivery vehicle [9, 10]. This is an intensively researched area and some of the therapies are at the clinical development stage [8]. As well as benefiting the patient by reducing side effects, it is claimed that targeted or personalized medicine will reduce drug consumption and treatment expenses [7].

Tissue engineering deals with structures or processes that can assist the body in repairing tissue. Porous silicon-based scaffolds have been fabricated that assist cell proliferation using bioactive mesoporous silicon and bioerodible polymers [11].

Information and Computing

Nanotechnology will play a crucial role in continuing the advances in miniaturisation and efficiency of computers. It will enable the fabrication of cleaner, stronger, lighter and more precise products. Modern day electronics is already on the nanoscale, with transistors sized at 50 nm and below [12]. In line with Moore's Law, miniaturisation of electronics continues at an unrelenting pace. As well as trying to miniaturise traditional silicon based electronics, Intel has been investigating what it referes to as "exotic" architecture. An example of such architecture is spintronics. Spintronics makes use of the quantum spin states of electrons as well as their charge state. The electron spin manifestes itself as a two state magnetic energy system. A spin polarised current can be created by sending the current through a ferromagnetic material. This can be used to create a giant magnetoresistance (GMR) device [13]. The magnetoresistance is enhanced for nanosized objects, for example when two ferromagnetic layers are separated by a nonmagnetic layer a few nanometers in diameter. GMR devices have greatly increased the data storage density of hard disks and has lead to gigabyte storage. Tunneling magnetoresistance (TMR) occurs due to spin dependent tunneling of electrons through adjacent ferromagnetic layers. GMR and TMR can be used in computers for non-volatile main memory, refered to as magnetic random access memory or MRAM [7].

Quantum computing promises to increased computing speeds exponentially. A quantum computer would make use of quantum mechanical phenomena, such as the

spin of an electron, to perform operations. Instead of "bits" of information, a quantum computer uses a quantum bit or qubit. The qubit arises due to quantum mechanics. A qubit can exist in a state corresponding to the logical state 0 or 1, and also in states corresponding to a superposition of these classical states. Hence the qubit can exist as a 0, a 1, or simultaneously as both 0 and 1, with the probability of occupation of each state represented by a numerical coefficient [14]. An example of a quantum computing system using quantum dots can be found in a paper by Daniel Loss and David P. DiVincenzo. This method involves utilising a set of one and two qubit gates using the spin states of coupled single-electron quantum dots. The necessary operations could be obtained by gating the tunneling barrier between neighboring dots [15].

Carbon Nanotube Applications

Carbon nanotubes are allotropes of carbon. A single wall carbon nanotube is equivalent to a rolled up sheet of graphene, capped on each end by half a buckyball (a spherical structure consisting of 60 carbon atoms). Carbon nanotubes have exceptional strength and unusual electrical properties, and are good heat conductors. The high strength and flexibility of carbon nanotubes means that they are promising materials for manipulating other objects on the nanoscale [9]. The highest recorded tensile strength of an individual multi-walled carbon nanotube is 63 GPa [16]. This strength doesn't scale up linearly to bulk dimensions, however composite materials containing carbon nanotubes show increased strength. Carbon nanotubes are being added to polymers to improve the thermal, mechanical and electrical properties of the material on the bulk scale. It has been shown that damascus steel contains carbon nanotubes, which may explain the legendary strength of swords made from it [16, 17].

It has also been shown that single and multi-walled nanotubes produce exceptionally tough materials [18, 19]. In the 2006 Tour de France, Floyd Landis rode a bike with a carbon nanotube reinforced carbon fiber frame. The whole bike's frame weighed just one kilogram [20]. Carbon nanotubes also have electrical applications. Transistors capable of single electron digital switching have been created using carbon nanotubes [21, 9].

1.1.3 Silicon Nanotechnology

Silicon nanostructures are auspicious components for nanoscale devices. This is partly due to the controllability of their growth, which provides some control over the morphology of the nanostructures. A variety of growth techniques allow parameters such as growth direction [22], thickness [23] and surface pacification to be controlled [22]. Zhang *et al* produced silicon nanowires using simple evaporation under argon gas [24]. They found that the average nanowire diameter was proportional to (the ambient pressure)$^{0.4}$. Hence silicon nanowires of a desired diameter could be produced by controlling the argon pressure. Wu *et al* claims to have achieved controlled growth using a chemical vapour deposition method with gold nanoparticle catalysts and silane gas [25]. Preferences for specific growth directions arise due to interfacial and surface energies produced during growth. For example, 95% of nanowires with diameters between 3 and 10 nm were formed along the (110) direction.

Silicon has the great advantage of being CMOS (complementary metal-oxide semiconductor) compatible. CMOS is the architecture that today's computers and microprocessors are built on. CMOS achieves high noise immunity and low static power supply drain. Power is only consumed when the transistors are switching between

on and off states. Hence CMOS devices do not produce as much heat as other forms of logic. CMOS is also designed to allow a high density of logic functions on a chip [26]. The miniaturisation of electronics means that the search for ever smaller components, especially transistors, receives much interest. Silicon nanowire transistors, due to their CMOS compatibility, are under developement [27]. They offer improved electrostatic control of the channel via the gate voltage and the consequent suppression of short channel effects [28], as well as increased miniaturisation.

The optical properties of silicon nanowires are of immense interest. They have the potential to act as optical inter-connects in an integrated circuit (IC). An efficient light emitter that is compatible with silicon based IC technologies is highly desirable [29]. Optical computing will allow for greatly increased processor speeds. It is envisioned that optical computers will use photons of light travelling along optical fibres and thin films, which will replace electronic circuits and wires that are currently used in computers. Optical computers, as well as being faster, will not need insulators as the components do not experience cross-talk. Photonic devices will alow light of different frequencies to travel simultaneously through the optical components, allowing multiple data streams to be processed simultaneously. Optical computers do not experience electromagnetic interference, have low losses and wide band width. They are also light weight and cheap to manufacture.

Hybrid electro-optic devices are currently in use, however their speed is limited by the electronic component of the device. They are very much in demand, as they can increase processing speeds while interfacing with standard electronic architecture [30]. A silicon based, efficient light emitter is highly desirable, as it would be compatible with CMOS technology. Silicon is a poor light emitter in its conventional form, and is not appropriate for used as a light source. Pavesi *et al* has reported light

amplification from silicon, by using quantum dots, 3 nm in diameter, dispersed in a silicon dioxide matrix [31]. A variable strip length method was utilised to measure the light amplification [32]. The optical gain was produced for waveguide and transmission configurations. The material gain was reported as being of the same order as that of direct bandgap quantum dots. The optical gain was attributed to population inversion of radiative states associated with the Si/SiO_2 interface. This brings the fabrication of a silicon laser significantly closer [31].

Silicon nanostructures are also under investigation for use in a biological and chemical sensors [33]. Silicon nanowires can be utilized for the sensing of DNA and proteins in electrolyte solution [34]. Due to its CMOS compatibility, silicon nanowires are important components for "lab on a chip" devices. Silicon nanowires in a microfluidic channel have been used to detect the interaction of anti-cancer drug Gleevec with its protein target [35].

Quantum dots are promising materials for replacing fluorescent dyes in biological fluorescence imaging [36, 37, 38, 39]. Table 1.1 lists the quantum efficiencies and emission ranges at room temperature of some quantum dot materials currently under investigation for biological applications. Although silicon quantum dots coated in oxide may not currently have quantum efficiencies as high as other quantum dots, they have the advantage of being non-toxic to humans, unlike other quantum dots studied to date such as CdSe dots with ZnS shells. Silicon quantum dots produce recombination rates appropriate for use in biological studies and can be made water soluble. The silicon oxide shell can also be modified easily, for example with glycans, for use in cancer detection [40].

Table 1.1: Luminescent quantum dots.

Material	% Yield	Emission Range
(CdS)Te	40 – 60	red – infrared [41]
(CdSe)ZnS	30 – 50	blue – red [42]
(Mn)ZnSe	40	red [43]
(Si)SiO_2	35	red [44]
PAAc grafted Si	24	red [45]

1.2 Thesis Outline

The motivation of this study was to characterise the morphological and optical properties of various silicon nanowire structures. Five different nanowire samples were investigated. Two of the samples consisted of spheres of nanocrystalline silicon encapsulated by silicon oxide nanowires. The remaining three samples contained crystalline silicon nanowires with silicon oxide shells. A selection of growth techniques was used to produce the structures. This study includes information on the morphologies produced by the various growth methods, linear and nonlinear optical properties of the silicon nanostructures.

This report contains detailed information on a wire structure referred to throughout this text as Sample A. The analysis of this sample was made possible by the continual availability of the sample from its supplier throughout the investigation process. Hence at the end of some of the characterisation chapters there is additional information supplied regarding Sample A. Sample A is also a very novel structure, as will be discussed in *Chapter* 4, *Structural Characterisation.* Hence the additional characterisation of this sample is of particular interest.

Bibliography

[1] Irish Council for Science, T. . I. I. *'The Science of Small Things' Press Release.* ICSTI, (2004).

[2] *Review of Nanotechnology,* `http://en.wikipedia.org/wiki/History_of_nanotechnology`, *accessed June 2007* .

[3] Goddard, W., Brenner, D., Lyshevski, S., and Lafrate, G. *Handbook of Nanoscience, Engineering and Technology, Transcript Section 1.1.* CRC Press, (2003).

[4] Drexler, K. E. *Engines of Creation; The Coming Era of Nanotechnology.* Anchor Books, New York, (1986).

[5] Drexler, K. E. and Smalley, R. E. *Chemical and Engineering News* **81**(48) (2003).

[6] Jain, P., H., E.-S. I., and El-Sayed, M. A. *Nanotoday* **2**(1) (2007).

[7] *Applications of Nanotechnology,* `http://en.wikipedia.org/wiki/List_of_nanotechnology_applications`, *accessed June 2007* .

[8] Gu, F., Karnik, R., Wang, A. Z., Alexis, F., Levy-Nissenbaum, E., Hong, S., Langer, R. S., and Farokhzad, O. C. *Nanotoday* **2**(3) (2007).

[9] *Carbon Nanotubes,* `http://en.wikipedia.org/wiki/Carbon_nanotube#Potential.2C_Current_and_Ancient_Applications`, *accessed June 2007* .

[10] Singh, R., Pantarotto, D., McCarthy, D., Chaloin, O., Hoebeke, J., Partidos, C. D., Briand, J.-P., Prato, M., Bianco, A., and Kostarelos, K. *Journal of the American Chemical Society* **127**(12) (2005).

[11] Coffer, J., Whitehead, M., Nagesha, D., Mukherjee, P., Akkaraju, G., Totolici, M., Saffie, R., and Canham, L. *Phys. Status Solidi A* **202**(8), 1451–5 (2005).

[12] Intel. *Intel Press Release* (2006).

[13] *Spintronics,* `http://en.wikipedia.org/wiki/Spintronics`, *accessed June 2007* .

[14] *Quantum Computing,* `http://www.cs.caltech.edu/~westside/quantum-intro.html`, *accessed June 2007* .

[15] Loss, D. and DiVincenzo, D. P. *Physical Review A.* **57**(1) (1998).

[16] Inman, M. *National Geographic News* (16 November 2006).

[17] Reibold, M., Paufler, P., Levin, A., Kochmann, W., Patzke, N., and Meyer, D. *Nature* **444**(7117) (2006).

[18] Zhang, M., Fang, S., Zakhidov, A. A., Lee, S. B., Aliev, A. E., Williams, C. D., Atkinson, K. R., and Baughman, R. H. *Science* **309**(5738) (2005).

[19] Dalton, A. B., Collins, S., Munoz, E., Razal, J. M., Ebron, V. H., Ferraris, J. P., Coleman, Jonathan N.and Kim, B. G., and Baughman, R. H. *Nature* **423**(6941) (2003).

[20] Kanellos, M. *CNET News.com* (7 July 2006).

[21] Postma, H., Teepen, T., Yao, Z., Grifoni, M., and Dekker, C. *Science* **292**(5527) (2001).

[22] Zhang, R.-Q., Lifshitz, Y., and Lee, S.-T. *Advanced Materials* **15**(7-8), 635–640 (2003).

[23] Wang, N., Zhang, Y., Tang, Y., Lee, C., and Lee, S. *Applied Physics Letters* **73**(26), 3902–4 (1998).

[24] Zhang, H., Yu, D., Ding, Y., Bai, Z., Hang, Q., and Feng, S. *Applied Physics Letters* **73**(23), 3396–8 (1998).

[25] Wu, Y., Cui, Y., Huynh, L., Barrelet, C., Bell, D., and Lieber, C. *Nano Letters* **4**(3).

[26] *CMOS,* `http://en.wikipedia.org/wiki/CMOS`, *accessed June 2007* .

[27] Canham, L., Cox, T., Loni, A., and Simons, A. *Applied Surface Science International Sympsoium on Si Heterostructures: From Physics to Devices, 11-14 Sept. 1995* **102**, 436–41 (1996).

[28] *The silicon nanowire transistor,* `http://monteverdi.iet.unipi.it/ fiori/snwthtml/node1.html`, *accessed June 2007* .

[29] Nihonyanagi, S. and Kanemitsu, Y. *Physica E International Conference on Superlattices Nano-Structures and Nano-Devices. ICSNN 2002, 22-26 July 2002* **17**(1-4), 183–4 (2003).

[30] Abdeldayem, H., Frazier, D. O., Paley, M. S., and Witherow, W. K. *Nasa Publications* .

[31] Pavesi, L., Negro, L., Mazzoleni, C., Franzo, G., and Priole, F. *Nature* **408**(6811) (2000).

[32] Shaklee, K., Nahaory, R. E., and Leheny, R. F. *Journal of Luminescnece* **7** (1973).

[33] Cui, Y., Wei, Q., Park, H., and Lieber, C. *Science* **293**(5533), 1289–1292 (2001).

[34] Bunimovich, Y. L. *PhD thesis,* `http://resolver.caltech.edu/CaltechETD:etd-05242007-151027` .

[35] Alper, J. *NCI Alliance for Nanotechnology in Cancer* **5** (2005).

[36] Bruchez, M., J., Moronne, M., Gin, P., Weiss, S., and Alivisato, A. *Science* **281**(5385), 2013–16 (1998).

[37] Dubertret, B., Skourides, P., Norris, D., Noireaux, V., Brivanlou, A., and Libchaber, A. *Science* **298**(5599), 1759–62 (2002).

[38] Chan, W. and Nie, S. *Science* **281**(5385), 2016–18 (1998).

[39] Larson, D., Zipfel, W., Williams, R., Clark, S., Bruchez, M., Wise, F., and Webb, W. *Science* **300**(5624), 1434–6 (2003).

[40] Warner, J. H., Hoshino, A., Yamamoto, K., and Tilley, R. D. *Angewandte Chemie - International Edition* **44**(29), 4550–4554 (2005).

[41] Bailey, R. E., Strausburg, J. B., and Nie, S. *Journal of Nanoscience and Nanotechnology* **4**(6) (2004).

[42] Dabbousi, B., Rodriguez-Viejo, J., Mikulec, F., Heine, J., Mattoussi, H., Ober, R., Jensen, K., and Bawendi, M. *Journal of Physical Chemistry B* **101**(46) (1997).

[43] Pradhan, N., M., D., Liu, Y., and Peng, X. *Nano Letters* **7**(2) (2007).

[44] Valenta, J., Juhasz, R., and Linnros, J. *Journal of Luminescence* **98**(1-4) (2002).

[45] Li, Z. and Ruckenstein, E. *Nano Letters* **4**(8) (2004).

Chapter 2

Crystallinity and Solid State Physics

2.1 Crystallinity

2.1.1 Introduction to Crystallinity

Materials in the solid state can be classified by the way in which their atoms are arranged. When the atoms are arranged randomly the material is classified as amorphous. If the atoms are positioned with a high degree of order the material is crystalline. Crystalline structures can be categorised by their lattice structure.

2.1.2 The Bravais Lattice

A lattice can be invariant under symmetry operations such as rotation through a certain angle, inversion and reflection. According to lattice classification by these criteria, there are 14 different types of lattice that can be used to describe any crystal

identified thus far. These are referred to as the 14 Bravais Lattices[1]. They are illustrated in Figure 2.1[2]

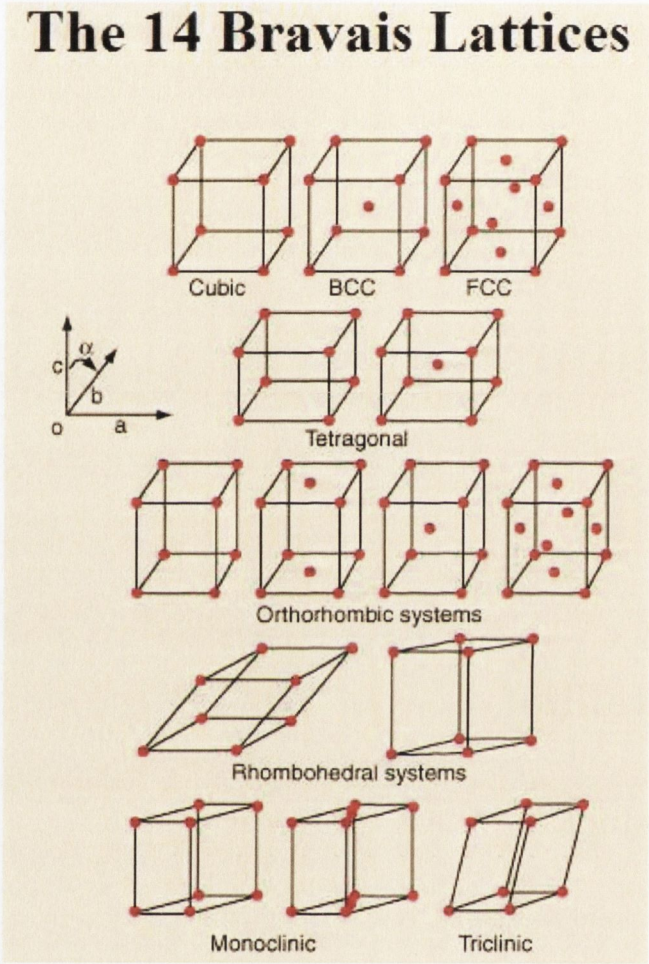

Figure 2.1: The 14 Bravais lattices.

2.1.3 Miller Indices

Miller indices are used to refer to the intercepts made by a plane on axes defined by a_1 a_2 and a_3. An (m_1,m_2,m_3) plane cuts the a_1 axis at a_1/m_1, the a_2 axis at a_2/m_2 and the a_3 axis at a_3/m_3[3]. This convention is illustrated in Figure 2.2[4]. In

crystallography it is customary to use (hkl) rather than (m_1 m_2 m_3). An example of various crystallographic planes of a cubic lattice defined by Miller indices is shown in Figure 2.3[5].

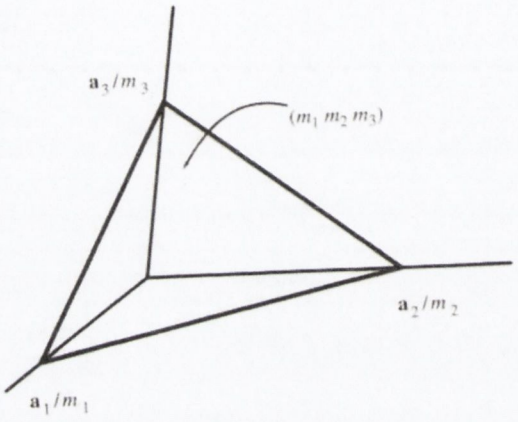

Figure 2.2: Miller indices.

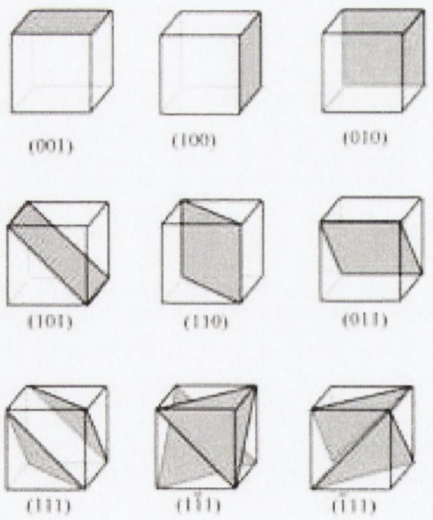

Figure 2.3: Crystallographic planes.

2.1.4 Brillouin Zones

A primitive cell is a unit cell of minimum volume. A Wigner-Seitz cell is a primitive cell that is centered around a lattice point, and reflects the symmetry of the underlying lattice. The first Brillouin zone is usually defined as the Wigner-Seitz cell of the reciprocal lattice. The reciprocal lattice undergoes periodicity in k space. All of the information about this reciprocal lattice is contained in the primitive unit cell of the reciprocal lattice, i.e., the first Brillouin zone [6].

2.1.5 The Reciprocal Lattice

The idea of a reciprocal lattice is useful for mathematical representations of planes within a crystal. For a three dimensional lattice defined by its' primitive vectors (a_1, a_2, a_3), its reciprocal lattice can be determined by generating its three reciprocal primitive vectors through the equations labelled 2.1. Reciprocal space is also referred to as Fourier space, k-space and momentum space[7].

$$\begin{aligned} b_1 &= 2\pi \frac{a_2 \times a_3}{a_1 \cdot (a_2 \times a_3)} \\ b_2 &= 2\pi \frac{a_3 \times a_1}{a_2 \cdot (a_3 \times a_1)} \\ b_3 &= 2\pi \frac{a_1 \times a_2}{a_3 \cdot (a_1 \times a_2)} \end{aligned} \tag{2.1}$$

2.1.6 Defects

Most crystalline materials contain a certain amount of defects. Point defects include vacancies, interstitials and impurities. Vacancies are sites which should be occupied by an atom but are unoccupied. Generally, the stability of the surrounding lattice

guarantees that the neighbouring atoms do not collapse around the vacancy. Interstitials are atoms which occupy a site in the crystal structure where there is not usually an atom. Impurity atoms are often incorporated at a regular atomic site in the lattice. They are therefore referred to as substitutional defects.

Dislocations are linear defects around which some of the atoms of the crystal lattice are misaligned. They result in lattice strain. There are two types of dislocation, edge and screw dislocations. Edge dislocations are caused by the termination of a plane of atoms in the middle of a crystal. A screw dislocation occurs when a helical path is traced around the dislocation line by the atomic planes of atoms in the lattice.

Planar defects include grain boundaries and stacking faults. Grain boundaries occur when the crystallographic direction of the lattice abruptly changes. A stacking fault is a one or two layer interruption in the stacking sequence of the crystalline layers that usually compose a regular sequence.

Bulk defects include voids and precipitates. A void occurs when there is a small region containing no atoms. They are equivalent to a cluster of vacancies. A cluster of impurities is referred to as a precipitate [8].

2.1.7 Amorphous and Crystalline Silicon

Silicon can occur in an amorphous or crystalline form. Amorphous silicon has no long range order and not all the atoms are four-fold coordinated. This leads to the presence of dangling bonds, which in turn can bond to impurity atoms.

Silicon crystallises in a diamond structure. It can be visualised as two interpenetrating face centered cubic lattices [9]. Each silicon atom is surrounded by four other silicon atoms, which it bonds to covalently. Figure 2.4 displays the diamond structure

of the unit cell. Figure 2.5 includes numbers indicating the height of each atom above the base of the cube as a fraction of the cell dimension [10].

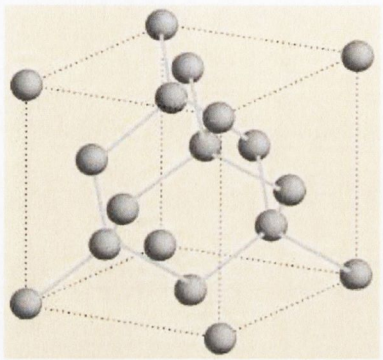

Figure 2.4: Diamond lattice structure of silicon.

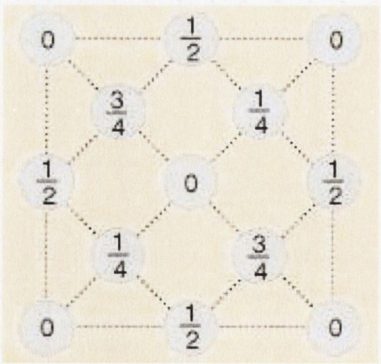

Figure 2.5: Arrangement of atoms in a unit cell of crystalline silicon.

2.2 Band Structure

2.2.1 The Fermi Level

The Fermi level is the top of the electron energy levels at absolute zero. The concept comes from Fermi-Dirac statistics, and from the Pauli exclusion principle whereby electrons cannot exist in identical energy states. Therefore at absolute zero the electrons occupy the lowest available energy states and build up a "Fermi sea" of energy states. At absolute zero, no electrons have enough energy to rise above the Fermi level. At temperatures above absolute zero a certain fraction of the electrons, characterised by the Fermi function, will exist above the Fermi level[11].

2.2.2 The Fermi Function

The Fermi function is obtained from the Fermi-Dirac distribution, which applies to fermions. A fermion is a particles with half-integer spin, which must obey the Pauli exclusion principle. Therefore electrons are an example of fermions. Each type of Fermi-Dirac distribution function has a normalization term multiplying the exponential in the denominator, which may be temperature dependent. The Fermi function is given by Equation 2.2,

$$f(E) = \frac{1}{e^{(E-E_F)/kT} + 1} \tag{2.2}$$

where f(E) is the probability that a particle will have energy E, E_f is the Fermi energy, k is Boltzmann's constant and T is the temperature in Kelvin.

At absolute zero there is a sizable gap between the Fermi level and the conduction band of a semiconductor. At higher temperatures, a fraction of the electrons can

bridge this gap. The population of electrons depends on the product of the Fermi function and the electron density of states. In the band-gap there are no electrons because the density of states is zero. In the conduction band at absolute zero, there are no electrons as the Fermi function is zero. At high temperatures, both the density of states and the Fermi function have finite values in the conduction band, so there is a finite conducting population.[1] Figure 2.6 illustrates the Fermi function of a semi-conductor as a function of temperature [13].

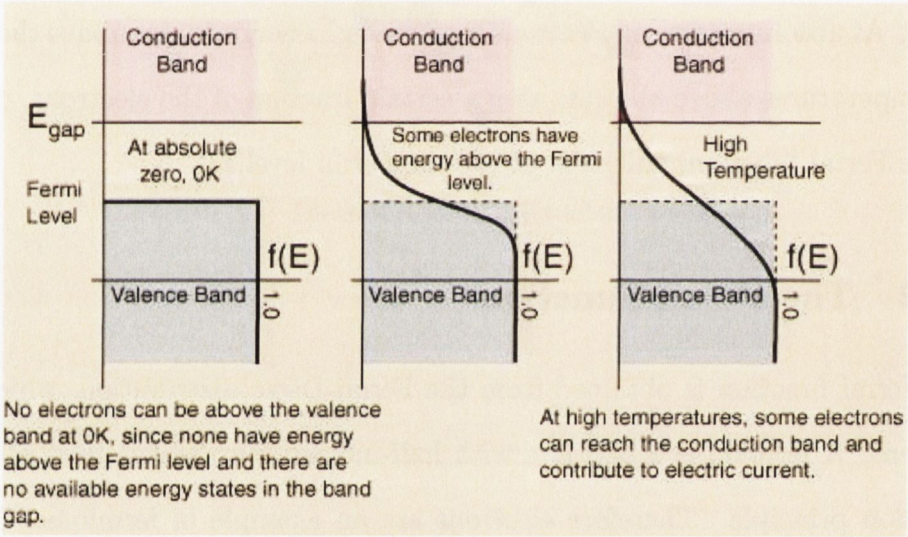

Figure 2.6: Bandgap of a semi-conductor.

2.2.3 Band Structure of Solids

The electronic and vibrational states of free atoms and molecules have discrete energies. In solids however, the electron and phonon (a quantized vibration) modes

[1]The explaination of the Fermi energy and Fermi function have been based on the treatment of the topic at hyperphysics.com[11] A more detailed explaination of the topic can be found in a work by John Singleton[12].

have a continuous range of energies, which gives rise to continuous absorption and emission bands. The density of states gives an indication of how closely packed the energy levels are, within a given energy range.

Due to the fact that atoms are closely packed in a solid, delocalisation of the electron states can occur. In a crystal, these delocalised states possess the underlying translational symmetry of the crystal. Delocalisation also allows collective excitation of the whole crystal. In terms of lattice vibrations, the delocalised excitations are described by phonon modes. Phonon modes are continuous, unlike the discrete vibrational frequencies of molecules. The delocalised states of a crystal are described by quantum numbers such as k, which have dimensions of inverse length [14].

2.2.4 Direct and Indirect Band-structure

Whether a semi-conductor has a direct band-gap or an indirect band-gap depends on the positions of the conduction band minimum and the valence band maximum in the Brillouin zone. For a direct band-gap material, both occur at $k = 0$, as shown in Figure 2.7 [15]. For an indirect band-gap material, the conduction band minimum does not occur at $k = 0$, as shown in Figure 2.8 [16]. The shaded regions of the valence and conduction bands indicate states that are occupied by electrons.

In a direct band-gap material, an electron can travel from the valence band to the conduction band by absorbing a photon of appropriate energy. However, for an indirect band-gap material, in order for an electron to make the transition from the valence band to the conduction band a phonon must also be involved in order to conserve momentum, as illustrated in Figure 2.8. This makes the transition of an electron from the valence band to the conduction band of an indirect band-gap

material highly unlikely [17].

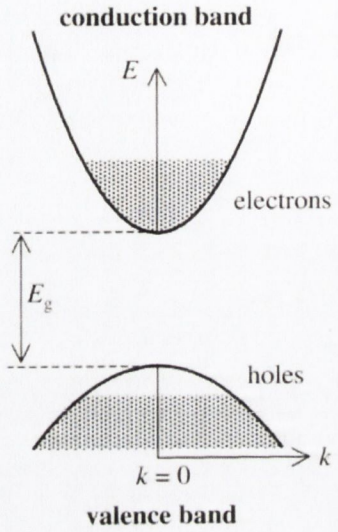

Figure 2.7: Direct band-gap semi-conductor.

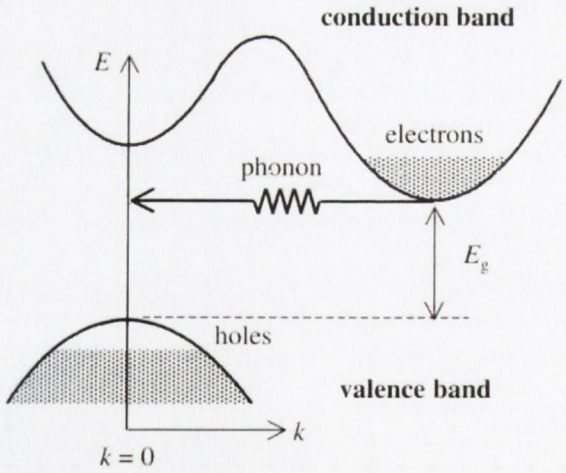

Figure 2.8: Indirect band-gap semi-conductor.

2.2.5 Silicon Band Structure

Figure 2.9 illustrates the band structure of silicon along the (100) and (111) directions[2]. Silicon is based on the diamond lattice structure, and the wave vectors at the X and L points are $k = \frac{2\pi}{a}(100)$ and $k = \frac{\pi}{a}(111)$ respectively, where a is the length of the cube edge of the face centered cubic lattice from which the diamond structure is derived [19].

Silicon has an indirect band-gap which shall be referred to as E_g, and has a value of 1.1 eV. It can be seen from Figure 2.9 that the conduction band minimum is located close to the X point of the Brillouin zone. The minimum direct separation between valence and conduction bands occurs close to the L point, between $L_3^{'}$ and L_1, and has a value of 3.5 eV. This shall be referred to as E_1 [20]. The separation of the bands close to the X point is also significant and is quoted as being 4.4 eV. This band separation shall be referred to as E_2.

Close to the L and X points the conduction and valence bands are almost parallel to each other. Therefore direct transitions can occur with the same photon energy, for many different values of k. The joint density of states is therefore very high at these regions. Absorption by silicon should be correspondingly strong close to E_1 and E_2 [20]. This will be discussed in detail in *Chapter* 6, *Linear Optical Characterisation I.*

[2]Figure 2.9 sourced from Band Theory and Electronic Properties of Solids by John Singleton, p. 51, based on work by M. Cardona and F. Pollack [18].

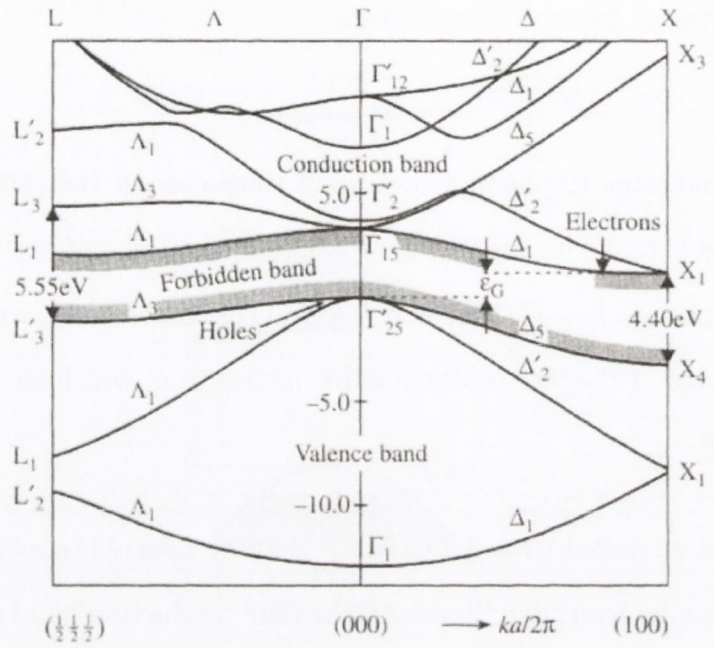

Figure 2.9: Band structure of silicon.

2.3 Quantum Mechanics

An understanding of quantum mechanics is necessary when working on the nanoscale. Some basic, useful concepts are outlined in this section.

2.3.1 The Time-dependent Schrödinger Equation

Particles such as electrons can display wavelike behaviour. In one dimension, the wave-vector and momentum of a particle can be expressed as scalars. The de Broglie relations can be represented as

$$E = \hbar\omega \tag{2.3}$$

and

$$p = \hbar k \tag{2.4}$$

where E is the energy of the particle, $\hbar$ is Planck's constant (h) divided by 2π, and ω is the angular frequency ($2\pi v$ where v is the frequency).

For a classical wave moving in the x direction, its displacement at the point x at time t is given by the real part of the complex quantity A where

$$A(x,t) = A_0 e^{[i(kx-\omega t)]} \tag{2.5}$$

This expression is the solution to a wave equation. A form of wave equation relevant to many classical waves is

$$\frac{\delta^2 A}{\delta x^2} = \frac{1}{c^2}\frac{\delta^2 A}{\delta t^2} \tag{2.6}$$

where c is a constant representing the wave velocity. By substituting the right hand side of Equation 2.5 into Equation 5.9 it becomes apparent that Equation 2.5 is a solution to Equation 5.9 if

$$-k^2 = \frac{-\omega^2}{c^2} \tag{2.7}$$

i.e.

$$\omega = c \mid k \mid \tag{2.8}$$

If Equation 5.10 is combined with equations 2.3 and 2.4 we get

$$E = cp \tag{2.9}$$

But for non-relativistic free particles the energy and momentum are known to be

$$E = \frac{p^2}{2m} \tag{2.10}$$

hence a relation of the form of Equation 5.9 cannot govern matter waves. As plane waves are associated with free particles, Equation 2.5 is a solution to an equation that can govern matter waves.

For the de Broglie relations and Equation 5.14 to be solved simultaneously, the frequency of the wave must be proportional to the square of the wave-vector, rather than the magnitude as stated in Equation 5.10. Consider an equation of the form

$$\frac{\delta^2\Psi}{\delta x^2} = \alpha\frac{\delta\Psi}{\delta t} \tag{2.11}$$

where α is a constant and $\Psi(x,t)$ is a wavefunction, which is a complex quantity. Substituting a plane wave of the same form as Equation 2.5 for Ψ produces a solution to Equation 5.15 if

$$-k^2 = -i\alpha\omega \tag{2.12}$$

The de Broglie relations and Equation 5.14 are therefore satisfied by defining α as

$$\alpha = \frac{-2mi}{\hbar} \tag{2.13}$$

If Equation 2.13 is substituted into Equation 5.15 and re-arranged, the wave equation for the matter waves of free particles is found to be

$$i\hbar\frac{\delta\Psi}{\delta t} = -\frac{\hbar^2}{2m}\frac{\delta^2\Psi}{\delta x^2} \tag{2.14}$$

This equation meets the requirements and can be checked by making Ψ equal to a plane wave as described in Equation 2.5 and by using the de Broglie relations to produce

$$E\Psi = \frac{p^2}{2m}\Psi \tag{2.15}$$

This approach can be extended to a particle moving under a potential $V(x,t)$. The total energy is equal to the sum of the kinetic and the potential energy, hence

$$E\Psi = (\frac{p^2}{2m} + V)\Psi \tag{2.16}$$

It is therefore possible that Equation 2.15 can be generalised to

$$i\hbar\frac{\delta\Psi}{\delta t} = -\frac{\hbar^2}{2m}\frac{\delta^2\Psi}{\delta x^2} + V\Psi \tag{2.17}$$

This is known as the one dimensional time dependent Schrödinger equation [21].

2.3.2 The Time-independent Schrödinger Equation

When the potential V of a system is not a function of time, then the one dimensional time-independent Schrödinger equation is applicable.

A separation of variables can be applied to the Schrödinger equation giving

$$\Psi(x,t) = u(x)T(t) \tag{2.18}$$

If Equation 2.18 is substituted into Equation 2.17 and divided by Ψ then the following is obtained

$$i\hbar\frac{1}{T}\frac{dT}{dt} = -\frac{1}{u}\frac{\hbar^2}{2m}\frac{d^2u}{dx^2} + V(x) \tag{2.19}$$

The left side of this equation is independent of x and the right side is independent of t. The equation must be valid for all values of x and t, which can only be true if both sides are equal to a constant. This constant shall be referred to as E. Hence

$$i\hbar\frac{dT}{dt} = ET \tag{2.20}$$

and

$$-\frac{\hbar^2}{2m}\frac{d^2u}{dx^2} + V(x)u = Eu \tag{2.21}$$

Equation 2.21 is the time-independent Schrödinger equation [22].

Boundary Conditions

Solutions to the time-independent Schrödinger equation must obey a number of boundary conditions.

1: The wave-function is a continuous, single valued function of time and position.

2: The integral of the squared modulus of the wave-function over all values of x is finite.

3: The first derivative of the wave-function with respect to x is continuous everywhere except where there is an infinite discontinuity in the potential [23].

2.3.3 The Infinite Square Well

Consider a square potential well with $V \rightarrow \infty$. The potential is

$$V(x) = 0, \quad -\frac{a}{2} < x < \frac{a}{2} \tag{2.22}$$

$$V(x) = \infty, \quad x < -\frac{a}{2}, x > \frac{a}{2} \tag{2.23}$$

Consider the eigenfunction $\Psi(x)$. As $V \rightarrow \infty$, the following conditions must apply

$$\Psi_n(x) = 0, \quad x \leq -\frac{a}{2}, x \geq \frac{a}{2} \tag{2.24}$$

Solving the time-independent Schrödinger equation for the conditions set out in Equation 2.24 gives

$$\Psi_n(x) = A_n \sin(K_n x) + B_n \cos(K_n x), \quad -\frac{a}{2} \leq x \leq \frac{a}{2} \tag{2.25}$$

where

$$K_n = \sqrt{\frac{2mE_n}{\hbar}} \tag{2.26}$$

The even parity eigen-functions are

$$\Psi_n(x) = B_n \cos(K_n x), \quad -\frac{a}{2} \leq x \leq \frac{a}{2} \tag{2.27}$$

The odd parity eigen-functions are

$$\Psi_n(x) = A_n \sin(K_n x), \quad -\frac{a}{2} \leq x \leq \frac{a}{2} \tag{2.28}$$

Due to the evenness and oddness of the eigenfunctions, Equation 2.24 need only be applied at $x = \frac{a}{2}$. Equation 2.27 leads to

$$0 = B_n \cos(\frac{K_n a}{2}) \tag{2.29}$$

hence,

$$K_n \frac{a}{2} = \frac{\pi}{2}, \frac{3\pi}{2}, \frac{5\pi}{2}, \cdots \tag{2.30}$$

giving

$$K_n = \frac{n\pi}{a}, \quad n = 1, 3, 5, \ldots \tag{2.31}$$

Applying Equation 2.24 to Equation 2.28 at $x = \frac{a}{2}$ gives

$$0 = A_n \sin(\frac{K_n a}{2}) \tag{2.32}$$

hence,

$$K_n \frac{a}{2} = \pi, 2\pi, 3\pi, \ldots \tag{2.33}$$

giving

$$K_n = \frac{n\pi}{a}, \quad n = 2, 4, 6, \ldots \tag{2.34}$$

From equations 2.31 and 2.34, the eigenvalues are

$$E_n = \frac{K_n^2 \hbar^2}{2m} = \frac{\pi^2 \hbar^2 n^2}{2ma^2}, \quad n = 1, 2, 3, 4, \ldots \tag{2.35}$$

Figure 2.10[24] illustrates the first few eigenvalues for an infinite square well. The zero point energy is the lowest energy a particle can have if bound to the region $-\frac{a}{2} \leq x \leq \frac{a}{2}$ by an infinite square well [25]. It has the form

$$E_1 = \frac{\pi^2 \hbar^2}{2ma^2} \tag{2.36}$$

The zero point energy will later be discussed in relation to quantum confined effects.

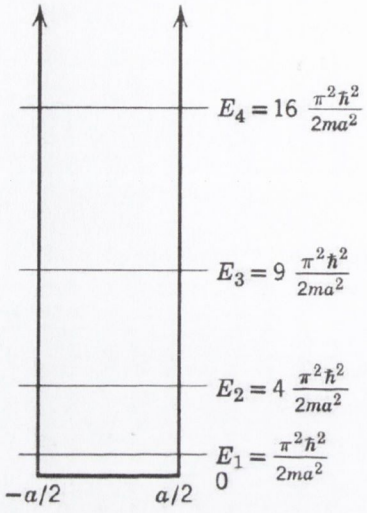

Figure 2.10: Eigenvalues for an infinite square well.

2.3.4 Quantum Confinement

The physical properties of materials may be altered when dealing with small dimensions. Quantum size effects are induced when the dimension of the material is comparable to the exciton Bohr radius. The Bohr exciton radius is the distance between an electron that has been excited to the conduction band and the hole it leaves in the valence band.

If confinement occurs in two dimensions it is referred to as a quantum well, if it occurs in one dimension it is referred to as a quantum wire, and if it is confined to zero dimensions it is referred to as a quantum dot. An illustration of the density of states as a function of dimensionality is shown in Figure 2.11.

The density of states can be expressed as

$$g(E) \equiv \frac{dN}{dE} = \frac{MV_M}{2}(2m)^{\frac{m}{2}}\frac{V_M}{h^M}E^{\frac{M-2}{2}} \tag{2.37}$$

where V_M is the volume of an M dimensional hypercube. Table 2.1 gives the equations

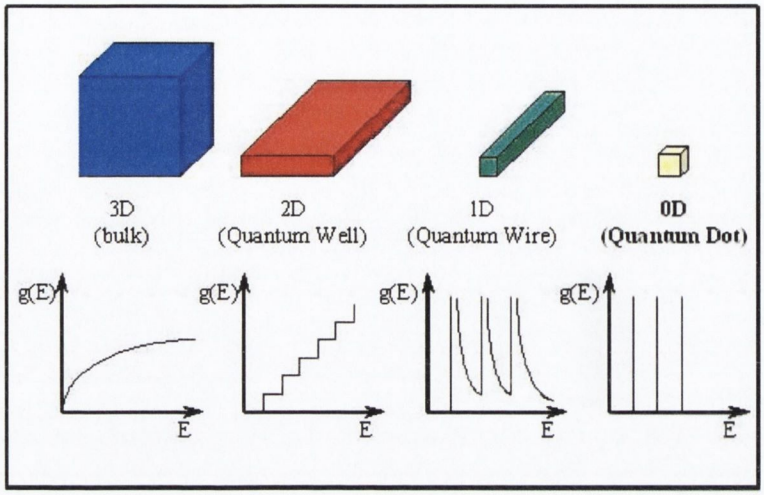

Figure 2.11: Density of states as a function of dimensionality.

of the density of states from zero to three dimensions [26].

Table 2.1: Equations for the density of states as a function of dimensionality.

Dimensionality	$g(E)$
0	δE
1	$\frac{\sqrt{2m}L}{h}\frac{1}{\sqrt{E}}$
2	$\frac{2\pi mA}{h^2}$
3	$\frac{2\pi(2m)^{\frac{3}{2}}V}{h^3\sqrt{E}}$

In three dimensions, the density of states is a smooth square root function with respect to energy. For zero, one and two dimensions, a series of discrete sub-bands appear, as illustrated in Figure 2.11[27].

Quantum confinement can be discussed in terms of a particle in a box (bound particle in an infinite square well, see Section 2.3.3). If the wall of the one dimensional potential is compressed, the gap between the energy levels of the particle increases.

For a semiconductor, this corresponds to the widening of the bandgap.

Quantum confinement can be illustrated by using the effective mass approximation for electrons and holes in a semiconductor and examining it in terms of a particle in a box [28], i.e., an electron of effective mass m_e^* and a hole of effective mass m_h^* in a 1-D potential well. The solution to the time-independent Schrdinger equation gives discrete energy levels with energies inversely proportional to the square of the width of the well. This gives rise to a negative hole effective mass, which causes an increase in the bandgap [29].

The energy of the electrons in the conduction band can be expressed as [30]

$$E_c = \frac{E_g}{2} + \frac{\hbar^2 k^2}{2m_e^*} \tag{2.38}$$

and the energy of holes in the valence band is

$$E_v = -\frac{E_g}{2} - \frac{\hbar^2 k^2}{2|m_h^*|} \tag{2.39}$$

where E_g is the band gap and k is the crystal momentum.

The ground state for a particle in a box corresponds to

$$E_{box} = \frac{\hbar^2 \pi^2}{2m^* a^2} \tag{2.40}$$

where a is the width of the well.

In a confined system

$$E_c^{confined} = E_c + \frac{\hbar^2 \pi^2}{2m^* a^2} \tag{2.41}$$

and

$$E_v^{confined} = E_v - \frac{\hbar^2 \pi^2}{2m^* a^2} \tag{2.42}$$

Hence for a confined system the band gap opens according to

$$E_g^{confined} = E_c^{confined} - E_v^{confined} \tag{2.43}$$

which leads to

$$E_g^{confined} = E_g + \frac{\hbar^2 \pi^2}{a^2}(\frac{1}{m_e^*} + \frac{1}{|m_h^*|}) \tag{2.44}$$

[30]

2.3.5 Properties of Quantum Dots

Quantum dots are approximately spherical, with all dimensions equal to or smaller than the bohr exciton radius of the material. Hence the energy levels of the quantum dot are discrete, according to the arguments laid out in Section 2.3.4. These discrete energy levels can be "tuned". The smaller the quantum dot becomes, the more the band gap widens, and the more the emission wavelength is blue-shifted. This effect is illustrated in Figure 2.3.5[31]

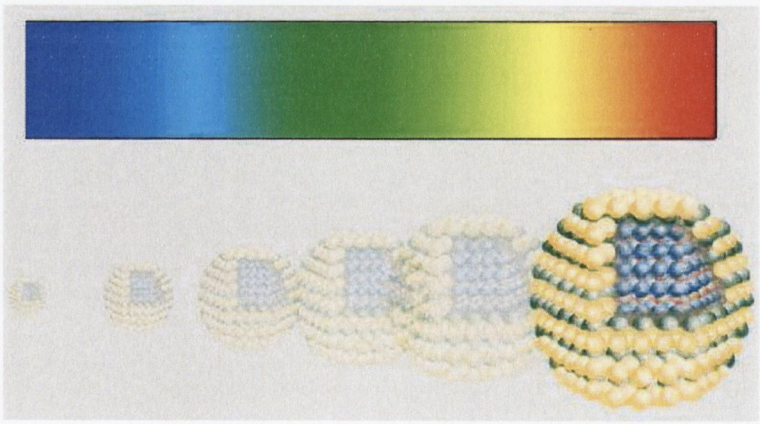

Figure 2.12: As quantum dot size decreases, the band-gap widens and the emission wavelength blue-shifts.

2.4 Luminescence from Silicon

2.4.1 Introduction

Since silicon is an indirect band-gap semiconductor, it is a highly inefficient light emitter in its bulk form. The requirement for both an appropriate photon and phonon being involved in an electron transition from the valence to the conduction band means that there is a relatively small transition probability [32]. In addition to the indirect nature of the fundamental band-gap of silicon, the gap is also too small to interact efficiently with light from the visible spectrum. This is an additional hinderance to the effectiveness of silicon in light emitting devices [33].

The exciton Bohr radius of silicon is 4.9 nm [34]. When an exciton is created in a nanocrystal with dimensions smaller than the excitonic Bohr radius of the material, the exciton is confined in real and reciprocal space. The band structure of the material ceases to be continuous and becomes discrete (see Section 2.3.4). Hence by disrupting the crystal symmetry, the momentum selection rules are relaxed and the radiative recombination is much more efficient in the quantum confined structure[35].

2.4.2 Photoluminescence Models

Although quantum confinement effects are a source of luminescence in nanoscale silicon, a number of other emission species exist for silicon. Six different models are illustrated in Figure 2.13 [36]. Excluding the quantum confinement model, all the models are based on an extrinsic origin of luminescence.

Model (a) represents emission due to quantum confinement in crystalline silicon, as previously discussed. In model (b) the emission is due to a hydrogenated amorphous

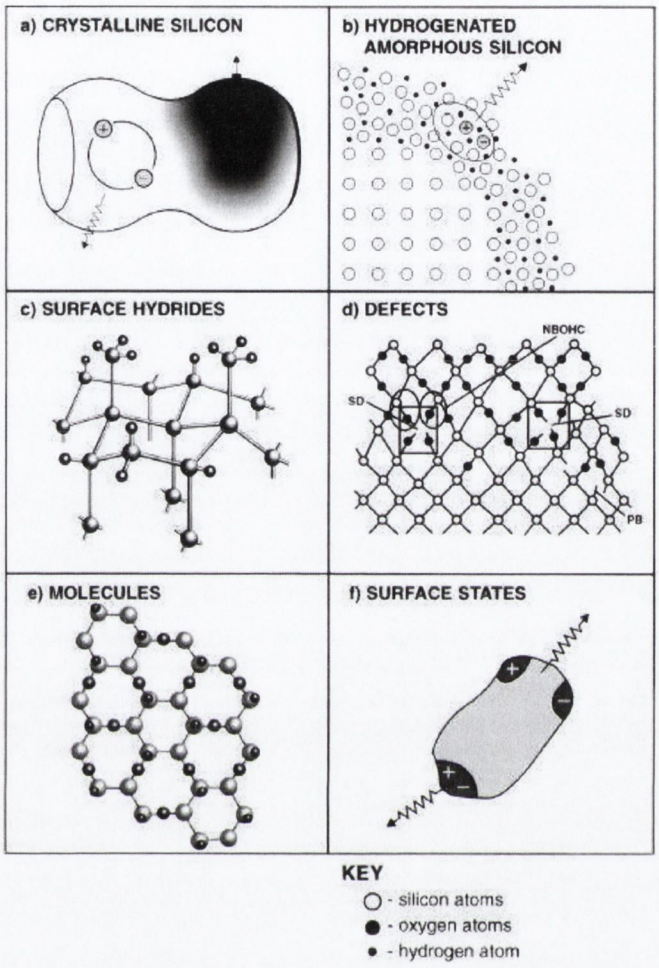

Figure 2.13: The origins of luminescence in silicon.

phase [37]. Model (c) is a surface hydride model where Si-H_x causes the luminescence [36]. In model (d) the luminescence is caused by carriers localized at extrinsic centers, i.e. defects in the crystalline silicon or silicon oxide that covers the surface [38, 39]. In model(e) Siloxene, which is an Si:H:O based polymer created during porous silicon anodization, is the proposed origin of luminescence [40]. In model (f) absorption occurs due to quantum confined structures, but radiative recombination occurs at localized surface states [41].

With regard to the silicon nanostructures under investigation in this study, only emission species involving quantum confinement, defects and surface states are applicable, i.e. models (a), (d), and (f), as hydrogen and siloxene are not present in the samples.

Many studies have been carried out on silicon-silicon oxide nanostructures [42, 43, 44, 45, 46]. Photoluminescence (PL) can be attributed to an emission species by the wavelength of the emission. Table 2.2 shows PL emission wavelengths produced by silicon nanostructures and the corresponding emission species, at room temperature [42, 43, 44, 45, 46].

Table 2.2: PL from silicon and the corresponding emission species.

PL Region	**Emission Species**
Red	Quantum confinement (at E_g of bulk silicon)
Blue-Green	Self-trapped excitons located at defects in the crystalline silicon and/or silicon oxide
UV	Quantum confinement (at direct recombination energies of bulk silicon)

Emission due to Quantum Confinement

Quantum confinement causes the band energies to become discrete, and relaxation of the k selection rule in the confined regime allows transitions to occur at E_g (see Section 2.2.5, Silicon Band Structure). Emission also occurs at the direct recombination energies of bulk silicon. Hence quantum confined emission occurs in the red region [42, 45, 43, 47], and in the ultra – violet [45]. These emission peaks can be blue-shifted in energy as the diameter of the confined region is altered.

Quantum confined emission has been reported in nanowires with core diameters far exceeding the Bohr exciton radius of silicon [43]. High resolution electron mi-

croscopy and Raman spectroscopy show that isolated crystalline grain regions can exist inside the crystalline core, which are smaller than the Bohr exciton radius and can lead to quantum confined emission. Quantum confined emission can also occur due to lattice disruption from defects such as stacking faults and grain boundaries. Increasing the oxidation time can lead to an increase in the PL emission due to quantum confinement, as the encroaching oxide forms isolated crystalline grains smaller than the Bohr exciton radius of silicon, and disruption to the lattice increases the number of defects [43].

The Effect of Oxidation on Quantum Confinement

It has been demonstrated that quantum confined emission becomes more intense as oxidation increases, and this occurs until a critical oxidation point is reached [42]. As oxidation increases, the average diameter of the crystalline regions decreases, so that more nanostructures are capable of undergoing quantum confinement. Quantum confined emission occurs until a critical point is reached when the oxidation is so extensive that almost all crystalline regions are destroyed, and emission due to quantum confinement no-longer occurs. The way in which oxidation affects nanoscale crystalline silicon can be summarised as follows [43, 42];

Stage 1: Crystalline silicon exists inside an oxide shell. Quantum confined emission can occur when the crystalline region is smaller than the Bohr exciton radius, or within a larger crystalline structure due to defects such as grain boundaries.

Stage 2: Increased oxidation can cause a size reduction of the crystalline region so that it is small enough to undergo quantum confinement. For larger crystals, e.g. 40 nm, the number of isolated crystalline grain regions also increases due to oxide

penetration forming isolated "islands" of crystalline silicon. At this stage, the effect of oxidation is to increase the strength of the emission due to quantum confinement.

Stage 3: Oxidation is extensive and few, if any, crystalline regions now exist. The structure is essentially oxide, with no contribution to PL from quantum confinement.

Emission due to Self-trapped Excitons

Emission in the blue – green region arises due to self-trapped excitons [42, 43, 44, 45, 46]. Semi-empirical tight binding and ab-initio local density calculations show that excitons self-trapped at the surface of a silicon nanocrystal are stable [48]. The PL occurs in the blue – green region, and the wavelength is independent of nanocrystal size i.e. it does not blue-shift with decreasing nanocrystal size, unlike emission due to quantum confinement [43]. The origin of visible photoluminescence from silicon is further discussed in *Chapter 7, Linear Optical Characterisation II.*

2.5 Summary

Silicon crystallises in a diamond structure and can be visualised as two interpenetrating face centered cubic lattices [9]. Each atom is surrounded by four other atoms, which it bonds to covalently.

Silicon is an indirect band-gap semiconductor and therefore is an inefficient light emitter in its bulk form. It is possible for nanoscale silicon to produce efficient light emission due to quantum confinement, as well as from extrinsic emission species. Quantum confinement effects occur when an exciton is confined to dimensions smaller than the excitonic Bohr radius of the material, which for silicon is 4.9 nm [34].

Bibliography

[1] Singleton, J. *Band Theory and Electronic Properties of Solids, p. 171.* Oxford University Press, (2001).

[2] *Bravis Lattices,* `hyperphysics.phy-astr.gsu.edu/hbase/hframe.html`, *accessed June 2007* .

[3] Singleton, J. *Band Theory and Electronic Properties of Solids, p. 168-169.* Oxford University Press, (2001).

[4] Singleton, J. *Band Theory and Electronic Properties of Solids, p. 169.* Oxford University Press, (2001).

[5] *Miller planes,* `http://upload.wikimedia.org/`, *accessed June 2007* .

[6] Singleton, J. *Band Theory and Electronic Properties of Solids, p. 17, 167.* Oxford University Press, (2001).

[7] *Reciprocal lattice,* `http://en.wikipedia.org/wiki/Reciprocal_lattice`, *accessed June 2007* .

[8] Kleinert, H. *Gauge Fields in Condensed Matter, Vol. II, "Stresses and Defects", p. 743-1456, World Scientific (Singapore, 1989); From an overview at*

http://en.wikipedia.org/wiki/Crystallographic_defect, *accessed December 2006* .

[9] Ashcroft, N. W. and Mermin, N. D. *Solid State Physics.* Saunders, (1976).

[10] *Figure: The silicon lattice,* hyperphysics.phy-astr.gsu.edu/hbase/solids/sili2.html, *accessed December 2006* .

[11] *The Fermi level and Fermi function,* http://hyperphysics.phy-astr.gsu.edu/hbase/solids/fermi.html, *accessed June 2007* .

[12] Singleton, J. *Band Theory and Electronic Properties of Solids, p. 7-9.* Oxford University Press, (2001).

[13] *Figure: The Fermi function,* http://hyperphysics.phy-astr.gsu.edu/hbase/solids/fermi.html, *accessed June 2007* .

[14] Fox, M. *Optical Properties of Solids, p. 19-20.* Oxford University Press, (2001).

[15] Fox, M. *Optical Properties of Solids, Figure 5.2, p. 95.* Oxford University Press, (2001).

[16] Fox, M. *Optical Properties of Solids, Figure 5.4, p. 97.* Oxford University Press, (2001).

[17] Fox, M. *Optical Properties of Solids, p. 50-51.* Oxford University Press, (2001).

[18] Cardona, M. and Pollack, F. *Physical Review* **142**(2), 530–543 (1966).

[19] Fox, M. *Optical Properties of Solids, p. 56.* Oxford University Press, (2001).

[20] Fox, M. *Optical Properties of Solids, p. 67.* Oxford University Press, (2001).

[21] Rae, A. I. M. *Quantum Mechanics, Fourth Edition, p. 14-16.* Institute of Physics Publishing, (2002).

[22] Rae, A. I. M. *Quantum Mechanics, Fourth Edition, p. 18,19.* Institute of Physics Publishing, (2002).

[23] Rae, A. I. M. *Quantum Mechanics, Fourth Edition, p. 19,20.* Institute of Physics Publishing, (2002).

[24] Eisberg, R. *Fundamentals of Modern Physics, p. 255.* John Wiley and Sons, (1961).

[25] Eisberg, R. *Fundamentals of Modern Physics, p. 251-255.* John Wiley and Sons, (1961).

[26] *Density of States, C.E. Mungen* `http://www.usna.edu`, *accessed July 2007* .

[27] *Figure: Density of states as a function of dimensionality,* `www.imperial.ac.uk/research/exss/research/semiconductor/qd/images/density.JPG`, *accessed January 2007* .

[28] Griffths, D. J. *Introduction to Quantum Mechanics.* Prentice - Hall, (1995).

[29] Collins, R. T., Fauchet, P. M., and Tischler, M. A. *Physics Today* **50**(24) (1997).

[30] Canham, L. T. *Properties of porous silicon.* Inspec, (1999).

[31] *Quantum dot emission* `http://www.evidenttech.com/qdotdefinition/quantumdotintroduction.php`, *accessed July 2007* .

[32] Fox, M. *Optical Properties of Solids, p. 96.* Oxford University Press, (2001).

[33] Schwarz, J., Contescu, C., and Putyera, K. *Dekker Encyclopedia of Nanoscience and Nanotechnology, p. 3563-3564.* Marcel Dekker, (2004).

[34] Cullis, A. *Journal of Applied Physics* **82**(3), 909–65 (1997).

[35] Biteen, J. S. *Plasmon-enhanced silicon nanocrystal luminescence for optoelectric applications, p. 3-4.* Thesis submitted to the Califoria Institute of Technology, Pasadena, California, (2006).

[36] Cullis, A. G., Canham, L. T., and Calcott, P. D. J. *Journal of Applied Physics* **82**(3), 909–965 (1997).

[37] Pavesi, L. *Solid State Phenomena* **44-46**(2), 261–274 (1995).

[38] Qin, G. and Jia, Y. *Solid State Communications* **86**(9), 559–563 (1993).

[39] Prookes, S. M., Carlos, W. E., and Glemblocki, O. J. *Physical Review B* **50**, 17093 (1995).

[40] Xu, Z., Gal, M., and Gross, M. *Applied Physics Letters* **60**(11), 1375 (1992).

[41] Koch, F., Petrova-Koch, V., Muschik, T., Nikolov, A., and Gavrilenko, V. *Microcrystalline Semiconductors: Materials Science and Devices Symposium* , 197–202 (1993).

[42] Yu, D., Bai, Z., Wang, J., Zou, Y., Qian, W., Fu, J., Zhang, H., Ding, Y., Xiong, G., Feng, S., You, L., and Xu, J. *Physical Review B (Condensed Matter)* **59**(4), 2498–501 (1999).

[43] Bai, Z., Yu, D., Wang, J., and Zou, Y. *Materials Science & Engineering B (Solid-State Materials for Advanced Technology)* **72**, 117–120 (2000).

[44] Qi, J., Belcher, A., and White, J. *Applied Physics Letters* **82**(16), 2616–18 (2003).

[45] Wilcoxon, J., Samara, G., and Provencio, P. *Physical Review B (Condensed Matter)* **60**(4), 2704–14 (1999).

[46] Kanemitsu, Y. *Journal of Luminescence* **100**(1-4), 209–217 (2002).

[47] Calcott, P. **B51**, 132–40 (1997).

[48] Allan, G., Delerue, C., and Lannoo, M. *Physical Review Letters* **76**(16), 2961–4 (1996).

Chapter 3

Growth and Preparation Techniques

3.1 Introduction

In section 3.2 of this chapter, various silicon nanowire production methods will be discussed, and the production methods relevant for each of the samples under study will be outlined. Samples A, B and C were manufactured by Alan Colli in the Department of Engineering, University of Cambridge, U.K. Samples A and B were produced by the 'growth from oxide' technique. Sample C was prepared by a gold catalyzed thermal evaporation method. Samples D and E were manufactured by a private company in Germany by chemical vapour deposition. Detailed information on the morphology of each wire sample is presented in *Chapter 4, Structural Characterisation.*

Section 3.3 outlines the sample preparation techniques utilised to prepare the nanostructures for the characterisation studies.

3.2 Growth Techniques

3.2.1 Vapour-Liquid-Solid Growth Model

The Vapour-Liquid-Solid model proposes that silicon nanowire growth can occur due to liquid gold (Au) particles forming a eutectic with silicon vapour and producing a 1D precipitation. The silicon-gold eutectic temperature is 363°C [1]. This is called a 'Au-catalyzed' method. The VLS model is used to explain the physics responsible for growth in these conditions.

Traditionally, wires were grown using $SiCl_4$ as the Silicon source gas. The reaction temperature for this method is approximately 1000°C. Using silane (SiH_4)as the source gas allows growth at lower temperatures. The bond energies in silane are 3.9 eV, whereas in $SiCl_4$ they are 4.8 eV. The silane decomposition reation is thermodynamically very favourable [2]. Reports on the growth of silicon nanowires through the VLS method include Wagner *et al.* [3], Givargizov and Chervov [4], Givargizov [5] and Westwater *et al.* [2].

3.2.2 Nanowire Growth from Oxide

With this method of nanowire synthesis, silicon oxide must first be evaporated either by laser ablation or thermal evaporation. The resulting vapour is carried down an alumina tube by an inert gas such as argon. At the initial nucleation stage, silicon oxide vapour condenses on a cooler region of the alumina tube and forms silicon nanoparticles. They continue to absorb reactive SiO clusters and facilitate the formation of silicon nanowires [6, 7]. It is thought that SiO_x clusters attach to the tips of the nanowires. SiO_2 forms an outer shell that restricts lateral growth [8]. The

nucleation of nanoparticles is assumed to occur by different decompositions of silicon oxide as shown in equations 3.1 and 3.2 [7]

$$Si_xO \longrightarrow Si_{x-1} + SiO, \tag{3.1}$$

where $x > 1$ and

$$2SiO \longrightarrow Si + SiO_2, \tag{3.2}$$

Details on the structure of silicon nanowires grown from oxide using laser ablation can be found in a report by Wang *et al.* [9]. Reports on silicon nanowires grown from oxide using thermal evaporation are also available [10, 11, 1].

3.2.3 Chemical Vapour Deposition

Chemical vapour deposition is based on the decomposition of a gas onto a substrate. For silicon nanostructures, silane is often used as the process gas and gold as the mediating solvent on a silicon substrate. When the gold is heated, the gold and silicon form a eutectic, as per the VLS method. Silcon is dissolved from the vapour phase, leading to the production of silicon nanowires with gold tips. Wires grown at low temperatures with small quantities of gold tend to produce thinner wires because the molten alloy breaks up into small spheres. If the spheres become too small then wire growth is not possible, as it becomes chemically favourable for the silicon to stay in the vapour phase and not deposit on the eutectic [2].

3.2.4 Relevant Processes for the Samples under Study

Samples A and B

SiO_2 powders were evaporated in a high temperature furnace at 1400°C. The vapour formed from this evaporation was swept down an alumina tube by argon gas. Within the alumina tube, argon pressure was kept constant at 500 mbar and a 50 sccm (standard cubic centimeters per minute) argon flow was admitted (and pumped at the same time from the downstream outlet). The vapour condensed in the colder regions of the tube (900–950°C) in the form of silicon nanowires. Growth time was three hours. The individual nanowires were collected in the form of an orange flake which had formed on the alumina tube. The flake was approximately 1 centimeter in diameter. This "flake" consisted of individual nanowires which were later separated by placing the flake into solution and gently agitating it with a sonic tip. With this method, wires that condense in different locations have different morphologies. Debate continues as to whether this is due to local temperature or pressure variations [12, 1].

Sample C

Sample C was prepared by a thermal evaporation method, with gold as a mediating catalyst. The silicon vapour was provided by thermal evaporation of pure silicon powder. The process was carried out at 700–800°C. For this method the VLS model is consistent, as the operating temperature is well above the gold-silicon eutectic temperature [1]. Hence it is probably most correct to say that Sample C was produced through gold catalysed thermal evaporation, following the VLS model.

Samples D and E

Samples D and E were produced by CVD with silane as a precursor and gold as a mediating catalyst. They were supplied by a private company, hence the exact parameters used during production are not known. There are some structural differences between the two samples, as will be discussed in Chapter 4. These differences could arise from varying growth conditions such as temperature, pressure and growth time.

3.3 Specimen Preparation

3.3.1 Fluidic Dispersion

The majority of characterisation techniques utilised in this report were carried out on the silicon nanowires in isopropal alcohol (IPA) dispersions. Samples D and E were delivered by the manufacturer already in an IPA solution. Samples A, B and C were delivered in solid form. They were each placed in spectroscopic grade IPA. The nanowires were then dispersed by agitation with a sonic tip. To ensure that during subsequent investigation processes, the concentration of the nanowire dispersions would not change due to sedimentation, it was necessary to obtain a stable suspension of each sample. This process is outlined in Section 3.3.2.

An alternative method of dispersion could have involved the use of tensio-active molecules which have a polar – non-polar structure and can aid in dispersion. Solvent–oxide interaction, and in particular the effects of heat dissipation at the oxide surface, are of interest in the non-linear optical study, which would have been complicated by the addition of surface moieties. The suspensions obtained using dispersion by a sonic

tip with no use of tensio-active molecules produced suspensions which had stable phases with lifetimes far exceeding those required for the characterisation studies undertaken in this report.

3.3.2 Sedimentation Profiling

Methodology

Each of the five sample dispersions underwent gentle agitation with a sonic tip. The samples were then immediately placed into a machine to record their sedimentation profiles. This involved recording the changes in the intensity of light from a series of lasers as it travelled through the dispersions, as outlined in Figures 3.1 and 3.2. From the sedimentation profile, it was possible to determine the life-times of any unstable phases present. It was necessary to separate out any unstable phases to enable accurate, repeatable studies such as z-scan analysis and 3-D photoluminescence studies to be carried out.

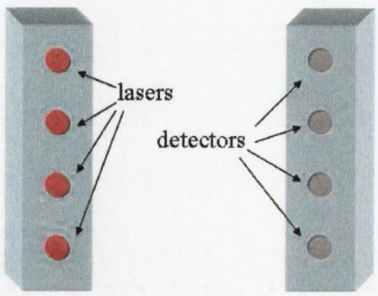

Figure 3.1: Graphic of sedimentation laser set-up.

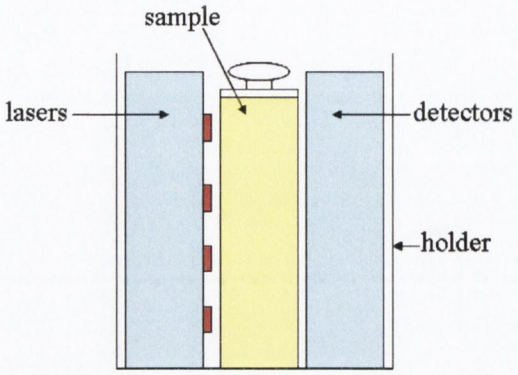

Figure 3.2: Graphic of sedimentation machine with sample in position.

3.3.3 Theory of Sedimentation

The sedimentation properties of the suspensions were studied by monitoring the optical transmission of the dispersions with respect to time. The optical transmission changed as non-stable phases sedimented out of the dispersion. A sedimentation equation, which demonstrates that the concentration of any insoluble dispersed phase decreases exponentially with time, was utilised [13] . Turbidity is essentially a measure of the cloudiness of a sample, and is often utilised as a tool for assessing the purity of water. The higher the turbidity of a sample, the cloudier it is. Turbidity can be represented by the product of sample concentration C and an effective extinction co-efficient α. α represents all absorption and extinction processes. There are three main assumptions made, 1. the solid particles are small with respect to the sedimentation vessel and have the same density; 2. the constituents of the solution are incompressible; 3. there is no mass transfer between the solid and the fluid during sedimentation. Each phase in a solution has its own time constant and partial concentration. There may also be soluble components present. Some equations will be presented here that enable the analyses of the different phases present in a solution. A

full treatment of the derivations can be found in 'Solubility of Mo_6 $S_{4.5}$ $I_{4.5}$ nanowires in common solvents, a sedimentation study' by Nicolosi *et al.* [13].

The local time dependent concentration of a dispersion with n insoluble components and one soluble phase can be described by

$$C_t = C_0 + \sum_n C_n e^{-t/\tau_n}, \tag{3.3}$$

where C_0 is the concentration of the soluble phase. Due to the conservation of mass, the initial concentration C_{Tot} is given by

$$C_{\text{Tot}} = C_0 + \sum_n C_n. \tag{3.4}$$

Total turbidity $T(t)$ should decay as

$$T(t) = T_0 + \sum_n T_n e^{-t/\tau_n} = \alpha_0 C_0 + \sum_n \alpha_n C_n e^{-t/\tau_n}, \tag{3.5}$$

where α_0 and α_n represent the extinction co-efficients of the soluble and insoluble phases, T represents the turbidity, T_0 is the turbidity of the soluble phase, C is the sample concentration, α represents the effective extinction co-efficient and τ is the time constant.

The analogue of Equation 3.4 is

$$T_{\text{Tot}} = T_0 + \sum_n T_n. \tag{3.6}$$

In order to fit an appropriate decaying exponential function and calculate lifetimes for the unstable phases of each sample, the turbidity at each second over a long period of time needed to be calculated.

According to the Beer Lambert law, the concentration of a substance in solution is directly proportional to the absorbance of the solution. In this situation, "absorbance"

includes pure electronic absorption as well as extinction due to scattering processes. Hence,

$$A = \ln(I_0/I) = \alpha C L \tag{3.7}$$

where A is the absorbance, I_0 is the intensity of incident radiation, I is the intensity of radiation transmitted through the sample, α represents the effective extinction co-efficient, C is the concentration of the solution and L is the sample path length.

Turbidity can be expressed as

$$T = \alpha C \tag{3.8}$$

Substituting T into equation 3.7 gives

$$A = TL \tag{3.9}$$

Hence

$$T = \frac{A}{L} = \frac{\ln(I_0/I)}{L} \tag{3.10}$$

where L is the path length of the sample, in our case, 1 cm. Hence turbidity as a function of time could be calculated by measuring I_0 initially, and then I as a function of time. Since

$$T_{\text{Tot}} = T_0 + \sum_n T_n e^{-t/\tau_n} \tag{3.11}$$

the time constants of the unstable phases of each sample could then be extracted by fitting an appropriate decaying exponential.

3.3.4 Results of Sedimentation Profiling

Due to the popularity of the sedimentation apparatus with many researchers, it was not possible to reach a completely stable state for most of the samples under study

here. However, the objective of this study was to obtain suspensions which would remain stable over the course of a particular characterisation, e.g. photoluminescence characterisation. Suspensions with lifetimes far exceeding the minimum requirements were obtained. Graphs of the turbidity of each sample as a function of time are shown below. Each profile was best fit in terms of χ^2 and R^2. Normalised turbidity is shown in arbitrary units (a.u.). Samples A, B, C and D were best fit by first order decaying exponential functions, that is

$$T_{\text{Tot}} = T_0 + T_1 e^{-t/\tau_1} \tag{3.12}$$

This means that each of the four samples contained a stable component and one unstable component. Sample E was stable over the time framed studied and will be discussed separately.

The fits obtained were of good quality. Some may not appear to be very good to the naked eye, but that is because they are displayed on a log scale, which is the convention for turbidity graphs. The discrepancy between experimental and fitted curves occurs only for the horizontal parts of these curves, and therefore do no significantly alters the determination of lifetimes. When examined over the lifetime of the sedimentation study using a linear scale, it is clear that the fits are of good quality. The graphs displayed here were best fit in terms of χ^2 and R^2 using Origin software. The fits were double-checked using an excel based package, and best fit was achieved by minimising the sum of the squared residuals. The results of both fitting methods were in good agreement with each other.

Sample A was fit with a first order decaying exponential, with $\chi^2 = 0.002$ and $R^2 = 0.72645$. $\tau = 575848 \pm 21467$ seconds, as shown in Figure 3.3. Hence the lifetime of the unstable phase of Sample A is 6.7 days $\pm$5.96 hours.

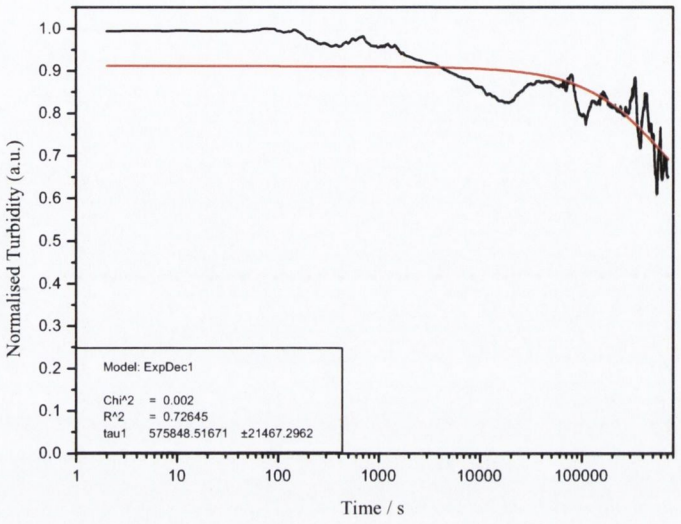

Figure 3.3: Plot of normalised turbidity against time for Sample A.

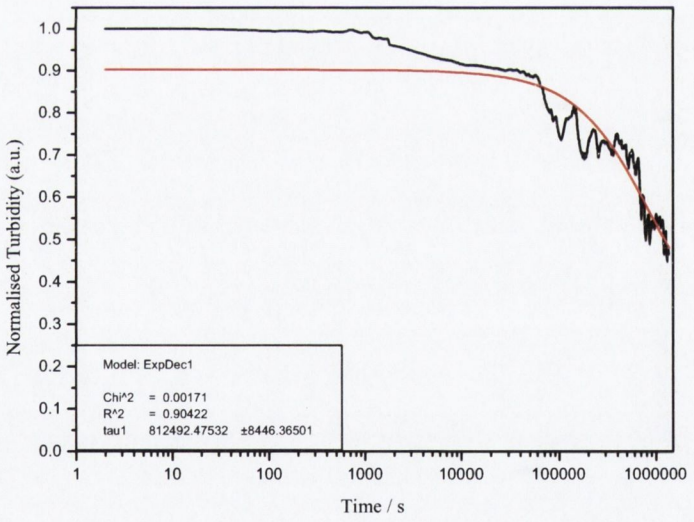

Figure 3.4: Plot of normalised turbidity against time for Sample B.

Sample B was fit with a first order decaying exponential, with $\chi^2 = 0.00171$ and $R^2 = 0.90422$. $\tau = 812492 \pm 8446$ seconds, as shown in Figure 3.4. Hence the lifetime

of the unstable phase of Sample B is 9.4 days ±2.35 hours.

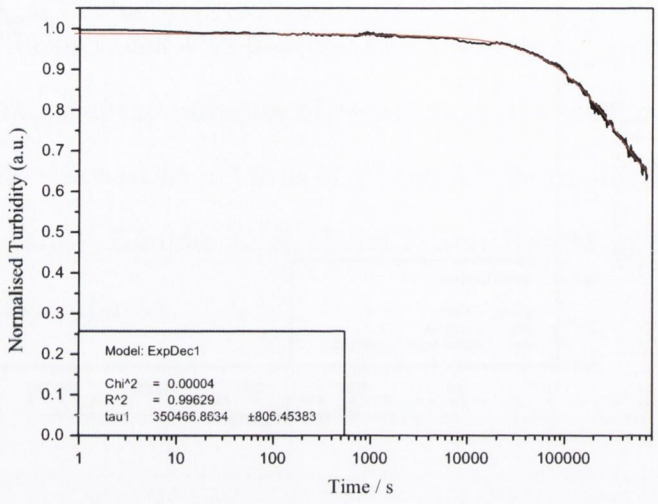

Figure 3.5: Plot of normalised turbidity against time for Sample C.

Sample C was fit with a first order decaying exponential, with $\chi^2 = 0.00004$ and $R^2 = 0.99629$. $\tau = 350466 \pm 806$ seconds, as shown in Figure 3.5. Hence the lifetime of the unstable phase of Sample C is 10.14 days ±13 minutes.

Sample D was fit with a first order decaying exponential, with $\chi^2 = 0.0004$ and $R^2 = 0.98958$. $\tau = 16891 \pm 59$ seconds, as shown in Figure 3.6. Hence the lifetime of the unstable phase of Sample D is 4.69 hours ±59 seconds.

When the unstable components had separated out for Samples A, B, C and D, the stable components were carefully pipetted off. From this point on in the text, all references to Sample A, B, C or D are referring to these stable components.

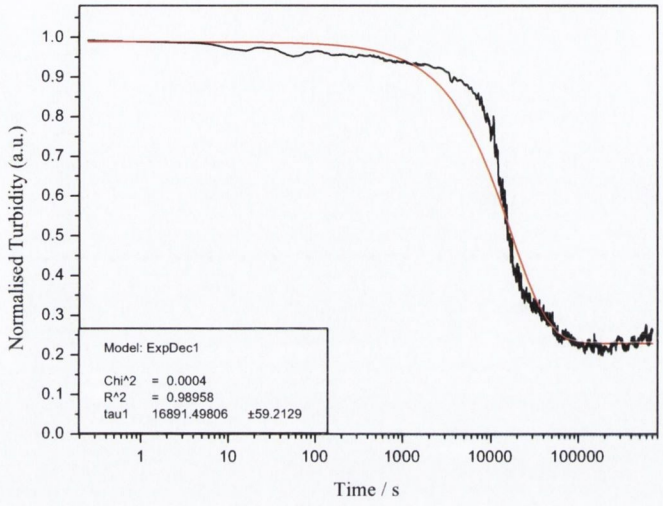

Figure 3.6: Plot of normalised turbidity against time for Sample D.

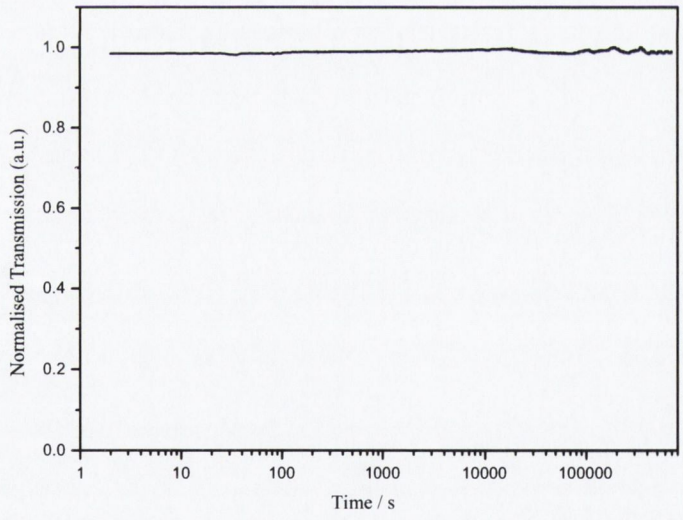

Figure 3.7: Plot of normalised transmission against time for Sample E.

A graph of turbidity against time for Sample E was not satisfactorily fit by any form of decaying exponential function. From Figure 3.7 it is clear that the sample is stable over the time frame studied. It is likely that the sample may start to fall out

of the suspension over a long period, for example months. Hence Sample E can be considered to be a stable suspension for the purposes of this investigation.

3.4 Conclusions

Silicon nanowires can be produced by various techniques including oxide assisted growth, thermal evaporation with gold as a mediating catalyst and chamical vapour deposition. Five samples of silicon nanowires, produced by various growth techniques, were dispersed in IPA using gentle agitation by a sonic tip. To ensure that during subsequent investigation processes, the concentration of the nanowire dispersions would not change due to sedimentation, it was necessary to obtain a stable suspension of each sample.

The sedimentation properties of the suspensions were studied by monitoring the optical transmission of the dispersions with respect to time. A stable dispersion of each sample was obtained. The sedimentation graphs were best fit in terms of χ^2 and R^2 using Origin software. The fits were double-checked using an excel based package, and best fit was achieved by minimising the sum of the squared residuals. Although saturation could not be reached for some of the samples due to limited access to the apparatus, the objective of the procedure was to obtain suspensions which would be stable over the lifetime of subsequent investigations, for example, three dimensional photoluminescence spectroscopy. This requirement was satisfied for all of the samples. All further analysis in this report pertaining to nanowires dispersed in IPA refers to these stable dispersions.

Bibliography

[1] Colli, A., Hofmann, S., Fasoli, A., Ferrari, A., Ducati, C., Dunin-Borkowski, R., and Robertson, J. *Applied Physics A (Materials Science Processing)* **85**, 247–253 (2006).

[2] Westwater, J., Gosain, D., Tomiya, S., Usui, S., and Ruda, H. *Journal of Vacuum Science & Technology B (Microelectronics and Nanometer Structures)* **15**(3), 554–7 (1997).

[3] Wagner, R. and Ellis, W. *Metallurgical Society of American Institute of Mining, Metallurgical and Petroleum Engineers – Transactions* **233**(6), 1053 – 1064 (1965).

[4] Givargizov, E. and Chernov, A. *Soviet Physics - Crystallography* **18**(1), 89 – 92 (1973).

[5] Givargizov, E. *Journal of Crystal Growth* **31**(1), 20 – 30 (1975).

[6] Zhang, R., Chu, T., Cheung, H., Wang, N., and Lee, S. *Materials Science & Engineering C, Biomimetic and Supramolecular Systems Symposium-C, Nanostructured Materials* **C16**(1-2), 31–5 (2001).

[7] Lee, S., Wang, N., and Lee, C. *Materials Science & Engineering A (Structural Materials: Properties, Microstructure and Processing)* **A286**(1), 16–23 (2000).

[8] Zhang, R.-Q., Lifshitz, Y., and Lee, S.-T. *Advanced Materials* **15**(7-8), 635–640 (2003).

[9] Wang, N., Tang, Y., Zhang, Y., Lee, C., and Lee, S. *Physical Review B (Condensed Matter)* **58**(24), 16024–6 (1998).

[10] Wang, N., Tang, Y., Zhang, Y., Lee, C., Bello, I., and Lee, S. *Chemical Physics Letters* **299**(2), 237–42 (1999).

[11] Wen-Sheng, S., Hong-Ying, P., Yu-Feng, Z., Ning, W., Nai-Gui, S., Zhen-Wei, P., Chun-Sing, L., and Shuit-Tong, L. *Advanced Materials* **12**(18), 1343–5 (15).

[12] Sun, X., Wong, N., Li, C., Lee, S., and Sham, T. *Journal of Applied Physics* **96**(6), 3447–51 (2004).

[13] Nicolosi, V., Vrbanic, D., Mrzel, A., McCauley, J., O'Flaherty, S., McGuinness, C., Compagnini, G., Mihailovic, D., Blau, W. J., and Coleman, J. N. *Journal of Physical Chemistry B* **109**(15), 7124–7133 (2005).

Chapter 4

Structural Characterisation

4.1 Introduction

Various techniques were employed to determine the morphology of each nanowire sample. The structure, length and diameter of the wires in each sample were investigated using transmission electron microscopy (TEM). A high resolution transmission electron microscopy (HRTEM) study was also carried out. Sample A underwent additional characterisation using Energy-Filtering Transmission Electron Microscopy (EFTEM), Electron Energy Loss Spectroscopy (EELS) and Raman. The various techniques are described in Section 4.2, and the results are presented and discussed in Sections 4.3, 4.4 and 4.5.

4.2 Characterisation Techniques

4.2.1 Transmission Electron Microscopy

The transmission electron microscope uses electrons as the source making it possible to get a resolution a thousand times better than with a light microscope. If the microscope is operating to a high standard, it is possible to image features as small as a few angstroms.

Figure 4.1 is an illustration of a TEM arrangement [1]. An electron source at the top of the microscope emits electrons that travel through a vacuum in the column of the microscope. Electromagnets focus the electrons into a very thin beam. The electron beam then travels through the specimen under study. Depending on the density of the material present, some of the electrons are scattered and disappear from the beam. At the bottom of the microscope the unscattered electrons hit a fluorescent screen, which gives rise to a "shadow image" of the specimen with its different parts displayed in varied darkness according to their density. The image can be studied directly by the operator or photographed with a camera [2]. CCD detectors are often employed to collect the images, which can then be stored electronically.

4.2.2 High Resolution Transmission Electron Microscopy

High Resolution Transmission Electron Microscopy (HRTEM) allows the imaging of the crystallographic structure of a sample at the atomic scale. It produces high resolution and is frequently used in the study of nanoscale crystalline materials. Currently the highest achievable resolution is 0.8 Å. Research is ongoing that will enable a resolution as high as 0.5 Å. At these small scales, individual atoms and crystalline defects

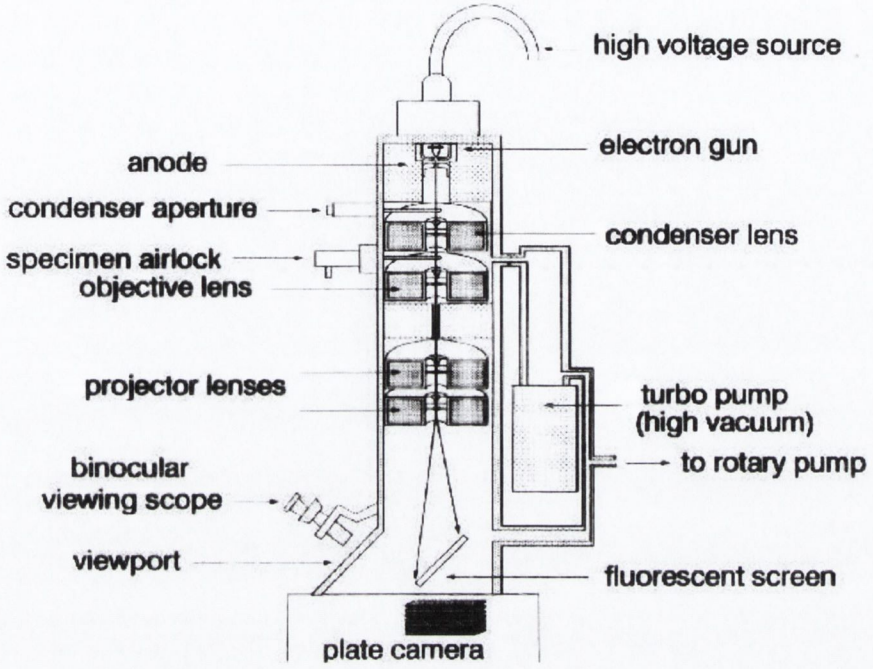

Figure 4.1: Illustration of a TEM set-up.

can be imaged. Conventional TEM uses absorption by the sample for image formation. HRTEM uses contrast from the interference in the image plane of the electron wave with itself. It is currently impossible to record the phase of these waves, so the amplitude resulting from this interference is measured, however the phase of the electron wave still carries the information about the sample and generates contrast in the image [3].

4.2.3 Energy-Filtering Transmission Electron Microscopy

With Energy-Filtering Transmission Electron Microscopy (EFTEM) an image is produced by electron scattering in the sample. If the sample's atoms are ionised during the inelastic scattering process, energy losses which are characteristic of the elements

present will result. The technique also utilises additional interactions. Electrons can be selected according to their scattering angle, energy and energy bandwidth. This allows for very good contrast to be obtained, particularly with samples containing light elements [4].

4.2.4 Electron Energy Loss Spectroscopy

Electron Energy Loss Spectroscopy (EELS) is usually used in conjunction with an electron microscope. It makes use of incident electrons that are inelastically scattered by the sample under study. A specific region of interest can be selected from the electron microscopic image of the sample. Elemental composition is determined by analyzing the energy of the scattered electrons with a spectroscope which is attached under the electron microscope. Electrons with a particular energy loss can be selected, allowing the elemental distribution in a sample to be recorded [5].

4.2.5 Introduction to Raman Spectroscopy

Raman spectroscopy is used to study vibrational, rotational, and other low-frequency modes in a system. It relies on inelastic scattering of monochromatic light, usually from a laser in the visible, near infrared, or near ultraviolet range. The shift in energy gives information about the phonon modes in the system. Wavelengths close to the laser line (due to elastic Rayleigh scattering) are filtered out and those in a certain spectral window away from the laser line are dispersed onto a detector, usually a CCD camera.

Raman scattering occurs in a system as follows. A photon excites one of the electrons into a virtual state. When the photon is released the molecule relaxes

back into a vibrational energy state. The molecule will usually relax into the first vibrational energy state, which is called Stokes Raman scattering. If the molecule was already in an elevated vibrational energy state, the Raman scattering is then called Anti-Stokes Raman scattering [6], see Figure 4.2 [7].

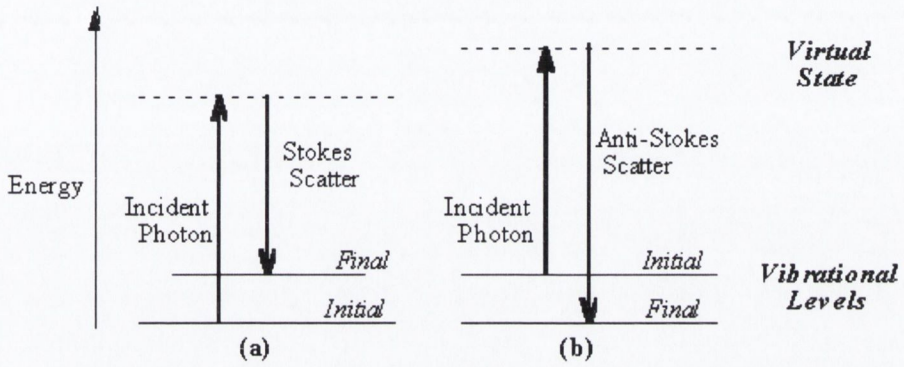

Figure 4.2: Raman scattering.

4.2.6 Raman Spectroscopy of Silicon

For silicon, a Raman peak at 520 cm^{-1} is due to scattering of the first order optical phonon of crystalline silicon. This is a first order scattering process. A broad peak at 300 cm^{-1} is associated with the scattering of two transverse acoustic (2TA) phonons. A broad peak at 970 cm^{-1} is due to the scattering of two transverse optical (2TO) phonons. Both these peaks are the result of a two phonon process, and are referred to as second order scattering [8].

When crystalline size decreases, momentum conservation is relaxed and the Raman active modes are not limited to the centre of the Brillouin zone. As crystalline size decreases, the shift towards lower frequences increases. The peaks also become broader and more asymmetric [8]. Li *et al.* also noted that it is not the width of a

nanowire that is significant, rather the size of the crystalline grains that it contains.

Discrepancies between the degree of frequency shift with reducing nanocrystal size reported by different groups may be due to the imperfect nature of some silicon lattice structures. Defects can induce strain in a lattice and effect the Raman spectrum. They can also break up crystalline regions into smaller grain regions, and lead to the enhancement of quantum confined effects [8].

There have been reports that the downshifting and broadening of silicon Raman peaks is due to laser heating of the sample [9, 10]. This does not mean that at least some downshifted features are due to phonon confinement. When extremely low laser power was utilised by Piscanec *et al.*, there was still evidence of phonon confinement. Also, Meier *et al.* [11] and Li *et al.* [8] used a constant laser power and still observed a shift towards lower frequencies for silicon nanocrystallites of decreasing size.

4.3 TEM Results

The TEM was carried out using a Hitachi H-7000. The samples were imaged on 400 mesh holey carbon grids, using a drop casting deposition method. [1]

4.3.1 Sample Morphologies

Figure 4.3 shows Sample A, which consisted of a chain-like structure, with spheres of crystalline silicon surrounded and connected by SiO_x shells.

Figure 4.4 shows Sample B, which consisted of a tadpole-like structure, with each

[1]The majority of TEM images were taken by Sharon McNicholas. Due to the malfunction of the TEM in Trinity College towards the end of the project, some additional images were obtained from the TEM in the Focus Institute at the Dublin Institute of Technology, by technician Anne Shanahan.

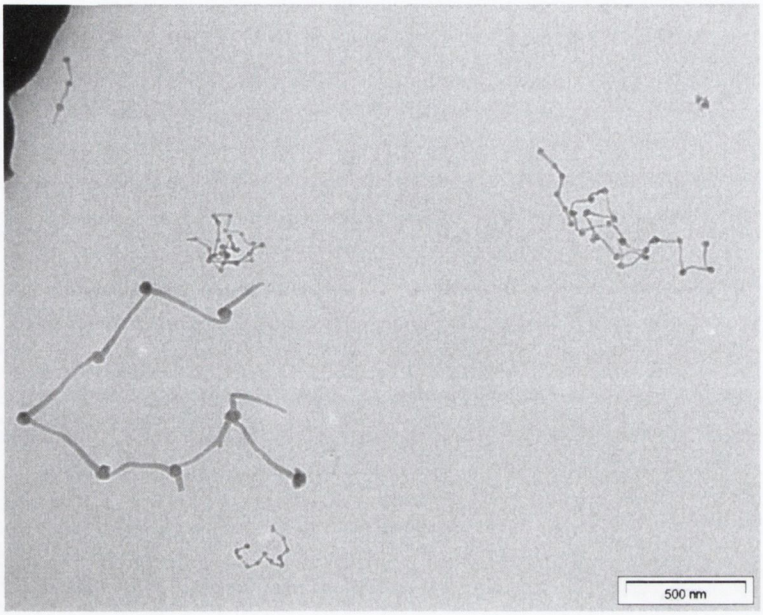

Figure 4.3: Morphology of Sample A.

sphere of crystalline silicon connected to a crystalline silicon nanowire. The entire structure was coated by an SiO_x shell.

Figure 4.5 shows Sample C, which consisted of crystalline silicon nanowires coated in oxide. It is clear that there is a broad distribution of wire sizes. Note: The carbon grid is visible in the image.

Figure 4.6 shows Sample D, which consisted of straight crystalline silicon nanowires coated in oxide. A catalyst particle can be seen at the tip of the nanowire.

Figure 4.7 shows Sample E, which consisted of crystalline silicon nanowires coated in oxide. There appears to be wire fragments of various sizes present in the sample. Note: The carbon grid is visible in the image.

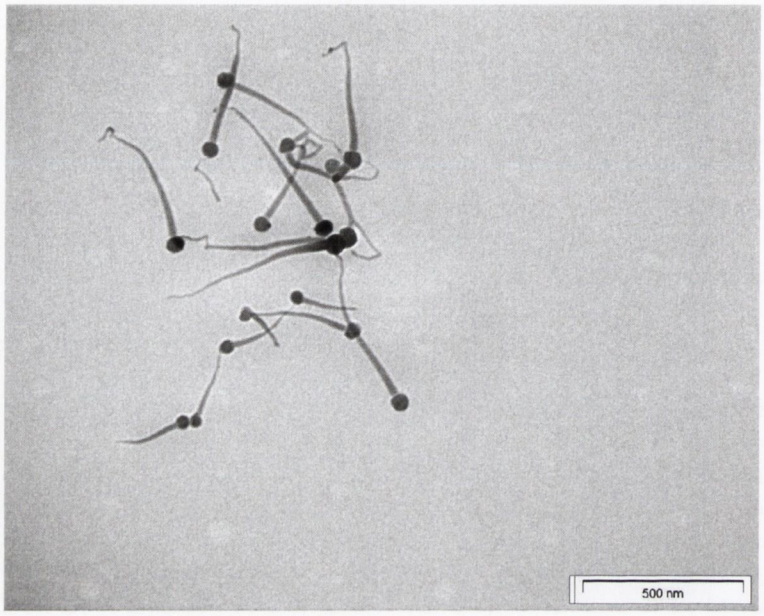

Figure 4.4: Morphology of Sample B.

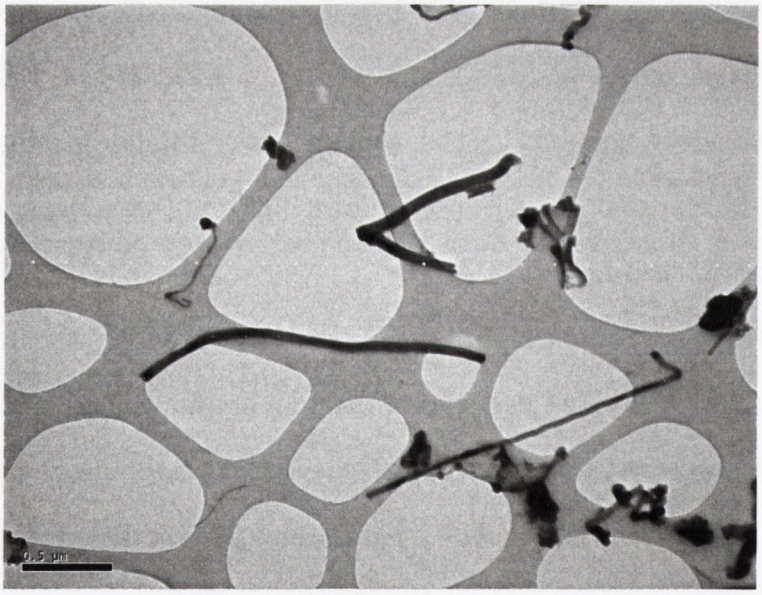

Figure 4.5: Morphology of Sample C.

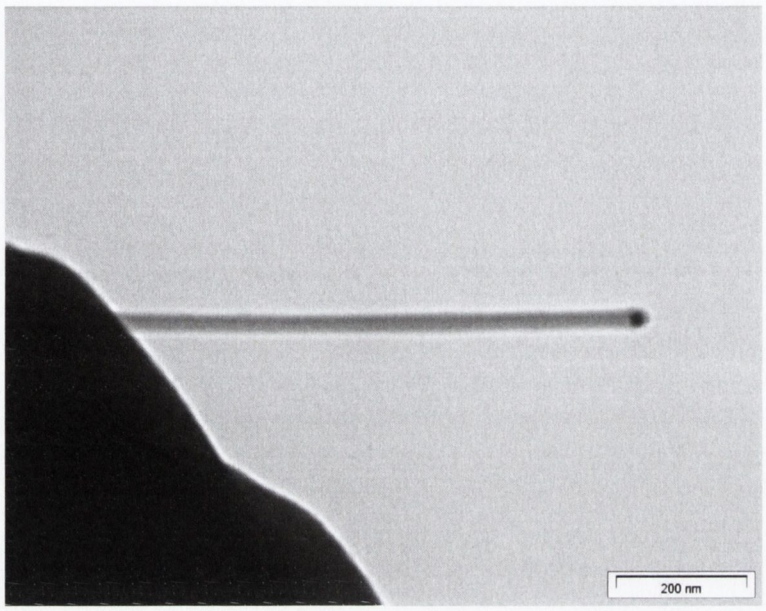

Figure 4.6: Morphology of Sample D.

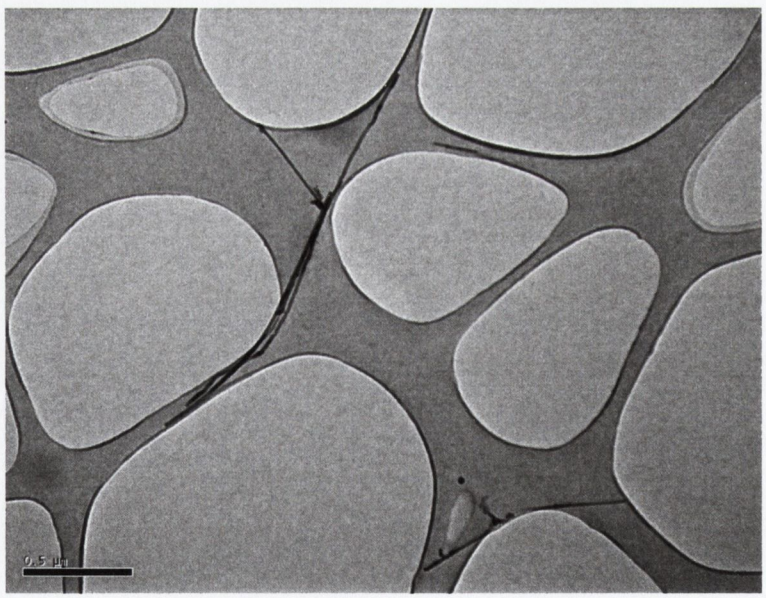

Figure 4.7: Morphology of Sample E.

4.3.2 Nanowire Dimension Study

The lengths and diameters of a number of nanowires from each sample were recorded. 50 nanowires were imaged and analysed for samples A, B, and D. 25 nanowires were imaged and analysed for samples C and E. A smaller number of nanowires were studied for Samples C and E because these solutions were more dilute, and therefore it took much longer to find and image each nanowire. Time constraints at the microscopy facility resulted in a smaller sample set being studied for these wires.

Notes regarding the measurement of values

50 spheres from Sample A were chosen at random and their diameters were recorded. The average diameter of a sphere turned out to be 31 nm, inclusive of the oxide shell. A 5 nm thick coating of oxide would result in the average diameter of a crystalline sphere of Sample A being 21 nm.

For Sample B, the diameter measurements were made half-way down the length of each wire, as the wires tended to taper off towards their tails (i.e. they were fatter at the end attached to the sphere, and thinner at the tail end), see Figure 4.4.

50 spheres from Sample B were chosen at random and their diameters were recorded. The average diameter of a sphere turned out to be 70 nm, inclusive of the oxide shell. A 5 nm thick coating of oxide would result in the average diameter of a crystalline sphere of Sample B being 60 nm.

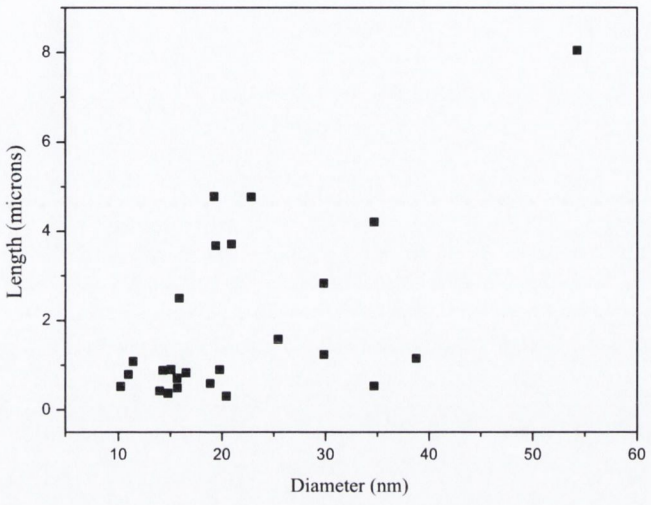

Figure 4.8: Nanowire length v diameter for Sample A.

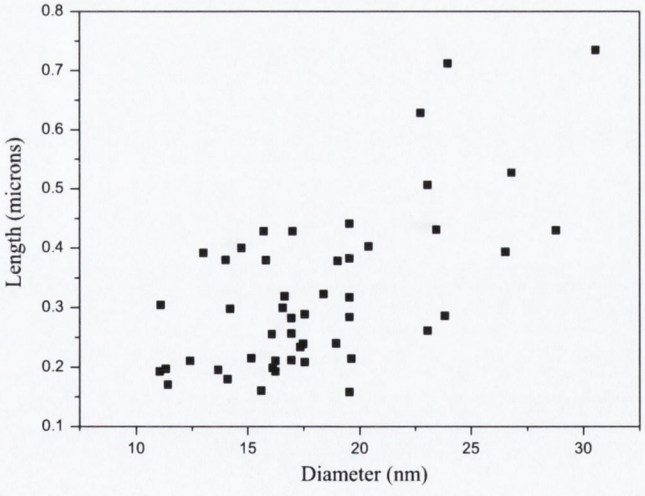

Figure 4.9: Nanowire length v diameter for Sample B.

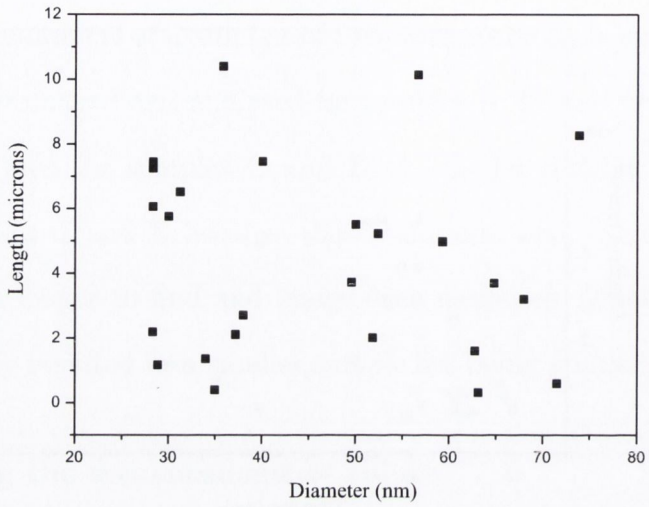

Figure 4.10: Nanowire length v diameter for Sample C.

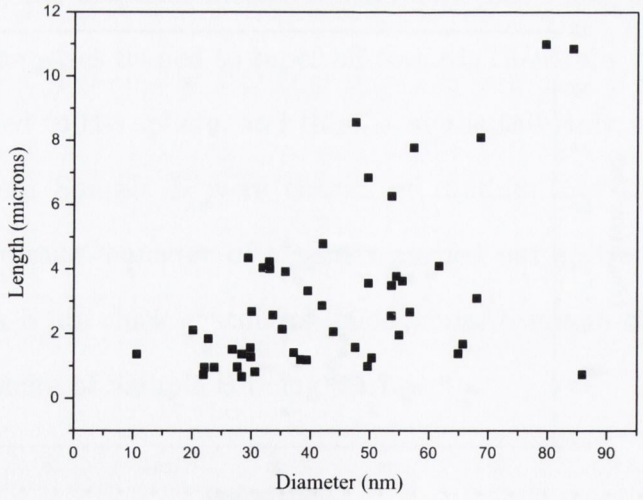

Figure 4.11: Nanowire length v diameter for Sample D.

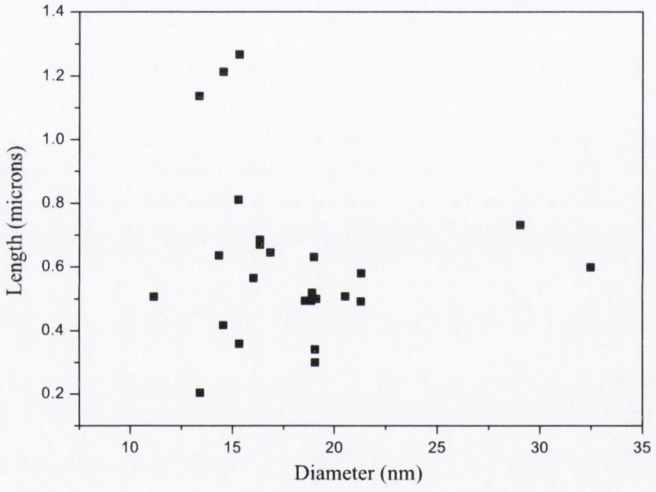

Figure 4.12: Nanowire length v diameter for Sample E.

Analysis

The average diameters of the nanowires, and where applicable nanospheres, are presented in Table 4.1. The values are inclusive of the outer oxide layer. "Sample Size" refers to the number of wires or spheres recorded for each sample. The corresponding standard deviation is presented in brackets after the average diameter.

Note: From Table 4.1 it is clear that the diameter of the crystalline cores of the nanowires in each sample are too large to undergo quantum confined effects. However, it may still be possible to experience quantum confined light emission from the samples, even though their diameters are larger than the Bohr exciton radius of silicon [12]. Quantum confined emission can occur due to lattice disruption from defects such as stacking faults and grain boundaries, and from isolated crystalline grain regions that exist within the crystalline nanowire core.

Table 4.1: Nanostructure diameters. "Sample Size" refers to the number of wires or spheres recorded for each sample.

Sample	**Sample Size**	**Wire Diameter (nm)**	**Sphere Diameter (nm)**
Sample A	50	19 (8)	31 (12)
Sample B	50	18 (4)	70 (11)
Sample C	25	46 (16)	N/A
Sample D	50	44 (17)	N/A
Sample E	25	18 (5)	N/A

The linear correlation factor for length versus diameter was calculated for each sample, from the scatter plots labelled as Figures 4.8 to 4.12. The linear correlation factor between length and diameter for each sample is presented in Table 4.2. The corresponding growth methods are also listed, where "ox. ass." represents oxide assisted growth, "ox. ass. + Au" represents oxide assisted growth with gold as a mediating catalyst and "C.V.D." represents chemical vapour deposition.

Table 4.2: Growth methods and the corresponding linear correlation factors for length versus diameter.

Sample	Growth Method	Linear Correlation Factor
Sample A	ox. ass.	.60
Sample B	ox. ass.	.63
Sample C	ox. ass. + Au	.13
Sample D	C.V.D.	.52
Sample E	C.V.D.	.13

In general, wide wires tend to grow to greater lengths than thin wires, as they are less prone to defects and kinks that can terminate growth [13]. Hence a large linear correlation factor between length and diameter can be an indicator of good quality nanowires, i.e. the wires are of relatively uniform morphology and free from kinks.

Analysis of Tables 4.1 and 4.2

Oxide assisted growth produced wires with a relatively high linear correlation factor. TEM images (including the many extra images not included in this report) show that Samples A and B consisted of wires of one morphology only, i.e. Sample A consisted of only chain-like wires and Sample B consisted of only tadpole-like wires, see Figures 4.3 and 4.4. This indicates that oxide assisted growth produces silicon nanowires of good quality.

Oxide assisted growth with gold as a mediating catalyst had a low linear correlation factor. TEM analysis obtained images of poor quality kinked wires, see Figure 4.5. Hence it appears that oxide assisted growth with gold as a mediating catalyst is not an appropriate method for producing good quality silicon nanowires.

Chemical vapour deposition for wires of large diameter (average = 44 nm) had a relatively high linear correlation factor, whereas for smaller diameter wires (average = 18 nm) the linear correlation factor was low. TEM analysis obtained images of good

quality kink-free nanowires for the larger diameter sample, see Figure 4.6. TEM analysis of the smaller diameter sample revealed the presence of bent and kinked nanowires, see Figure 4.7 . Hence the analysis indicates that C.V.D. produces good quality large diameter silicon nanowires, and poorer quality small diameter silicon nanowires. This is consistent with theory [13]. Chemical vapour deposition is based on the decomposition of a gas onto a substrate. When the gold on the substrate is heated, the gold and silicon form a eutectic, as per the vapour – liquid – solid (VLS) method. With the VLS method, larger diameter silicon nanowires contain less defects such as bends and kinks. Hence the smaller the nanowire diameter, the poorer the quality of the nanowires produced. The results presented here show that C.V.D. can produce good quality silicon nanowires of average diameter 44 nm, but it is not an appropriate method for producing small diameter silicon nanowires.

4.4 HRTEM Results

A selection of HRTEM images are presented here[2]. They illustrate the amorphous and crystalline regions in each sample type. Figure 4.13 shows the chainlike structure of Sample A. The crystalline spheres appear darker than the amorphous interconnects. In Figure 4.14 it is possible to see the lattice planes of the crystalline silicon, and the amorphous nature of the interconnects. Figure 4.15 clearly shows that a short range lattice plane of an alternate direction is present in the middle of a crystalline sphere. This is evidence of the presence of defects.

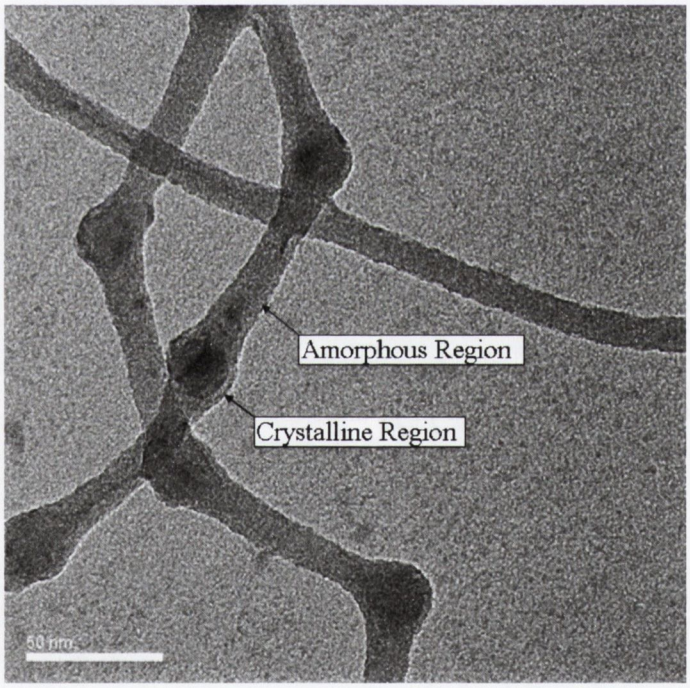

Figure 4.13: HRTEM image showing crystalline spheres and amorphous interconnects in Sample A.

Figure 4.16 shows how the crystalline lattice continues perfectly from the wire

[2]HRTEM was carried out in collaboration with specialist microscopists as outlined in Acknowledgements.

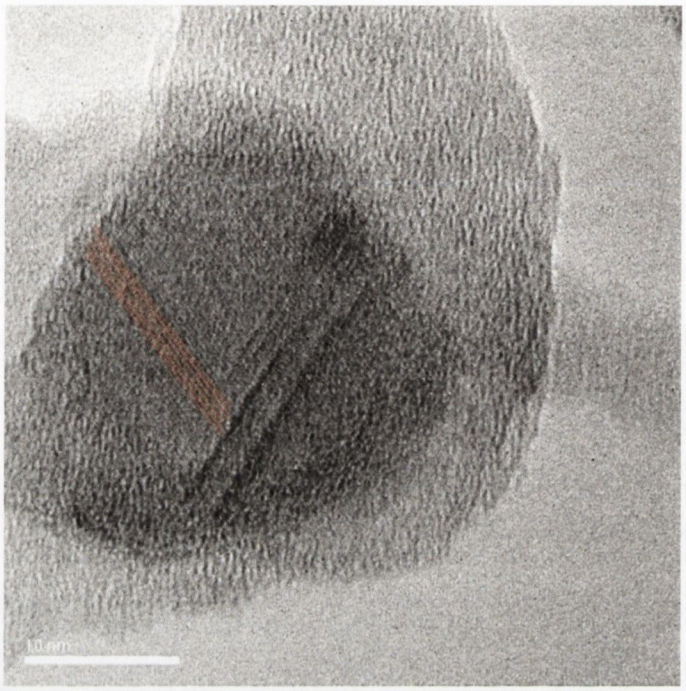

Figure 4.14: HRTEM image showing lattice planes in Sample A.

section of sample B into the sphere section, without a change in lattice direction or any observable defects. Figure 4.17 shows the regular lattice arrangement of the crystalline region of Sample B. An amorphous shell around the crystalline region is also visible in the image.

Samples C, D and E all consisted of crystalline silicon nanowires capped in SiO_x. Figure 4.18 illustrates the crystalline nature of the wire core, and the amorphous nature of the shell. Lines have been added to the image to highligh the lattice planes of the crystalline region.

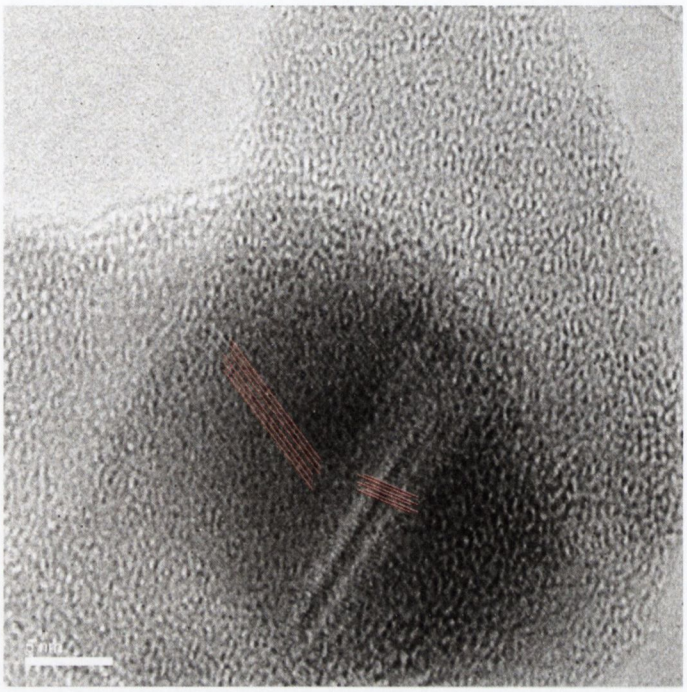

Figure 4.15: HRTEM image showing different lattice planes in a single crystalline sphere of Sample A.

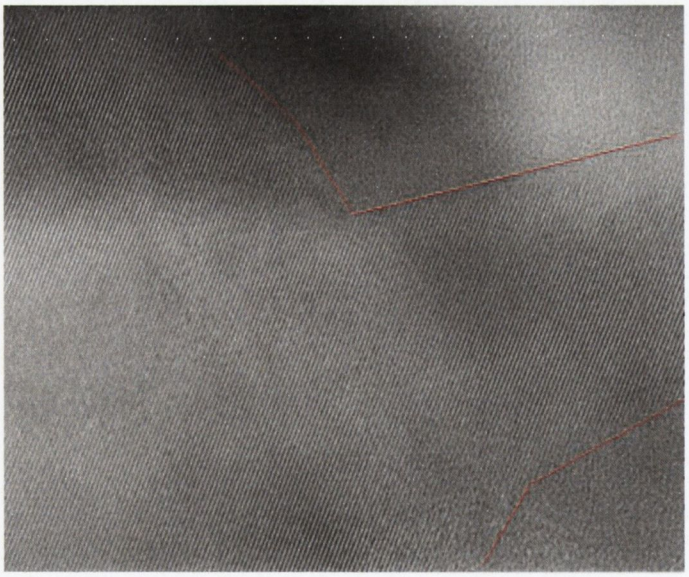

Figure 4.16: HRTEM image of Sample B, showing a crystalline wire and sphere structure.

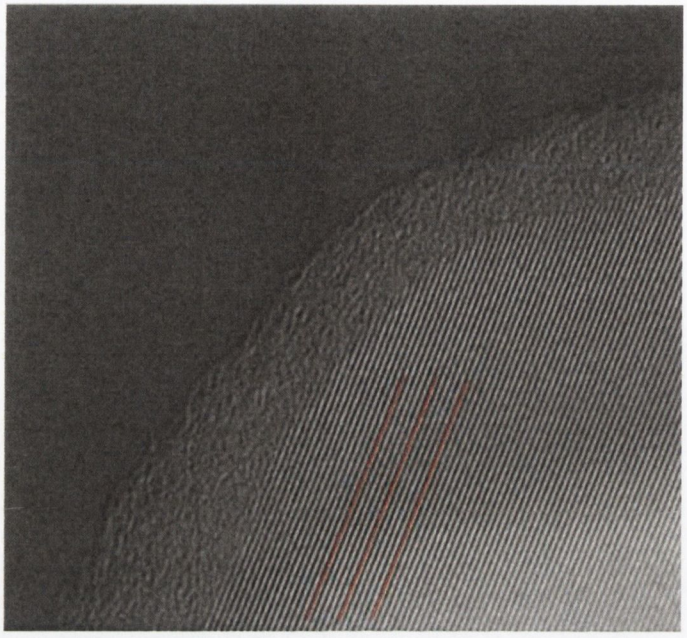

Figure 4.17: HRTEM image of the lattice planes in Sample B.

Figure 4.18: HRTEM image of a straight wire (Sample C).

4.5 Results from Additional Techniques

EFTEM and EELS were carried out on Sample A, the results of which are outlined in Setions 4.5.1 and 4.5.2 respectively.[3] The availability of additional Sample A in bulk form made Raman analysis possible, which is discussed in Section 4.5.3.[4]

4.5.1 EFTEM Results

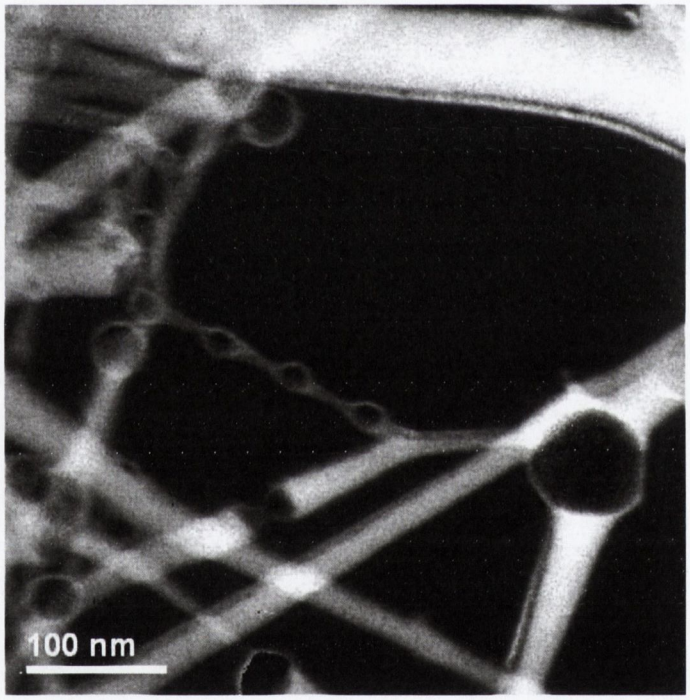

Figure 4.19: EFTEM image of Sample A.

Figure 4.19 shows the EFTEM analysis of Sample A. The spheres of crystalline silicon appear dark. The interconnects consist of SiO_x and appear bright. This is

[3]EFTEM and EELS were carried out by the manufacturer of Sample A.

[4]A portion of Sample A in bulk form was taken to the Focus Institute in the Dublin Institute of Technology. The Raman spectrum was obtained by a technician, Anne Shanahan.

consistent with the HRTEM analysis in Section 4.4

4.5.2 EELS Results

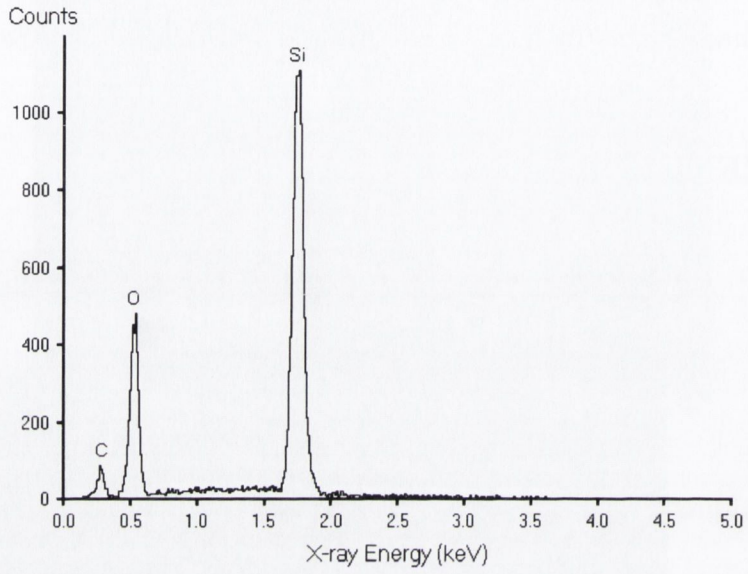

Figure 4.20: EELS spectrum of Sample A

From Figure 4.20 it is apparent that silicon and oxygen are present in the sample. The occurrence of carbon is due to the grid. The graph supports the manufacturers claim that there were no impurities present in the finished sample.

4.5.3 Raman Results

Raman analysis was performed on Sample A. The excitation source was a HeNe laser, with wavelength 632.817 nm. The laser power utilised was 2 mW.

A broad peak was produced by Sample A at 300 cm^{-1}, and is associated with the scattering of two transverse acoustic (2TA) phonons [8].

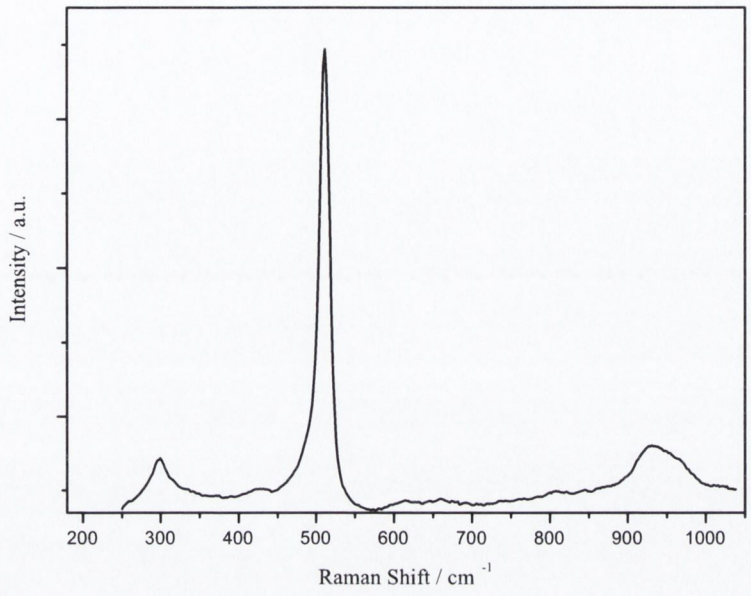

Figure 4.21: Raman spectrum of Sample A for laser excitation at 632.8 nm.

Sample A also produced a large peak at 512 cm^{-1}. Meier *et al.* [11] reported a shift of the first optical phonon peak (520 cm^{-1}) to 512 cm^{-1} for silicon nanoparticles 20 cm^{-1} in diameter. Li *et al.* [8] reported that the peak shifted to 511 cm^{-1} for crystal grain size of 15 nm. The average diameter of a crystalline sphere in Sample A is 21 nm (see Section 4.3.1). This is in good agreement with the nanoparticle size reported by Meier *et al.* [11] and Li *et al.* [8] for a similar frequency shift.

Meier *et al.* [11] observed a shift of the 2TO peak at 970 cm^{-1} towards lower frequencies with decreasing nanoparticle size. Sample A produced a peak at 930 cm^{-1}, which corresponds to the shift produced by silicon nanoparticles 16 nm in diameter, as reported by Meier *et al.* [11]. Sample A therefore shows evidence of phonon confinement, through the asymmetric broadening and downshifting of the Raman peaks. The magnitude of the downshift is consistent with observations made

by other groups on silicon nanostructures of similar diameters [8, 11].

4.6 Conclusions

Structural characterisation was carried out on five different nanowire samples. Length and diameter distributions of each nanowire sample were obtained through TEM analysis. Analysis of the nanowire/nanosphere diameters revealed that the nanostructures were too large to cause quantum confinement effects, as the crystalline structures were larger than the Bohr radius of silicon, which is 4.9 nm. It is possible that quantum confinement could be produced in small crystalline regions, or "grains" that exist within the larger crystalline regions, or from defects such as dislocations and grain boundaries [12].

TEM analysis combined with linear correlation function for length versus diameter of the nanowire samples was carried out. It revealed that oxide assisted growth produced good quality nanowires, but oxide assisted growth with gold as a mediating catalyst did not. Chemical vapour deposition produced good quality large diameter wires, but poor quality small diameter wires, which is consistent with theory [13].

Sample A underwent additional characterisation. The EFTEM analysis was in agreement with the findings of HRTEM, confirming that Sample A consisted of spheres of crystalline silicon surrounded and connected by amorphous silicon. EELS analysis showed that Sample A contained no observable impurities. This would suggest that the oxide assisted growth mechanism utilised to grow Sample A produces nanostructures of high purity. Raman spectroscopy provided evidence of phonon confinement in Sample A, through the asymmetric broadening and downshifting of the Raman peaks. The magnitude of the downshift is consistent with observations made

by other groups on silicon nanostructures of similar dimentions [8, 11].

Bibliography

[1] *Figure: TEM,* www.udel.edu/Biology/Wags/histopage/illuspage/lec1/iintro9.gif, *accessed December 2006* .

[2] *"The Transmission Electron Microscope," official web-site of the nobel foundation* http://nobelprize.org/educational_games/physics/microscopes/tem, *accessed December 2006* .

[3] *HRTEM,* http://en.wikipedia.org/wiki/Hrtem, *accessed December 2006* .

[4] *EFTEM,* http://www.smt.zeiss.com/, *accessed December 2006* .

[5] *EELS,* http://eels.kuicr.kyoto-u.ac.jp/eels.en.html, *accessed December 2006* .

[6] *Raman spectroscopy,* http://en.wikipedia.org/wiki/Raman_spectroscopy, *accessed December 2006* .

[7] *Figure: Raman scattering,* www.kosi.com/raman/resources/tutorial/, *accessed December 2006* .

[8] Li, B., Yu, D., and Zhang, S.-L. *Physical Review B* **59**(3).

[9] Piscanec, S., Ferrari, A., Cantoro, M., Hofmann, S., Zapien, J., Lifshitz, Y., Lee, S., and Robertson, J. *Materials Science & Engineering C, Biomimetic and Supramolecular Systems Current Trends in Nanoscience - From Materials to Application Symposium A, E-MRS Spring Metting 2003, 10-13 June 2003* **C23**(6-8), 931–4 (2003).

[10] Scheel, H., Reich, S., Ferrari, A., Cantoro, M., Colli, A., and Thomsen, C. *Applied Physics Letters* **88**(23), 233114–1 (2006).

[11] Meier, C., Luttjohann, S., Kravets, V., Nienhaus, H., Lorke, A., and Wiggers, H. *Physica E* **32**(1-2), 155–8 (2006).

[12] Bai, Z., Yu, D., Wang, J., and Zou, Y. *Materials Science & Engineering B (Solid-State Materials for Advanced Technology)* **72**, 117–120 (2000).

[13] Westwater, J., Gosain, D., Tomiya, S., Usui, S., and Ruda, H. *Journal of Vacuum Science & Technology B (Microelectronics and Nanometer Structures)* **15**(3), 554–7 (1997).

Chapter 5

Optical Limiting

5.1 Non-linear Optics

5.1.1 Non-linear Susceptibility

In the linear regime, the optical properties of a material, such as refractive index and absorption co-efficient, are independent of optical power. When a laser light source is utilised, the high power can result in the material under study displaying non-linear optical behaviour.

The optical properties of a material can be described by the real and imaginary parts of the dielectric constant ϵ_r, which can be derived as follows,

$$\mathbf{D} = \epsilon_0 \boldsymbol{\mathcal{E}} + \mathbf{P} \tag{5.1}$$

$$\mathbf{D} = \epsilon_0 \epsilon_r \boldsymbol{\mathcal{E}} \tag{5.2}$$

where $\mathbf{D}$ is the electric displacement, ϵ_0 is the permittivity of free space, $\mathbf{P}$ is the polarisation of the medium and $\boldsymbol{\mathcal{E}}$ depicts the electric field of the light wave.

In the linear regime, $\mathbf{P}$ has the following linear relationship with $\boldsymbol{\mathcal{E}}$,

$$\mathbf{P} = \epsilon_0 \chi \boldsymbol{\mathcal{E}} \tag{5.3}$$

where χ is the electric susceptibility. Combining Equations 5.2 and 5.3 gives

$$\epsilon_r = 1 + \chi \tag{5.4}$$

which is the standard form for representing the relationship between ϵ_r and χ.

If one considers a medium in which the polarisation is parallel to the electric field, the vector nature of $\mathbf{P}$ and $\boldsymbol{\mathcal{E}}$ can be ignored. In the non-linear regime, the polarisation P can be split into a first order response P^1, and a series of non-linear terms according to

$$P^{non-linear} = P^1 + P^2 + P^3 + ...P^n, \tag{5.5}$$

where P^n is the n^{th} order non-linear polarisation.

By introducing a non-linear susceptibility term $\chi^{(non-linear)}$, Equation 5.3 can be modified to become

$$P = \epsilon_0 \chi^{(non-linear)} \mathcal{E} = \epsilon_0 (\chi^{(1)} \mathcal{E} + \chi^{(2)} \mathcal{E}^2 + \chi^{(3)} \mathcal{E}^3 + ...), \tag{5.6}$$

where $\mathcal{E}$ is the magnitude of the applied field. Comparing Equations 5.4 and 5.6 gives

$$\epsilon_r^{non-linear} = 1 + \chi^{(non-linear)} \tag{5.7}$$

$$\epsilon_r^{non-linear} = 1 + \chi^{(1)} + \chi^{(2)} \mathcal{E} + \chi^{(3)} \mathcal{E}^2 + ... \tag{5.8}$$

hence the dielectric constant depends on the electric field through the non-linear susceptibilities [1].

Isotropic media such as gases, liquids and glasses possess inverse symmetry, which leads to the $\chi^{(2)}$ terms cancelling out and becoming zero. Hence for isotropic media, the lowest order non-linear susceptibility with non-vanishing components is $\chi^{(3)}$.

This representation of non-linear optical behaviour can be extended to include non-linear effects which result from processes other than the polarisation of the material responding non-linearly to the electric field of the incident light. If the non-linear optical behaviour of the material does not result from the non-linear response of the polarisation, it is referred to as an 'effective' χ response. Semi-conductor crystals often exhibit large effective $\chi^{(3)}$ coefficients due to the saturation of interband transitions and excitonic absorption [2]. Scattering mechanisms also produce an effective χ response.

5.1.2 Non-linear Refraction

Consider the following relationship [3],

$$P^{(3)} = \chi^{(3)}\mathcal{E}^3 \tag{5.9}$$

A monochromatic field is applied, of the form

$$\boldsymbol{\mathcal{E}} = \mathcal{E}\cos(\omega \cdot t) \tag{5.10}$$

Since

$$\cos^3 \omega t = \frac{1}{4}cos(3\omega t) + \frac{3}{4}\cos(\omega t) \tag{5.11}$$

the non-linear polarisation can be written in the form

$$P^{(3)} = \frac{1}{4}\chi^{(3)}\mathcal{E}^3\cos(3\omega \cdot t) + \frac{3}{4}\chi^{(3)}\mathcal{E}^3\cos(\omega \cdot t) \tag{5.12}$$

The first term in Equation 5.12 relates to third harmonic generation, where three photons of frequency ω are annihilated, creating one photon of frequency 3ω. The second term relates to the non-linear effect on the polarisation at the frequency of the incident field, and corresponds to a non-linear contribution to the refractive index.

In the linear regime, the refractive index can be expressed as follows

$$n_0^2 = 1 + \chi^{(1)} \tag{5.13}$$

Taking into account the third order contribution, Equation 5.13 becomes

$$n^2 = 1 + \chi^{(1)} + \chi^{(3)}\mathcal{E}^2 \tag{5.14}$$

This treatment was based on a parametric process, whereby the initial and final quantum mechanical states are the same and photon energy is conserved.

It is possible that the non-linear refractive index may change at incident wavelength. Equation 5.14 can be written as

$$n = n_0 + n_2 I \tag{5.15}$$

Self-focusing is the result of a non-linear response of the refractive index. Self-focussing can occur for a beam of non-uniform intensity distribution, e.g. a gaussian beam. For a positive n_2, the refractive index will be highest at the centre of the beam, causing the material to act as a convex lens [3]. It can be examined using the z-scan technique, which is discussed in Section 5.3.

5.1.3 Introduction to Optical Limiting

Non-linear optical materials are required for the production of photonic devices that control amplitude gain or extinction, polarisation, phase, reflection and refraction of light [4]. To this end, nanoscale silicon has been extensively studied, due to its CMOS compatibility and the enhancement of its non-linear effects due to quantum confinement [5].

An optical limiter displays high linear transmission for low input energy and low transmission for high input energy, as depicted in Figure 5.1 [6]. Applications of optical limiting materials include protective eye wear and protection of sensors from high light intensities, such as from laser beams.

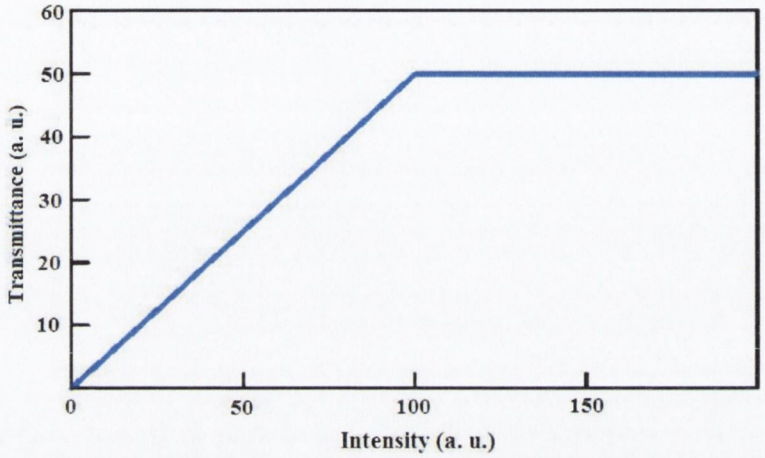

Figure 5.1: Response of an ideal optical limiter.

Optical limiting is usually attributed to effects such as reverse saturable absorption, non-linear refraction and thermal non-linearities or scattering. In the case of silicon, the non-linearities are usually attributed to two photon related absorption and $\chi^{(3)}$ variation related to quantum confinement effects [5, 7, 8, 9, 10].

Carbon black suspensions optically limit by a scattering process [11]. One proposed mechanism is that the carbon particles heat up as they absorb light, which causes them to ionise and produce microplasmas when the vaporisation temperature is reached. The microplasmas then scatter the light [12, 13, 14, 15]. Another mechanism may involve the carbon particles transferring the absorbed heat to the surrounding solvent. Initially, localised hot regions with a lower refractive index then the surrounding medium are produced. Increased heating creates bubbles which scat-

ter the light (see Figure 5.2 [16]) and this becomes the dominant limiting mechanism. This occurs below the vaporisation temperature of carbon [17, 18, 19].

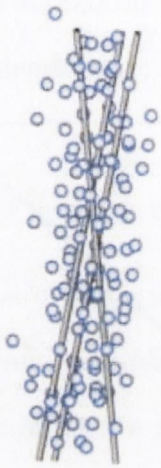

Figure 5.2: Bubble formation in solvent.

Laser induced breakdown in SiO_2 with pulse widths from 7 ns to 150 fs has been reported [20]. In this report it is proposed that optical limiting is occurring in suspensions of Si/SiO_2 nanostructures due to a scattering process. The scattering centres are most likely plasmas which are formed through ionisation of the SiO_2 outer shells.

It should be noted that Joudrier *et al.* attributed non-linear scattering in colloidal suspensions of silica particles to a photoinduced refractive index mismatch [21]. They used a mixture of toluene (refractive index 1.372) and hexane (refractive index 1.494) in the ratio 1:0.8 to closely match the refractive index of the solvent to that of silica (refractive index 1.455). It is unlikely that this mechanism is occurring in the system under study here. Spectroscopic grade isopropanol was used as the solvent, (refractive index 1.377) which is not close enough to the refractive index of the SiO_2 (refractive index 1.455) for this mechanism to be relevant.

5.2 The Z-Scan Technique

5.2.1 Introduction to Z-Scan

The z-scan technique consists of transporting the sample under study in the z direction, from a low intensity regime, through the focus of a laser (high intensity) and back out into the low energy regime. The light transmitted through the sample is recorded as a function of sample position, and hence laser intensity. The set-up is displayed in Figure 5.3.

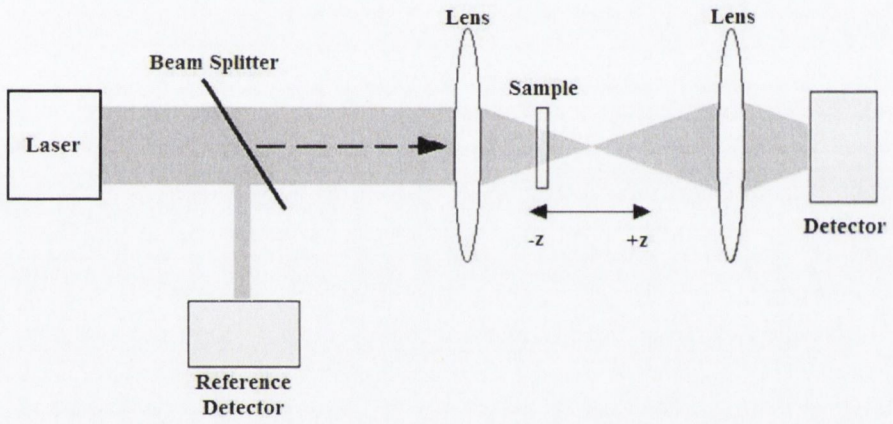

Figure 5.3: The z-scan technique.

An open aperture detector is used to detect losses such as scattering and absorption as the sample is transposed through the focus of the laser beam. When non-linear losses (non-electronic non-linear scattering and absorption) are occurring, plots of transmission intensity against z-scan position produce bell shaped curves, as illustrated in Figure 5.4, with the minimum of transmission occurring at the focus of the laser beam (z = 0).

A closed aperture is placed in front of the detector when the non-linear refractive

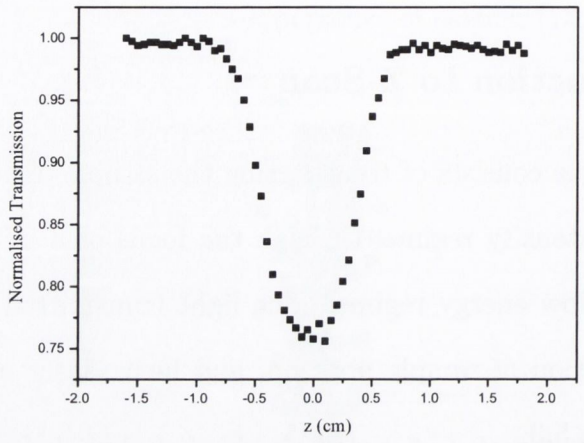

Figure 5.4: Open aperture z-scan.

index is of interest. Due to the Kerr lens effect, the laser pulses can experience self-focusing. Higher intensities on the beam axis, as compared to the wings of the beam, cause an effectively increased refractive index for the inner part of the beam. This modified refractive index distribution then acts like a focusing lens [22]. If self-focussing is occurring, then plots of transmission intensity against z-scan position produce valley-peak shaped curves, as illustrated in Figure 5.5 [23], with the minimum of transmission occurring before the focus of the laser beam (z = 0).

5.2.2 Results

Z-scan Curves

The non-linear optical properties of the five different silicon nanostructure dispersions were investigated by open and closed aperture z-scan with 6 ns Gaussian pulses at 532 nm from a frequency doubled, Q switched Nd:YAG laser. The beam waist radius

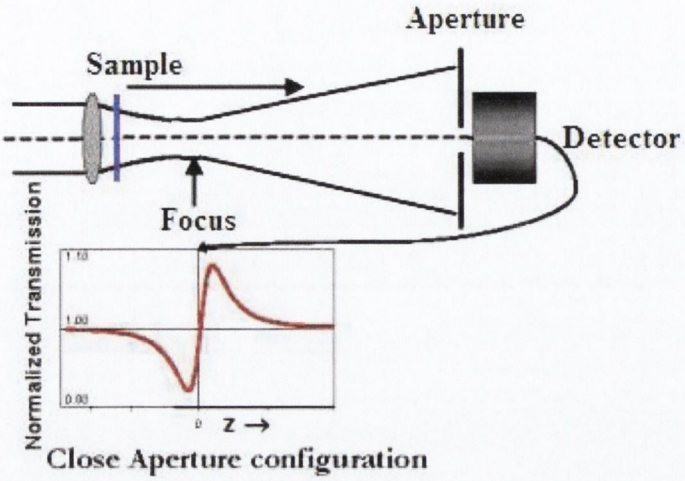

Figure 5.5: Closed aperture z-scan.

was 20 μm, and the pulse repetition rate was 10 Hz. The samples were held in a 1 cm cuvette. Since nanosecond pulses are being utilised, it is likely that the recorded responses are not the result of pure electronic non-linear optical effects. In the nanosecond regime, thermal effects may be a contributing factor.

Figure 5.6 shows a graph of normalised transmission against z position for Sample A, which is also representative of the response produced by Sample B. The transmission intensity for the open aperture scan was almost perfectly constant at low intensities, and the transmission decreased in the high intensity regime, producing a bell shaped curve. This is the response of an optically limiting material. The closed aperture z-scan produced a bell shaped curve, which indicates that non-linear changes in the refractive index were not the dominant optical limiting mechanism. The data obtained by closed aperture z-scan was divided by the data obtained by open aperture z-scan, and bell shaped curves were again produced. This reiterates the fact that the contribution from non-linear refraction is negligible. A peak-valley pattern, rather

than a bell-shaped pattern as was produced by the samples under study here, would be indicative of self focusing behaviour (See Figure 5.5). This is clearly not the case here. The optical extinction is dominated by non-linear losses. This response also occurred for Sample B. Therefore there is no evidence of a strong contribution to the limiting effect from non-linear refraction. The system appears to be dominated by non-linear losses, such as non-electronic non-linear scattering and absorption.

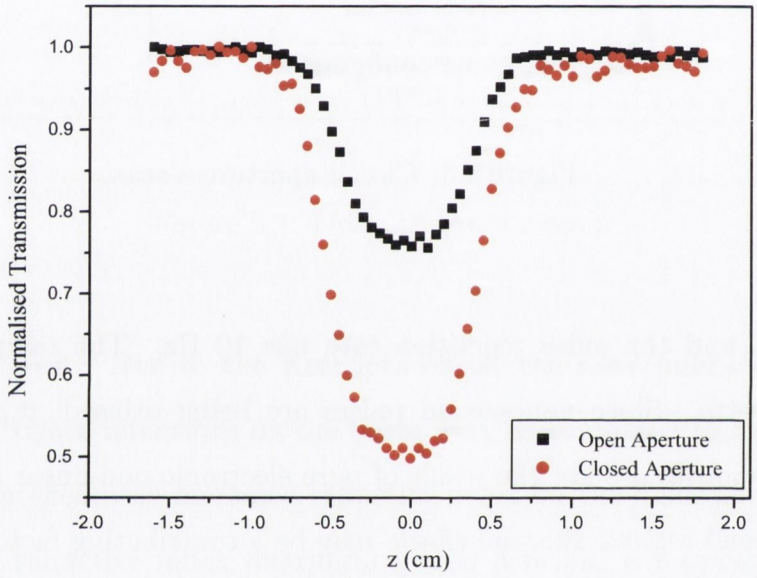

Figure 5.6: Normalised transmission against z position for Sample A.

Figure 5.7 shows a graph of normalised transmission against z position for Sample D, which is also representative of the response produced by Samples C and E. The bell shaped curve for the open aperture scan was not perfectly horizontal at low intensities, hence the material is not a perfect optical limiter. The same was true for Samples C and E, although Sample E displayed slightly better limiting behaviour than the other two samples. The closed aperture z-scan produced a bell shaped curve. The data obtained by closed aperture z-scan was divided by the data obtained by open aperture

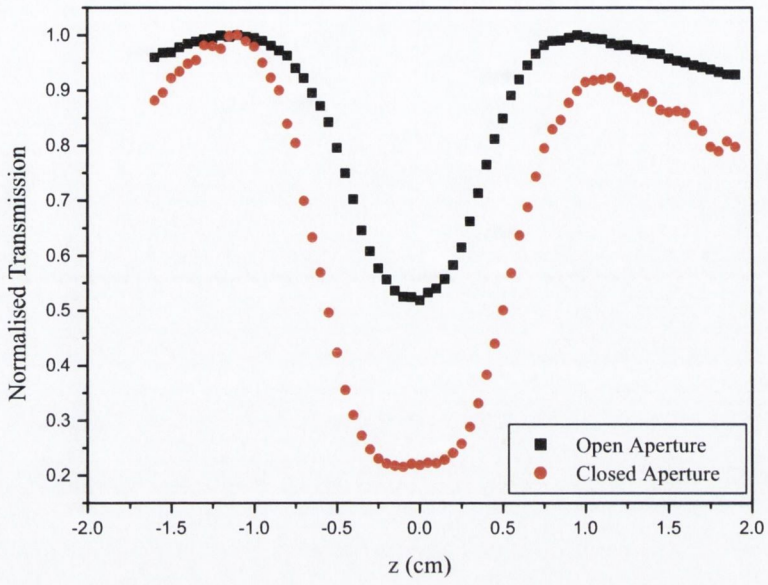

Figure 5.7: Normalised transmission against z position for Sample D.

z-scan, and bell shaped curves were produced indicating that the contribution from non-linear refraction is not contributing strongly to optical limiting. The optical extinction is caused by non-linear losses such as absorption and scattering. This response also occurred for Samples C and E.

Optical Limiting Properties

Figure 5.8 shows the normalised non-linear transmission for each sample, as a function of incident pulse energy density, as measured by open aperture z-scan. The normalised transmission was plotted against the energy density in a single pulse. The pulse energy density is defined as $F_{pulse} = E_{pulse} \; / \; [\pi\omega(z)^2]$, where E_{pulse} is the energy in a single pulse, and $\omega(z)$ is the radius of the propagating Gaussian pulse as a function of position z.

Samples A and B clearly exhibited optical limiting, with linear absorption dom-

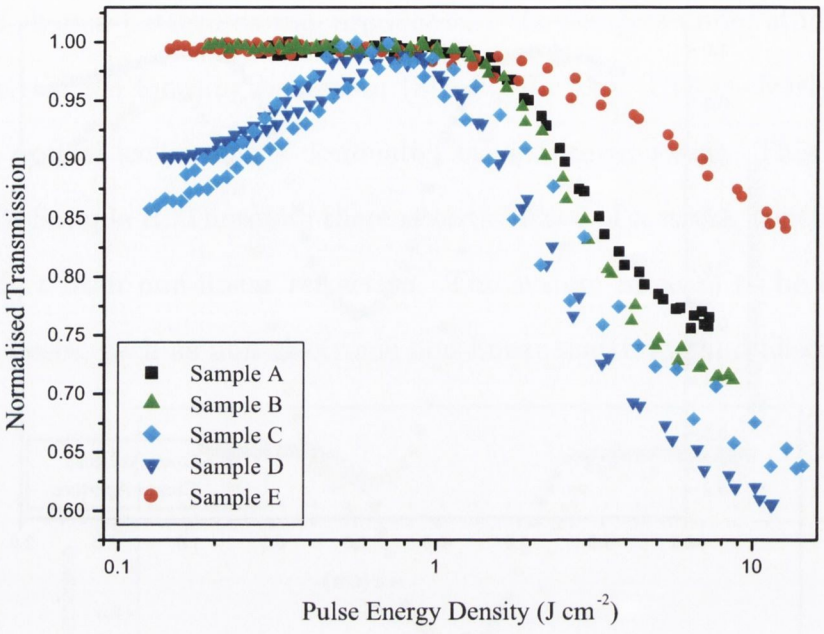

Figure 5.8: Transmission of each sample as a function of incident pulse energy density.

inating until a threshold limit was reached, at which point the samples started to display non-linear extinction. Samples C and D did not display linear absorption at lower intensities, but they did start to show increased absorption around the same threshold energy as Samples A and B. Sample C did not display linear absorption at low intensities either, but this is not clearly displayed in Figure 5.8, where only a slight scatter of points is visible. Analysis of the open aperture z-scan (bell shaped) curves for Sample E confirmed that it behaved similarly to Samples C and D, although the deviation from linear absorption at lower intensities was not as marked as for Samples C and D. This deviation from linear behaviour could be the result of saturable absorption. Investigation of optical absorption in the linear regime was carried out. The results are presented in *Chapter 6: Linear Optical Characterisation I - Absorption Spectroscopy.* Absorption at 532 nm (2.33 eV) in the linear regime was

weak for Samples A and B, slightly stronger for Sample E, and strongest for Samples C and D. Hence the samples most likely to experience saturable absorption at high light intensities at 532 nm would be Samples C and D, followed by Sample E, with Samples A and B least likely to undergo saturable absorption. This corresponds to the results presented in Figure 5.8.

Evaluation and Comparison of Effective Imaginary $\chi^{(3)}$

The effective imaginary $\chi^{(3)}$ values for each sample were calculated at a number of different incident light intensities. The effective intensity dependent non-linear absorption co-efficients, β_{eff}, were extrapolated by applying a curve fitting method, developed by Seán O'Flaherty [24], to the open aperture z-scan curves. The effective imaginary $\chi^{(3)}$ can be expressed as

$$Im\{\chi^{(3)}_{eff}\} = \frac{n_0^2 \epsilon_0 c^2 \beta_{eff}}{\omega} \tag{5.16}$$

where n_0 is the linear refractive index, ϵ_0 is the permittivity of free space, c is the speed of light and ω is the angular velocity of the incident light.

Figure 5.9 shows the effective imaginary $\chi^{(3)}$ values of each of the samples as a function of incident light intensity. Samples C and D have 4 points on the graph rather than 5, as they did not exhibit good optical limiting performance at low incident light intensity.

Tables 5.1 – 5.5 contain the calculated effective imaginary $\chi^{(3)}$ values of each sample over a range of incident light intensities. An average effective imaginary $\chi^{(3)}$ value for each sample is also shown in the tables.

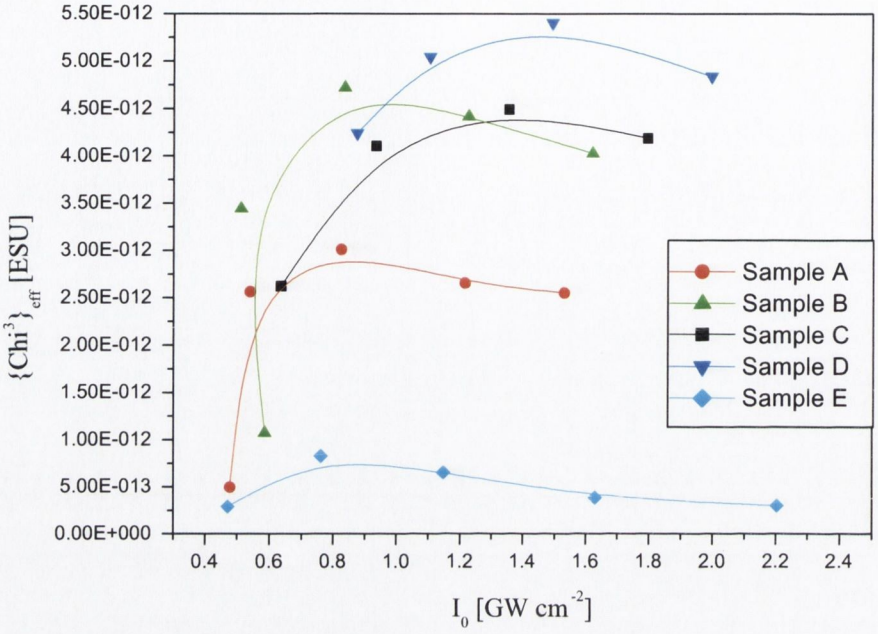

Figure 5.9: Effective imaginary $\chi^{(3)}$ values of each sample as a function of incident intensity.

Table 5.1: Effective imaginary $\chi^{(3)}$ values for various incident intensities, Sample A.

$\mathbf{I}_0$ [GW cm^{-2}]	Im$\{\boldsymbol{\chi}^{(3)}_{eff}\}$ [e.s.u.]
0.47809	4.91388×10^{-13}
0.54021	2.55736×10^{-12}
0.82581	3.00636×10^{-12}
1.21599	2.65234×10^{-12}
1.53136	2.55054×10^{-12}
Average	2.2516×10^{-12}

Table 5.2: Effective imaginary $\chi^{(3)}$ values for various incident intensities, Sample B.

$\mathbf{I}_0$[GW cm^{-2}]	Im$\{\boldsymbol{\chi}^{(3)}_{eff}\}$[e.s.u.]
0.58478	1.07039×10^{-12}
0.51096	3.44009×10^{-12}
0.83466	4.71894×10^{-12}
1.22509	4.41537×10^{-12}
1.6206	4.02808×10^{-12}
Average	3.53457×10^{-12}

Table 5.3: Effective imaginary $\chi^{(3)}$ values for various incident intensities, Sample C.

$\mathbf{I}_0$[GW cm^{-2}]	Im$\{\boldsymbol{\chi}^{(3)}_{eff}\}$[e.s.u.]
0.63514	2.62178×10^{-12}
0.93454	4.10545×10^{-12}
1.35357	4.49206×10^{-12}
1.79515	4.18686×10^{-12}
Average	3.85154×10^{-12}

Table 5.4: Effective imaginary $\chi^{(3)}$ values for various incident intensities, Sample D.

$\mathbf{I}_0$[GW cm^{-2}]	Im$\{\boldsymbol{\chi}^{(3)}_{eff}\}$[e.s.u.]
0.87433	4.23791×10^{-12}
1.10366	5.04553×10^{-12}
1.49017	5.40468×10^{-12}
1.99608	4.84139×10^{-12}
Average	4.88238×10^{-12}

Table 5.5: Effective imaginary $\chi^{(3)}$ values for various incident intensities, Sample E.

$\mathbf{I}_0$[GW cm^{-2}]	Im$\{\boldsymbol{\chi}^{(3)}_{eff}\}$[e.s.u.]
0.47064	2.84845×10^{-13}
0.76097	8.25873×10^{-13}
1.14642	6.52098×10^{-13}
1.6298	3.87122×10^{-13}
2.20291	3.05626×10^{-13}
Average	3.05626×10^{-13}

Table 5.6 contains an order of magnitude comparison of $\chi^{(3)}$ values calculated for various optical limiting materials. TPP (tetraphenylporphyrin), PPIX (protoporphyrin IX) and SWNT(single wall nanotubes) were analysed in solutions of DMF (dimethylformamide), and the $\chi^{(3)}$ values shown are effective imaginary values, as are the values for Samples A, B, C, D and E. The rest of the samples were characterised in the form of thin films, and the values are absolute. The values shown for each material in Table 5.6 were obtained at a wavelength of 532 nm.

Table 5.6: Order of magnitude comparison of the $\chi^{(3)}$ values of various materials.

Sample	$\boldsymbol{\chi^{(3)}}$ [e.s.u.]	**Ref.**
SiO_2-Au-TiO_2	$\times 10^{-6}$	[25]
Au-SiO_2	$\times 10^{-6}$	[25]
Au-TiO_2	$\times 10^{-7}$	[25]
Au	$\times 10^{-9}$	[26]
Samples A, B, C, D	$\times 10^{-12}$	
Sample E	$\times 10^{-13}$	
TPP	$\times 10^{-13}$	[27]
PPIX	$\times 10^{-13}$	[27]
SWNT	$\times 10^{-13}$	[27]
Fused silica	$\times 10^{-14}$	[28]

5.2.3 Summary

Silicon nanowires with silicon dioxide shells in an isopropanol dispersion display optical limiting properties. Nanowires with nanospherical inclusions are particularly good optical limiters. They displayed linear absorption characteristics at low incident laser energies and enhanced, non-linearly scaled absorption at high incident laser energies. Z-scan analysis indicated that non-linear refraction does not contribute significantly to the limiting process. The optical extinction is the result of non-linear losses caused by absorption and/or scattering.

The threshold energy at which each sample started to undergo non-linear optical extinction was very similar. If the extinction were being caused by two photon absorption or the enhancement of $\chi^{(3)}$ effects due to quantum confinement, then the threshold energy would be dependent on the band-structure, and hence the morphology of each of the samples. Since this is clearly not the case, the non-linear extinction is likely to be the result of a surface effect, such as laser induced breakdown of the silicon oxide shell. The z-scan technique was also carried out at 1064 nm. No response was achieved from any of the samples. This result strengthens the hypothesis that the non-linear behaviour has a sizable non-electronic component.

Du *et al.* demonstrated laser induced breakdown and plasma formation from bulk SiO_2 in a vacuum. The sample was mounted on a translation stage and probed with a 7 ns-150 fs pulses from a 780 nm laser [20]. In the study presented here, a 532 nm Nd:YAG laser with 6 ns pulses was used to probe each sample. It is possible that laser induced breakdown, which is depicted in Figure 5.10 [29], is occurring at the SiO_2 outer shell. This would cause plasma formation which scatters the light non-linearly, in this case at pulse energy densities above 1.5 Jcm^{-2} (see Figure 5.8).

The effective imaginary $\chi^{(3)}$ values calculated for Samples A, B, C and D were of the order of 10^{-12} e.s.u., and 10^{-13} e.s.u. for Sample E. This implies that the optical limiting capabilities of the dispersions are not nearly as good as for gold nanostructure composites [25], but the capabilities are comparable to optically limiting porphyrins [27].

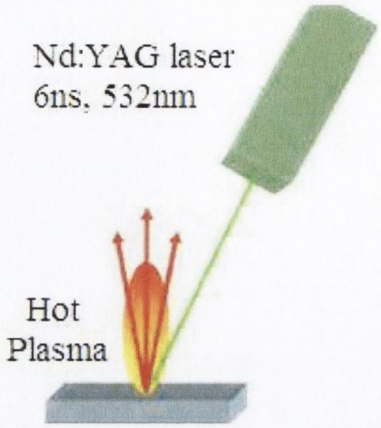

Figure 5.10: Laser induced breakdown of silicon oxide.

5.3 Scattering

5.3.1 Introduction to Light Scattering

The scattering of light by molecules and very small particles ($< 1/10$ wavelength of light) is predominantly Rayleigh scattering. Rayleigh scattering is wavelength dependent (hence the blue colour of the sky which is due to enhanced scattering of wavelengths towards the red end of the visible spectrum). The scattered light forms approximately equally large front and back scattered lobes. For larger particle sizes Mie scattering dominates. Mie scattering is not strongly wavelength dependent. It produces a large front scattered lobe, and a smaller back scattered lobe [30]. The scattering patterns produced by Rayleigh and Mie scattering are illustrated in Figure 5.11 [30].

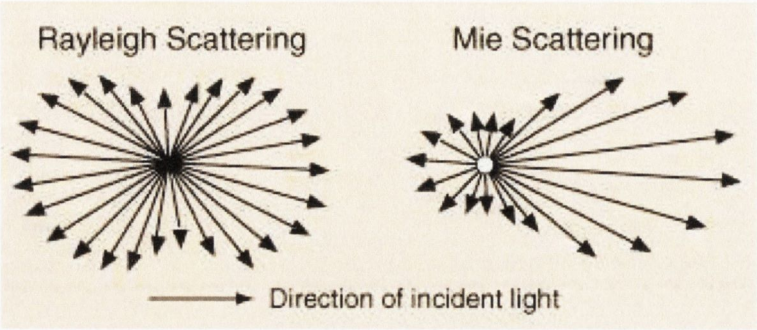

Figure 5.11: Rayleigh and Mie scattering.

5.3.2 Scattering Experiments

An additional investigaion was carried out on Sample A, in order to establish whether the intensity of the light scattered by the sample scaled non-linearly with incident laser intensity.

Angular Dependent Scattering

The sample was placed at the focus of the z-scan beam. The incident laser beam was kept at a constant intensity, at a pulse energy density of 7.3 Jcm^{-2}. The intensity of the scattered light was measured as a function of angular position around the sample, as outlined in figure 5.12.

Intensity Dependent Scattering

Intensity dependent scattering was carried out to observe the onset of non-linear behaviour. The apparatus illustrated in Figure 5.12 was utilised for this study. The detector and scattering arm were moved to 50 degrees off the horizontal axis, so that light scattered by the sample would be falling on the detector. The intensity of

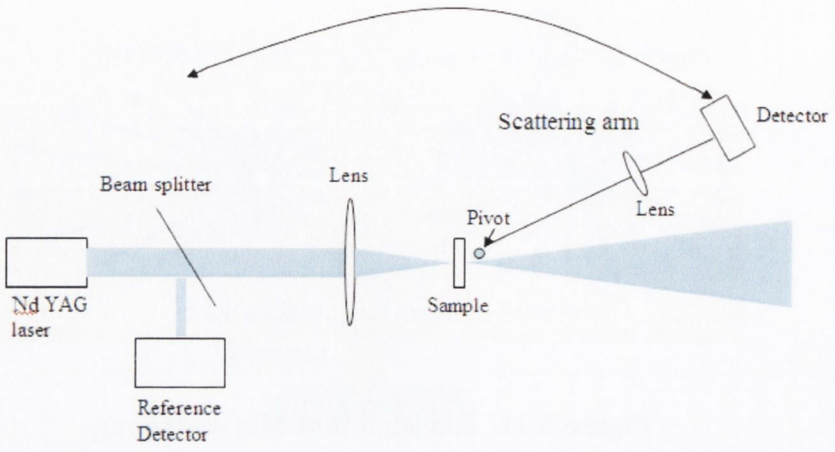

Figure 5.12: Scattering apparatus.

the scattered light was recorded while the intensity of the incident laser beam was incrementally increased.

5.3.3 Results

Angular Dependent Scattering

The intensity of the scattered light was measured as a function of angular position around the sample. The scattering profile obtained was characteristic of Mie scattering, with a pronounced front lobe and a diminutive rear lobe. A polar plot of angular dependent scattered light intensity is displayed in Figure 5.13.

Intensity Dependent Scattering

The intensity of the scattered light was recorded while the intensity of the incident laser beam was incrementally increased. The onset of non-linear dissipation of light also marked an increase in the intensity of the scattered signal, as demonstrated in

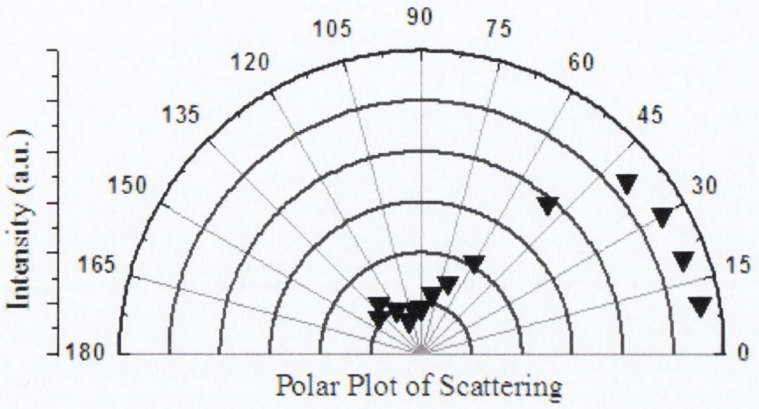

Figure 5.13: Angular dependent scattering at a pulse energy density of 7.3 Jcm^{-2}.

Figure 5.14. The scattered signal scaled non-linearly to pulse energy density. Hence non-linear scattering is clearly a contributing factor to the non-linear dissipation.

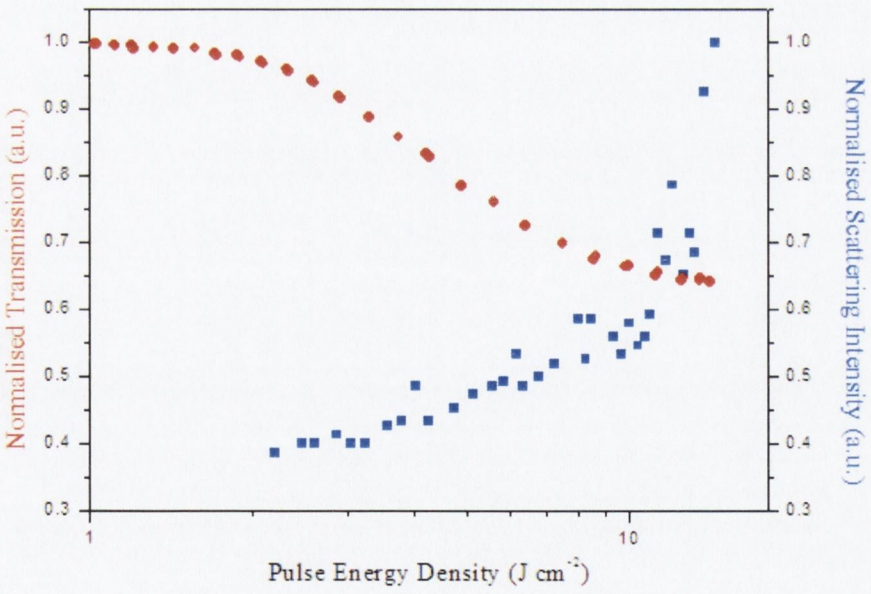

Figure 5.14: Intensity dependent scattering.

5.4 Summary

Oxide coated silicon nanoclusters in an IPA suspension display good optical limiting properties, with nanowires that contain spherical inclusions (Samples A and B) displaying enhanced optical limiting capabilities. It is unlikely that the optical limiting arises from photoinduced refractive index mismatch, as reported for colloidal suspensions of silica particles. The intensity of the scattered light scaled non-linearly to incident pulse energy density, and hence contributed to optical limiting. It is likely that the non-linear scattering has a strong contribution from plasmas which act as scattering centres. These plasmas are probably formed by laser induced breakdown of the nanostructure's SiO_2 outer shells.

Effective $\chi^{(3)}$ values were calculated for each of the samples. The optical limiting capabilities of the dispersions were comparable to some optically limiting porphyrins [27].

Bibliography

[1] Fox, M. *Optical Properties of Solids, p. 227,228.* Oxford University Press, (2001).

[2] Fox, M. *Optical Properties of Solids, p. 249.* Oxford University Press, (2001).

[3] Brennan, M. *Thesis: Multiphoton processes in a series of designer organic materilas, Trinity College Dublin* (2001).

[4] O'Flaherty, S., Hold, S., Brennan, M., Cadek, M., Drury, A., Coleman, J., and Blau, W. *Journal of the Optical Society of America B (Optical Physics)* **20**(1), 49–58 (2003).

[5] Liu, N.-N., Sun, J.-M., Pan, S.-H., Chen, Z.-H., Shi, W.-S., Wang, R.-P., and Wang, X.-G. *Optics Communications* **176**(1-3), 239–43 (2000).

[6] *Figure: An ideal optical limiter* `http://www.phys.utk.edu/`, *accessed Febuary 2007* .

[7] Prakash, G. V., Cazzanelli, M., Gaburro, Z., Pavesi, L., Iacona, F., Franzo, G., and Priole, F. *Journal of Applied Physics* **91**(7), 4607 (2002).

[8] Lettieri, S., Fiore, O., Maddalena, P., Ninno, D., Di Francia, G., and La Ferrara, V. *Optics Communications* **168**(5-6), 383–91 (15).

[9] He, J., Ji, W., Ma, G., Tang, S., Elim, H., Sun, W., Zhang, Z., and Chin, W. *Journal of Applied Physics* **95**(11 I), 6381–6386 (2004).

[10] Chemla, D. and Miller, D. *Optics Letters* **11**(8), 522–4 (1986).

[11] Durand, O., Grolier-Mazza, V., and Frey, R. *Optics Letters* **23**(18), 1471–3 (15).

[12] Mansour, K., Van Stryland, E., and Soileau, M. In *Materials for Optical Switches, Isolators and Limiters, 28-29 March 1989, Proc. SPIE - Int. Soc. Opt. Eng.*, volume 1105, 91–102, (1989).

[13] Mansour, K., Van Stryland, E., and Soileau, M. In *Electro-Optical Materials for Switches, Coatings, Sensor Optics, and Detectors, 16-20 April 1990, Proc. SPIE - Int. Soc. Opt. Eng.*, volume 1307, 350–62, (1990).

[14] Mansour, K., Soileau, M., and Van Stryland, E. *Journal of the Optical Society of America B (Optical Physics)* **9**(7), 1100–9 (1992).

[15] Xia, T., Dogariu, A., Mansour, K., Hagan, D., Said, A., Van Stryland, E., and Shi, S. In *Nonlinear Optical Liquids, 5-6 Aug. 1996, Proc. SPIE - Int. Soc. Opt. Eng.*, volume 2853, 142–8, (1996).

[16] *Figure: Bubble formation in solvent* `http://www.mse.mtu.edu/ wangh/cnt/cnt1.html`, *accessed Febuary 2007* .

[17] McEwan, K. and Madden, P. *Journal of Chemical Physics* **97**(11), 8748–59 (1992).

[18] Lowen, H. and Madden, P. *Journal of Chemical Physics* **97**(11), 8760–6 (1992).

[19] Fein, A., Kotler, Z., Bar-Sagi, J., Jackel, S., Shaier, P., and Zinger, B. In *FRISNO 3. 3rd French-Israeli Symposium on Nonlinear-Optics, 6-10 Feb. 1994, Nonlinear Optics, Principles, Materials, Phenomena and Devices*, volume 11, 277–88, (1995).

[20] Du, D., Liu, X., Korn, G., Squier, J., and Mourou, G. *Applied Physics Letters* **64**(23), 3071–3 (1994).

[21] Joudrier, V., Bourdon, P., Hache, F., and Flytzanis, C. *Applied Physics B (Lasers and Optics)* **B70**(1), 105–9 (2000).

[22] *Self-focusing* `http://www.rpphotonics.com/self_focusing.html`, *accessed March 2007* .

[23] *Figure: Closed aperture z-scan* `http://www.fresnel.fr/perso/billard/zscan.gif`, *accessed March 2007* .

[24] O'Flaherty, S. *Thesis: Nonlinear Optical extinction in polymer-carbon nanotube and phthalocyanine systems, Trinity College Dublin* (2003).

[25] Liao, H., Lu, W., Yu, S., Wen, W., and Wong, G. K. *Journal of the Optical Society of America B* **22**(9), 1923–1926 (2005).

[26] Couris, S., Xenogiannopoulou, E., Aloukos, P., Kaminska, E., Piotrowska, A., and Dynowska, E. *Optics Communications* **275**(1), 217–22 (2007).

[27] Ni Mhuircheartaigh, E., Giordani, S., and Blau, W. *Journal of Physical Chemistry B* **110**(46), 23136–41 (2006).

[28] Kanemitsu, Y., Okamoto, S., and Mito, A. *Physical Review B* **52**(15), 10752–5 (1995).

[29] *Figure: Laser induced breakdown* http://www.piacton.com/spectroscopy/, *accessed Febuary 2007* .

[30] *Rayleigh and Mie scattering* http://hyperphysics.phy-astr.gsu.edu/hbase/hframe.html, *accessed Febuary 2007* .

Chapter 6

Linear Optical Characterisation I - Absorption Spectroscopy

6.1 Introduction to Absorption Spectroscopy

Absorption spectroscopy is based on the absorption of light by a material through the promotion of an electron to a higher energy level within the material. The technique provides information regarding what energies are preferentially absorbed by a material, and hence provides information on the band structure of the system.

6.2 Quantum Theory

The energy levels in an atom or molecule are discrete, as are the vibrational energy levels. If an electron is to jump to a higher energy level, then the energy of the photon initiating the jump must be greater than or equal to the energy difference between the two levels. The energy of a photon is given by Equation 6.1,

$$e = hv, \tag{6.1}$$

where e is the energy of the photon, h is Plank's constant and v is the frequency of the photon [1].

The vibrational energy levels of a molecule are much closer together than the electronic energy levels. Photons of a lower energy than that needed for a change in the electronic structure of a molecule can therefore cause a change in the vibrational energy of the molecule. Infra red light contains sufficient energy to cause vibrational changes. Rotational energy levels are even more closely spaced than the vibrational energy states. Far infra red and microwave radiation can cause rotational changes.

Ultra violet - visible (UV-Vis) absorption spectra tend to consist of broad humps, rather than a series of sharp lines. This is because, in addition to the narrow peaks due to electronic transitions, there are also numerous transitions due to vibrational and rotational transitions. If a photon arrives with an energy not exactly equal to that required for a pure electronic transition, then the leftover energy can be used for a vibrational or rotational transition. So in a UV-Vis absorption spectrum there may be absorption lines due to electronic transitions, a larger number of vibrational lines in between them, and an even larger number of rotational lines filling in the gaps. In addition to this, the molecules of many materials exert forces on each other when in solution. This can slightly alter the extremely large number of energy levels and blur the spectral lines into bands [1].

6.3 The Beer-Lambert Law

The Beer-Lambert law states that the concentration of a substance in solution is directly proportional to the absorbance of the solution. For a sample under study in a spectrometer (see Section 6.4), the absorbance will be related to the length of the sample cell and the concentration of the solution. If I_0 is the intensity of the incident radiation and I is the intensity of the transmitted radiation, then I/I_0 is the transmittance, T. This is often expressed as percentage transmittance. The data obtained from a UV-Vis spectrometer can be expressed in terms of absorbance,

$$A = \log_{10}\left(\frac{I_0}{I}\right) = \log_{10}\left(\frac{100}{T}\right) = kcL,$$

where A is absorbance, L is the path length of the sample, c is the concentration of absorbing material and k is the extinction co-efficient. The extinction co-efficient is a constant dependant on the nature of the molecule and the wavelength of the radiation [1].

6.4 The UV-Vis Absorption Spectrometer

A UV-Vis absorption spectrometer is used to record a material's absorption spectrum. Figure 6.1 [2] illustrates the set-up for obtaining the absorption spectrum of a sample in solution. Usually two light sources are used in conjunction with each other. A tungsten lamp tends to be used as the white light source, and a deuterium lamp as the ultraviolet light source. The light sources illuminate the material, and the light that is not absorbed completely by the material is detected at the other side of the sample. A grating or filter in front of the sample allows you to illuminate the sample selectively, by breaking up the light source into its constituent wavelengths. A detector at the

other side of the sample detects the intensity of transmission at different wavelengths. Some wavelengths may be attenuated by the sample, and some may be completely absorbed. A reference of the solvent is used in conjunction with the sample under study. The background absorption due to the solvent can automatically be subtracted from the absorption profile by the spectrometer's accompanying software.

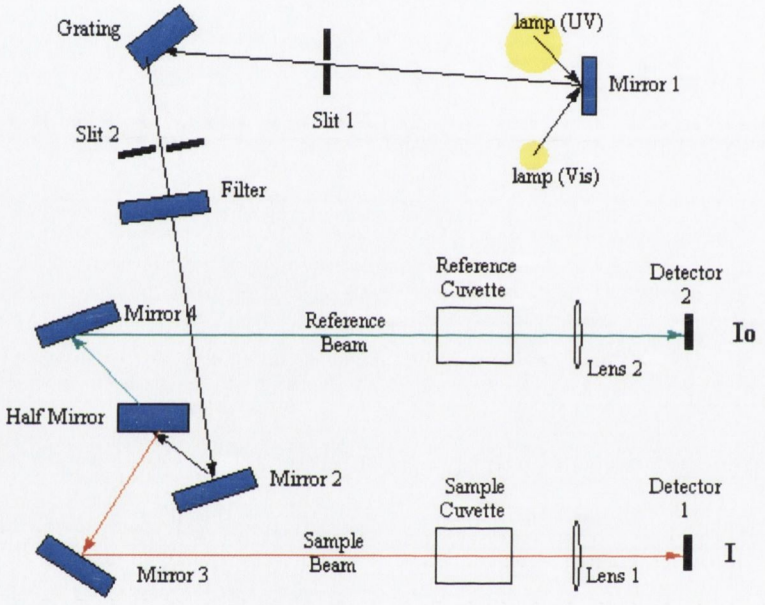

Figure 6.1: The UV-Vis absorption spectrometer

6.5 Silicon Absorption

Absorption by bulk silicon is particularly strong at the E_1 (3.5 eV) and E_2 (4.4 eV) points, where the conduction and valence bands are parallel. Absorption at E_g (1.1 eV) is negligible as this transition is indirect. The long absorption tail between 1.2 and 3 eV is indicative of the indirect nature of the band-gap [3]. Additional information

regarding transitions in silicon is available in *Chapter 2*, section 2.2.5, *"Silicon Band Structure"*. Figure 6.2 shows the typical absorption spectrum for bulk silicon at 300 K [4].

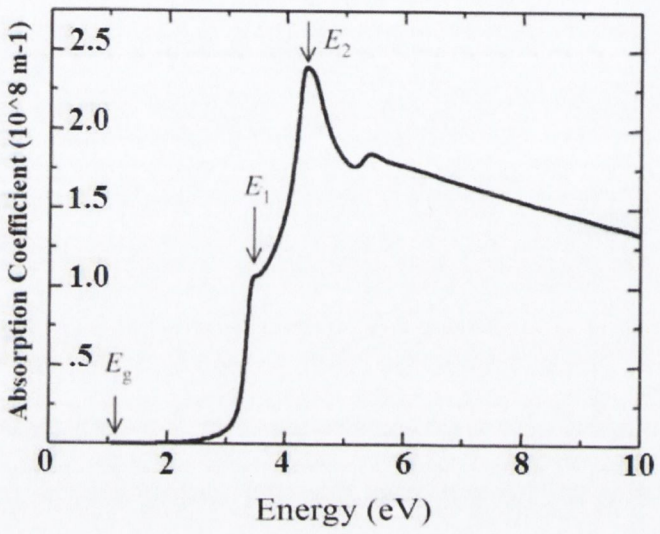

Figure 6.2: Silicon absorption spectrum

Quantum confinement influences the absorption spectrum of silicon. Blue-shift of the $\Gamma - X$ ($E = 1.1$ eV) and $X_4 - X_1$ ($E = 4.4$ eV) transitions is due to quantum confinement [3, 5]. Although the $\Gamma - X$ transition itself may not be apparent, the effect can manifest itself in the blue-shift of the absorption onset after the $\Gamma - X$ point. For additional information regarding quantum confinement, see *Chapter 2*, section 2.3.4.

Quantum confinement also causes a red-shift of the $\Gamma_{25} - \Gamma_{15}$ ($E = 3.4$ eV) transition [3, 5, 6]. This is contrary to the effect usually produced by quantum confinement, where the band-gap energy increases in the confined regime. This unusual effect occurs in silicon due to the saddle point structure of the (indirect) band-gap. Rama

Krishna and Friesner carried out a nonlocal and energy dependent pseudopotential based study on the effect of size on spectroscopic transitions in silicon clusters [6]. They discovered that the direct electronic transitions in the clusters is to the red of the corresponding transition in bulk silicon. They also predicted that the redshift increases with decreasing cluster size. Experimentally, Holmes *et al* has observed a 0.2 eV red-shift in the $\Gamma_{25} - \Gamma_{15}$ transition for silicon clusters 1.5 nm in diameter [5].

6.6 Results

Absorption spectrometry was carried out on each of the five samples in IPA solution. The dispersions were then left to stand for 2 months, so that oxidation would occur. Absorption spectroscopy was then carried out on the oxidised samples. The absorption spectrum of each pristine and oxidised sample were compared, to see if any observable changes occurred to the absorption spectra of the samples upon oxidation. The absorption spectra were obtained using a Shimatzu absorption spectrometer. Each sample was studied in a 1cm quartz cuvette, in IPA solution. (Absorption intensity is given in arbitrary units and the spectra are normalised to the baseline.)

6.6.1 Sample A

Figure 6.3 shows the absorption spectrum for Sample A. Figure 6.4 includes an inset illustrating the absorption onset of the sample, and shows two small shoulders that appeared in the oxidised sample's spectrum, which will be discussed later.

Both Oxidised and Pristine Sample A exhibited points of inflection near the direct band-gap energies of bulk crystalline silicon [7, 8]. The absorption onset ($\Gamma - X$) of Oxidised Sample A was blue-shifted by 0.2 eV from that of the pristine sample. This

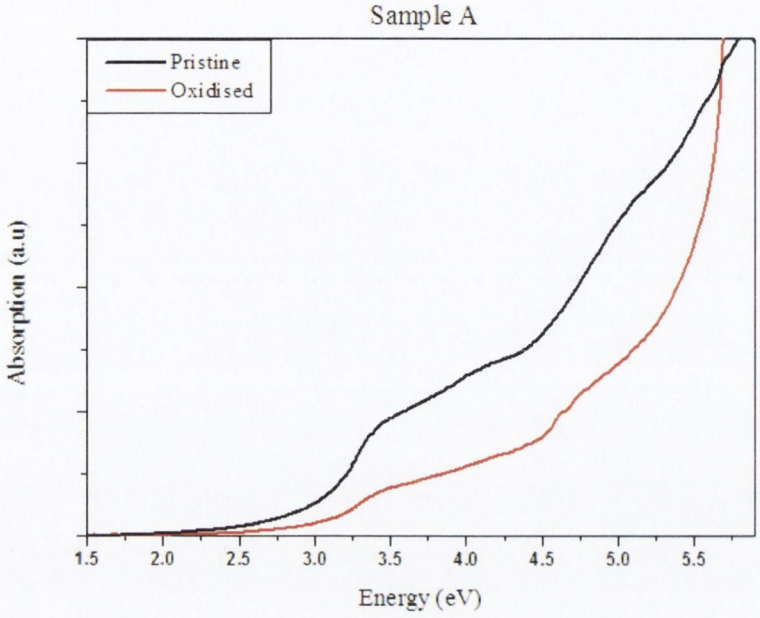

Figure 6.3: Absorption spectrum of Sample A

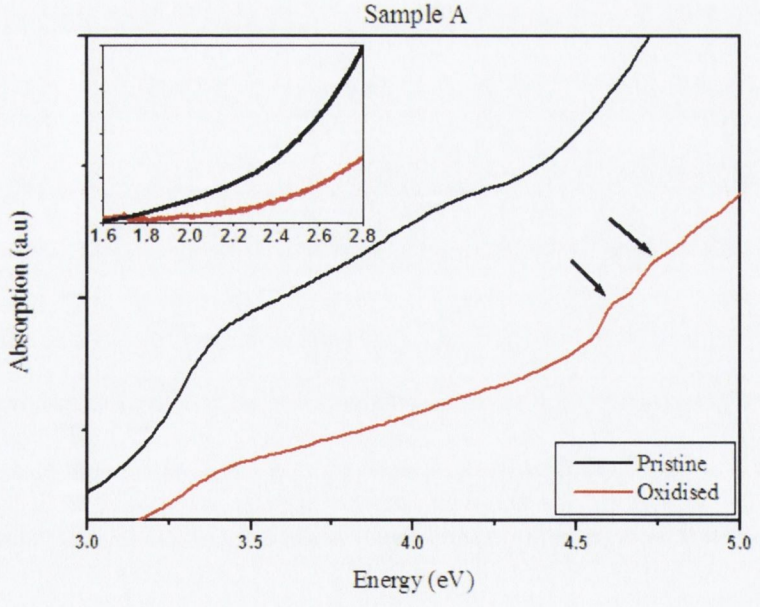

Figure 6.4: Absorption onsets of Sample A

indicates that the oxidised sample contains smaller nanocrystals than the pristine sample, which are capable of undergoing quantum confinement [3, 5].

6.6.2 Sample B

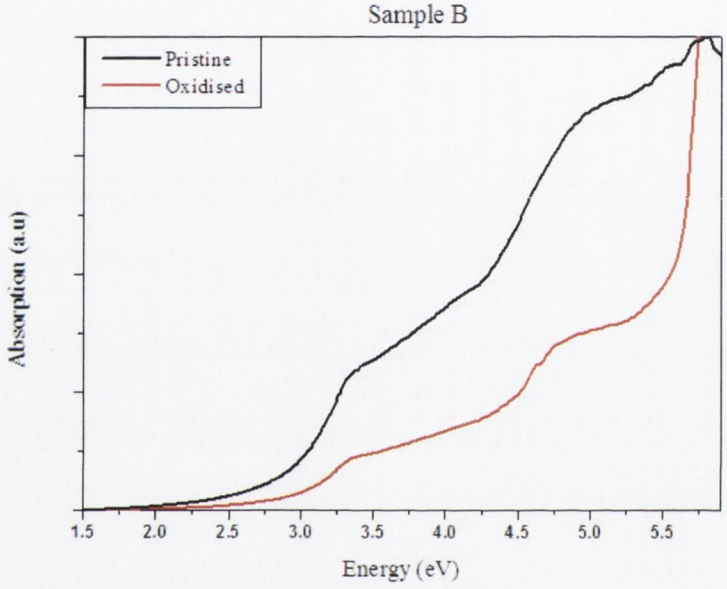

Figure 6.5: Absorption spectrum of Sample B

Figure 6.5 shows the absorption spectrum for Sample B. Figure 6.6 includes an inset illustrating the absorption onset of the sample, and shows a small shoulder that appeared in the oxidised sample's spectrum, which will be discussed later.

Both oxidised and pristine Sample B exhibited points of inflection near the direct band-gap energies of bulk crystalline silicon [7, 8]. The absorption onset ($\Gamma - X$) of Oxidised Sample B was blue-shifted by 0.2 eV from that of the pristine sample. This indicates that the oxidised sample contains smaller nanocrystals than the pristine sample, which are capable of undergoing quantum confinement [3, 5].

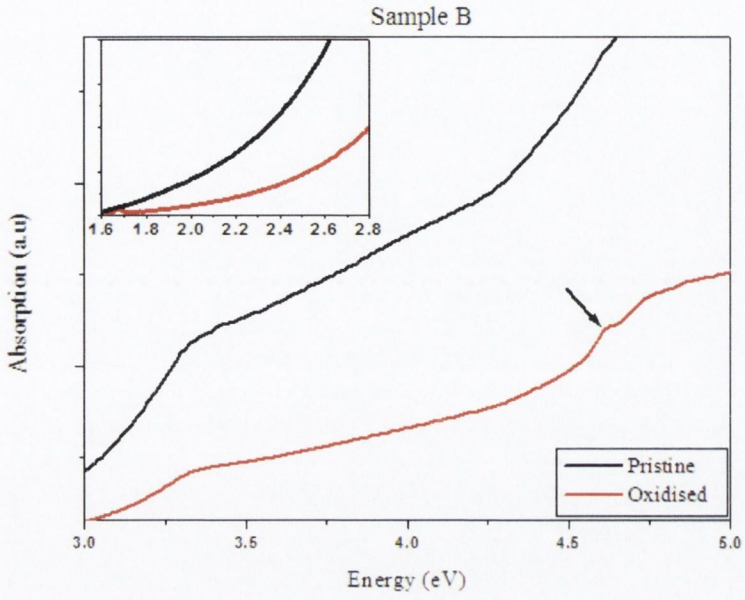

Figure 6.6: Absorption onsets of Sample B

6.6.3 Sample C

Figure 6.7 shows the absorption spectrum for Sample C. Both Pristine and Oxidised Sample C showed a similar absorption onset, with both samples exhibiting a strong absorption tail approaching 3 eV. Both samples displayed an absorption peak at 3.3 eV, which would correspond to a 0.1 eV red-shift of the $\Gamma_{25} - \Gamma_{15}$ transition, which is indicative of quantum confinement [3, 5, 6]. Another peak occurred for both samples at 3.8 eV. Both samples displayed very strong absorption past the $X_4 - X_1$ point, which occurs at 4.4 eV.

In summary, there was little observable difference between the absorption spectra for Pristine and Oxidised Sample C. There was some evidence of quantum confinement occurring in both samples due to the red-shift of the $\Gamma_{25} - \Gamma_{15}$ transition [3, 5, 6].

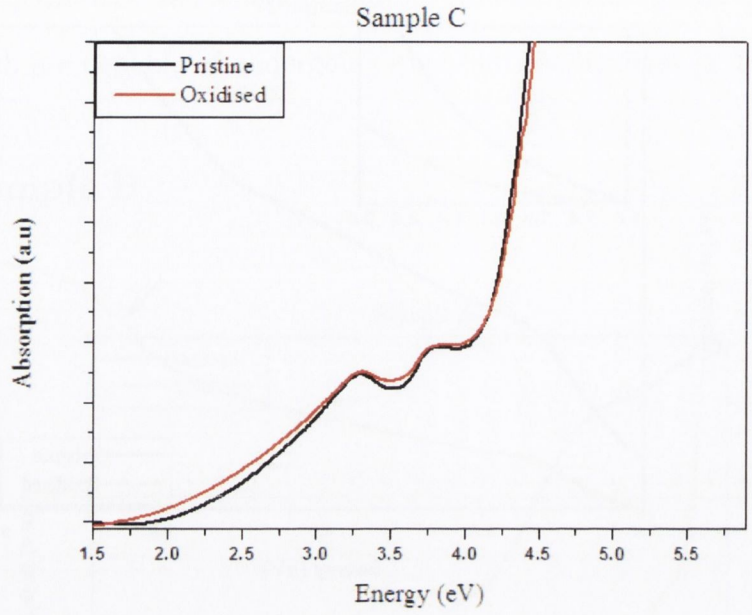

Figure 6.7: Absorption spectrum of Sample C

6.6.4 Sample D

Figure 6.8 shows the absorption spectrum for Sample D. Both Pristine and Oxidised Sample D showed a similar absorption onset. Both samples displayed an absorption peak at 3.3 eV, which would correspond to a 0.1 eV red-shift of the $\Gamma_{25} - \Gamma_{15}$ transition, which is indicative of quantum confinement [3, 5, 6].

Pristine Sample D exhibited a decrease in absorption between the $\Gamma_{25} - \Gamma_{15}$ and $X_4 - X_1$ points, but showed increased absorption in the region of the $L_3' - L_3$ (5.55 eV) transition [7].

Oxidised Sample D exhibited strong absorption around 4.8 eV, and also displayed additional absorption features in the region.

Therefore, both Pristine and Oxidised Sample D displayed red-shift of the $\Gamma_{25} - \Gamma_{15}$ transition, which is indicative of quantum confinement [3, 5, 6]. Oxidised

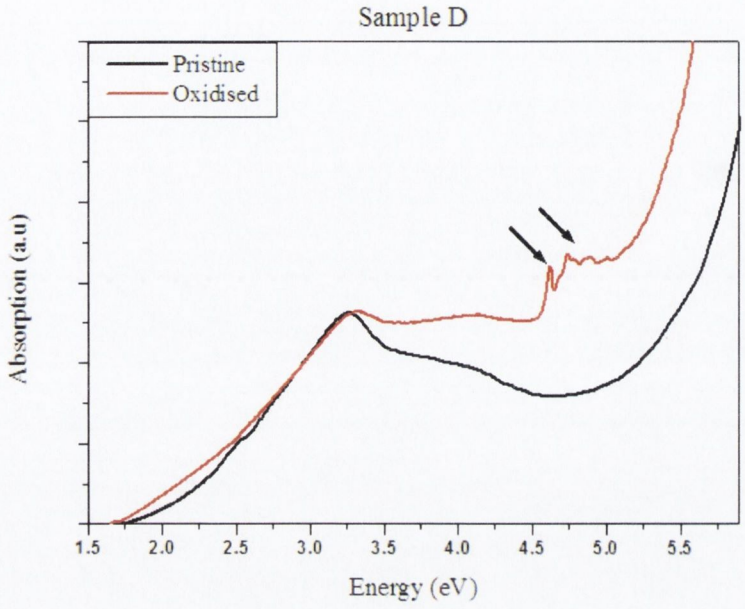

Figure 6.8: Absorption spectrum of Sample D

Sample D displayed interesting absorption features near the $X_4 - X_1$ (4.4 eV) point, which warrant further investigation (see Section 6.7 and *Chapter 8: Linear Optical Characterisation - A Discussion*).

6.6.5 Sample E

Figure 6.9 shows the absorption spectrum for Sample E. Both Pristine and Oxidised Sample E showed a similar absorption onset. Both samples displayed an absorption peak at 3.4 eV, which corresponds to absorption at the $\Gamma_{25} - \Gamma_{15}$ point.

Pristine Sample E exhibited shoulders in absorption at 4.6 and 4.8 eV. It absorbed strongly at higher energies, approaching the $L_3^{'} - L_3$ (5.55 eV) point.

Oxidised Sample E exhibited numerous peaks in the region of 4.7 eV, which shall be discussed later. It also absorbed strongly in the region of the $L_3^{'} - L_3$ (5.55 eV)

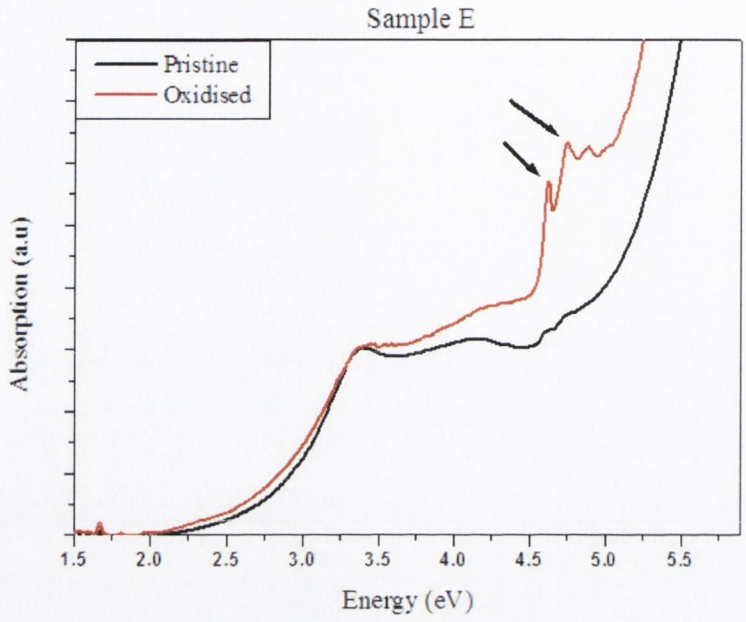

Figure 6.9: Absorption spectrum of Sample E

transition.

6.7 Summary

Absorption spectroscopy was carried out on all five samples, in the pristine and oxidised states. The spectra reflected the band-structure of silicon, with shoulders in absorption occurring at the direct transition energies of bulk silicon. Evidence of quantum confinement effects were exhibited by the samples in varying degrees. This evidence came in the form of a blue-shift of the $\Gamma - X$ onset energy and a red-shift of the $\Gamma_{25} - \Gamma_{15}$ transition energy.

As previously stated, the diameters of the crystalline nanowires and nanospheres are too large to experience quantum confinement. However, quantum confinement

may occur in the samples at isolated crystalline grain regions that exist inside the crystalline core, which are smaller than the Bohr exciton radius and can lead to quantum confined emission [9, 10]. Quantum confined emission can also occur due to lattice disruption from defects such as stacking faults and grain boundaries. Grain boundaries were imaged during the HRTEM study, see Figures 4.14 and 4.15 in *Chapter 4*. Increasing the oxidation time can lead to an increase in quantum confined effects, as the encroaching oxide forms isolated crystalline grains smaller than the Bohr exciton radius of silicon, and disruption to the lattice increases the number of defects [9, 10]. This mechanism is discussed in detail in *Chapter 2*. Although it was impossible to carry out a full HRTEM investigation in this study, a limited Raman study (*Chapter 4*) and an extensive photoluminescence study (*Chapter 7*) reveal the presence of quantum confined effects.

Some of the samples displayed additional peaks in the blue-shifted $X_4 - X_1$ region. These additional peaks were present in Pristine Sample E, and Oxidised Samples A, B, D and E. It is possible that these additional features may be indicative of oxidation effects. In *Chapter 8: Linear Optical Characterisation - A Discussion*, the absorption results reported here are compared with the Photoluminescence results from *Chapter 7: Linear Optical Characterisation II - Fluorescence Spectroscopy*. The comparison indicates that the enhanced absorption features found in the $X_4 - X_1$ region are indeed indicative of absorption by oxide, rather than quantum confined effects.

Bibliography

[1] ThermoSpectronic. *Basic UV-Vis Theory, Concepts and Applications,* `http://sbio.uct.ac.za/Sbio/documentation/ spectrophotometer.pdf`, *accessed January 2007* .

[2] *Figure: Spectrometer* `http://bouman.chem.georgetown.edu/S00/handout/spectrometer.gif`, *accessed January 2007* .

[3] Wilcoxon, J., Samara, G., and Provencio, P. *Physical Review B (Condensed Matter)* **60**(4), 2704–14 (1999).

[4] Fox, M. *Optical Properties of Solids, Figure 3.11, p. 66.* Oxford University Press, (2001).

[5] Holmes, J., Ziegler, K., Doty, R., Pell, L., Johnston, K., and Korgel, B. *Journal of the American Chemical Society* **123**(16), 3743–3748 (2001).

[6] Rama Krishna, M. and Friesner, R. *Journal of Chemical Physics* **96**(2), 873–7 (1992).

[7] Singleton, J. *Band Theory and Electronic Properties of Solids, p. 50.* Oxford University Press.

[8] Fox, M. *Optical Properties of Solids, p. 66,67.* Oxford University Press, (2001).

[9] Bai, Z., Yu, D., Wang, J., and Zou, Y. *Materials Science & Engineering B (Solid-State Materials for Advanced Technology)* **72**, 117–120 (2000).

[10] Yu, D., Bai, Z., Wang, J., Zou, Y., Qian, W., Fu, J., Zhang, H., Ding, Y., Xiong, G., Feng, S., You, L., and Xu, J. *Physical Review B (Condensed Matter)* **59**(4), 2498–501 (1999).

Chapter 7

Linear Optical Characterisation II — Fluorescence Spectroscopy

7.1 General Introduction to Excitation and Relaxation Mechanisms

Fluorescence is the absorption of a photon, followed by a re-emission of a lower energy photon. The difference in energy is used for an internal conversion, usually in the form of a molecular vibration (heat). The difference in position between the maxima of the absorbed energy and the re-emitted energy for the same electronic transition is called the Stokes shift. Energy levels are classified in terms of electronic spin. S refers to singlet states and T refers to triplet states. Most materials at room temperature exist in the ground state, termed S_0. Consider the situation where a photon is absorbed and excites an electron to a higher state: If the photon re-emission occurs between two states with the same spin, e.g. S_1 to S_0, then the emission is termed fluorescence.

If the photon re-emission occurs between two states with different spin, e.g. T_1 to S_0, then the emission is termed phosphorescence. Fluorescence has a much shorter lifetime (1×10^{-5}s to 1×10^{-9}s) than phosphorescence (1×10^{-4}s to hours), and is much more statistically probable [1]. The low probability of intersystem crossing arises due to the fact that the molecules must first undergo spin conversion to produce unpaired electrons, which is an unfavourable process. A Jablonski diagram depicts the relaxation mechanisms for excited state molecules, and is shown in Figure 7.1 [2].

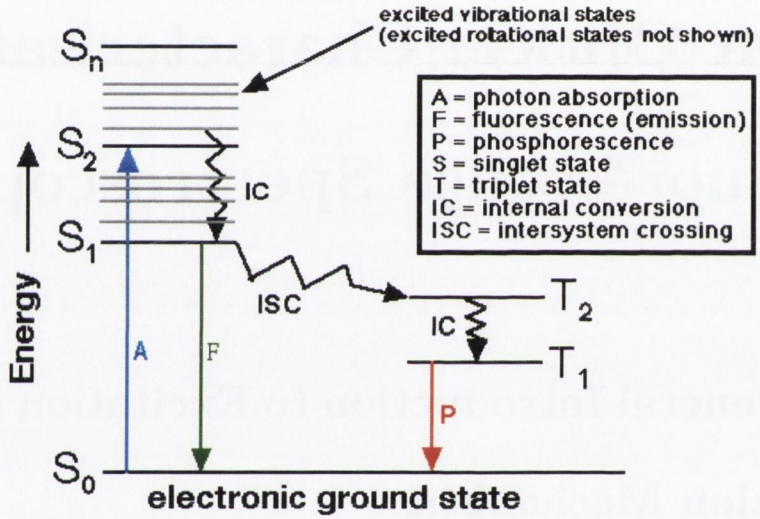

Figure 7.1: Jablonski diagram

Non-radiative processes can also occur. After a photon is absorbed, the excited molecule will quickly relax to the lowest vibrational energy level of the excited state. Because of this rapid internal conversion, all subsequent relaxation processes occur from the lowest vibrational level of the excited state. The primary cause of the Stokes shift is this rapid internal conversion in the S_1 excited state [3]. Internal conversion is the radiation-less transition between energy states of the same spin. Intersystem crossing is the radiation-less transition between different spin states. Vibrational

relaxation is the most common of the three, and occurs on the pico-second scale. It can occur in the form of vibrations or rotations, and is enhanced by physical contact with other molecules. Thus, vibrational relaxation is enhanced in the presence of a solvent. When the material in question is in a gaseous phase, vibrational relaxation can be increased due to collisions with other gas molecules [1]. When a sample is in solution, the emission spectrum tends to appear as a broad band as the detailed vibrational structure is lost [3].

7.2 The Fluorimeter

A fluorimeter is a device that records the fluorescence from a material. It operates by splitting a light source into its constituent wavelengths, and then selectively exciting the material under study. Fluorescence from the material is in turn broken into its constituent wavelengths, which then travel to the detector, see Figure 7.2. Generally, when studying a fluorescent material, an excitation wavelength is first chosen. The emission from the material is then recorded over a range of wavelengths. Usually the excitation wavelength is chosen with respect to the UV-Vis absorption spectrum. The material is first excited at the wavelength of maximum absorption. The process is repeated using different excitation wavelengths until the fluorescence is maximised. This process can be quite haphazard, due to the Stokes effect.

7.3 Fluorescence in Nanostructured Silicon

As discussed in Chapter 2, bulk silicon is an indirect band-gap material, and is therefore an inefficient light emitter. However, nanostructured silicon can photo-luminesce

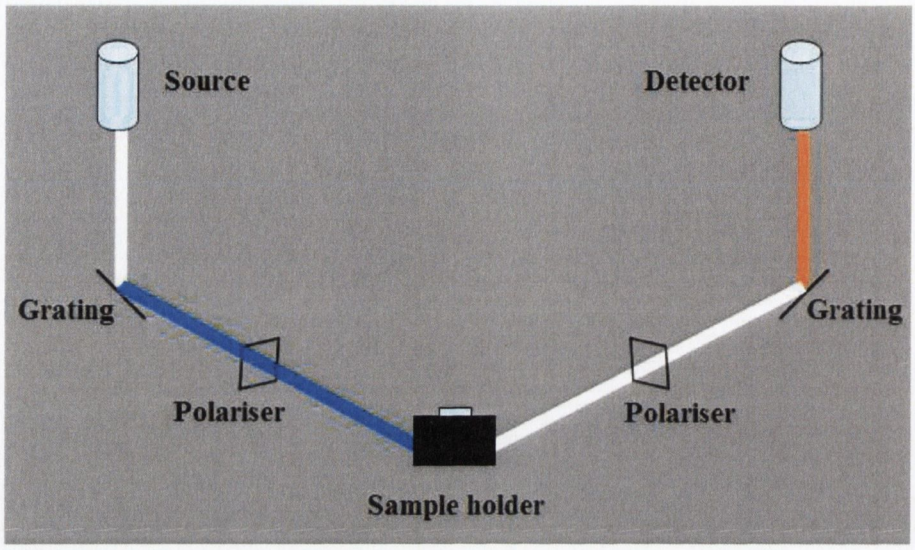

Figure 7.2: Fluorimeter

(PL) through a variety of different mechanisms. This section will concentrate on PL mechanisms in oxide coated silicon nanostructures. These structures are relevant to the samples under study in this report.

PL in the red region (700 – 900 nm) and at the in the direct electron-hole recombination energies in the ultra-violet region (280 – 400 nm) occurs due to quantum confinement [4, 5, 6, 7].

Emission in the blue-green region arises from radiative decay of self-trapped excitons. These can occur at defect centres located at the SiO_x/Si interface or in the amorphous silicon oxide layer [8, 5]. PL at wavelengths as low as 420 nm have been attributed to this mechanism [5].

7.4 Results

Three dimensional photoluminescence (3DPL) spectroscopy was carried out on each pristine and oxidised sample. The results were then compared to identify any changes in the PL spectra that occurred upon oxidation. The 3DPL analysis gave information on the emission bands of each sample, and also on what excitation energies each sample photoluminesced for.

2D PL analysis was also carried out. The PL spectrum of each pristine and oxidised sample was recorded for excitation at 200 nm. The 2D PL spectra provided detailed information on PL peak positions, which are not as easily identifiable from the 3DPL spectra. All PL measurements were recorded using a Perkin Elmer LS-55 fluorimeter.

7.4.1 Sample A

Figures 7.3 and 7.4 show the 3D PL spectra for Pristine Sample A. Emission occurred for excitation wavelengths between 200 nm and 345 nm (6.20 – 3.59 eV). Pristine Sample A's most intense emission peak occurred at 384 nm, for an excitation wavelength of 323 nm. The ridge-like structure that occurred across the 3D PL graph is evidence of an inhomogeneous size distribution of nanocrystals.

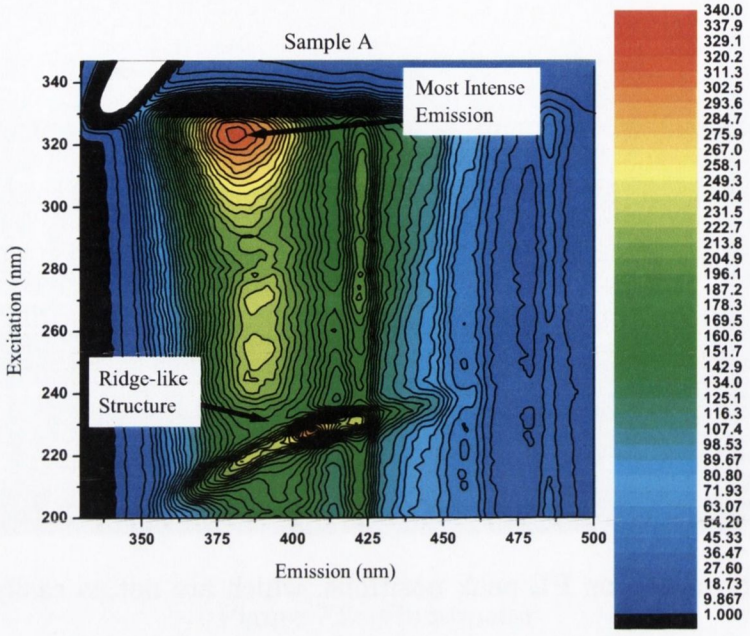

Figure 7.3: 3D PL graph, Pristine Sample A (i)

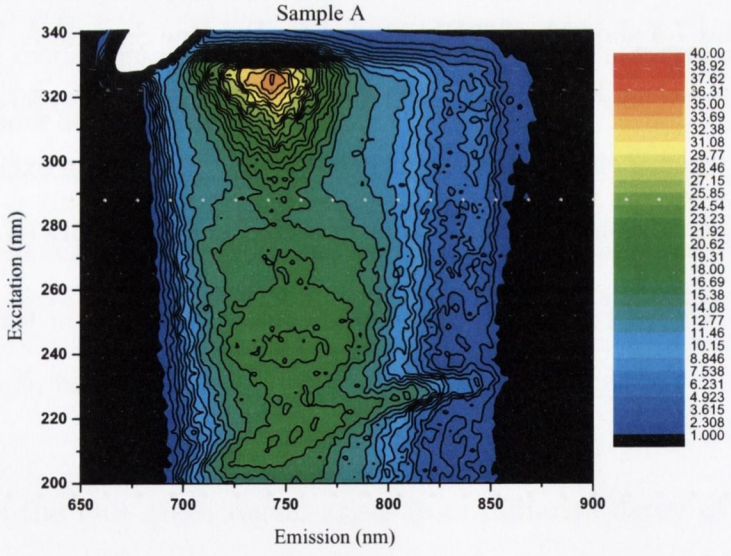

Figure 7.4: 3D PL graph, Pristine Sample A (ii)

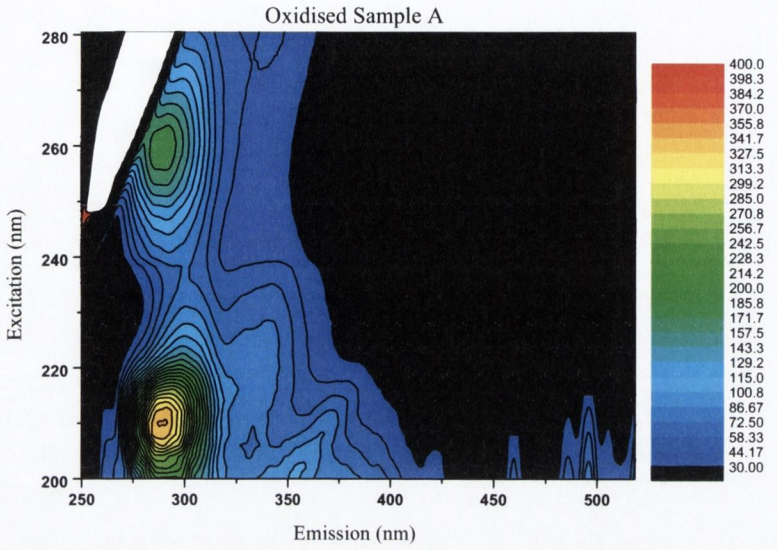

Figure 7.5: 3D PL graph, Oxidised Sample A (i)

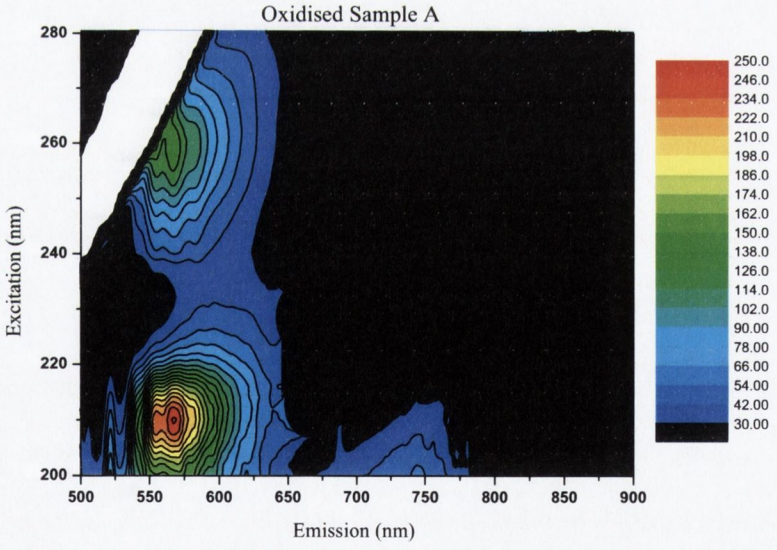

Figure 7.6: 3D PL graph, Oxidised Sample A (ii)

Figures 7.5 and 7.6 show the 3D PL spectra for Oxidised Sample A. Emission

occurred for excitation wavelengths between 200 nm and 290 nm (6.20 – 4.38 eV). Strong, broad emission occurred in the ultra-violet region.

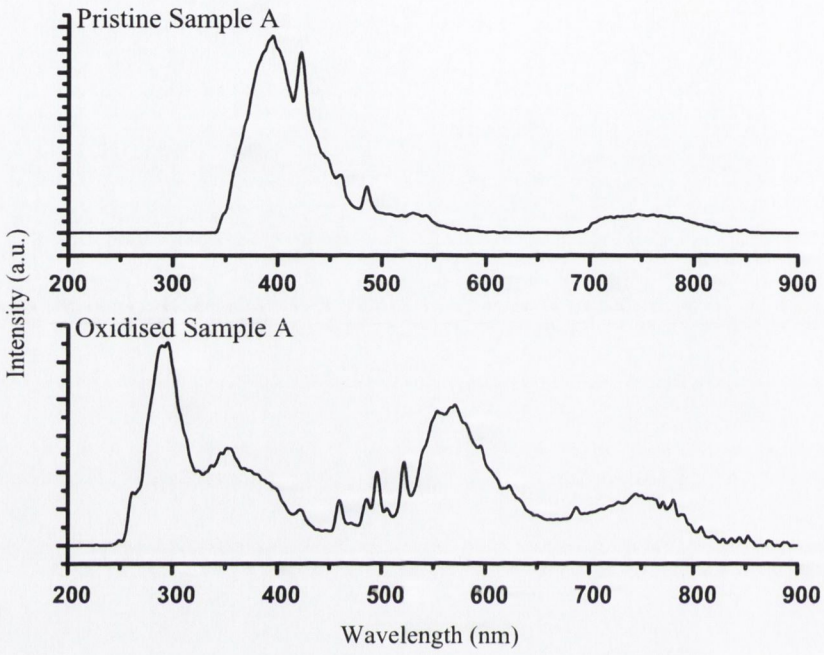

Figure 7.7: 2D PL graph for excitation at 200 nm, Sample A

Figure 7.7 compares the PL of Pristine and Oxidised Sample A for excitation at 200 nm. PL occured in the red region (700 – 800 nm) for both samples, with Oxidised Sample A producing more intense PL. PL in this region is due to quantum confinement [4, 5, 6]. Oxidised Sample A produced intense luminescence in the ultra-violet region at energies corresponding to the direct recombination energies of bulk silicon. This emission is due to quantum confinement [7] and will be examined further in *Chapter 8: Linear Optical Characterisation - A Discussion.*

Oxidised Sample A also produced strong emission in the 500 – 600 nm region.

This emission is due to radiative decay of self-trapped excitons [8, 5].

Strong broad emission occurred for Pristine Sample A in the ultra- violet to violet region (350 – 500 nm), with a sizable component occurring in the visible region (above 400 nm). It is likely that the PL arises from direct recombination of carriers at the interface between the crystalline silicon nanoclusters and the oxide shell. This mechanism will be explored further in *Chapter 8: Linear Optical Characterisation - A Discussion.*

7.4.2 Sample B

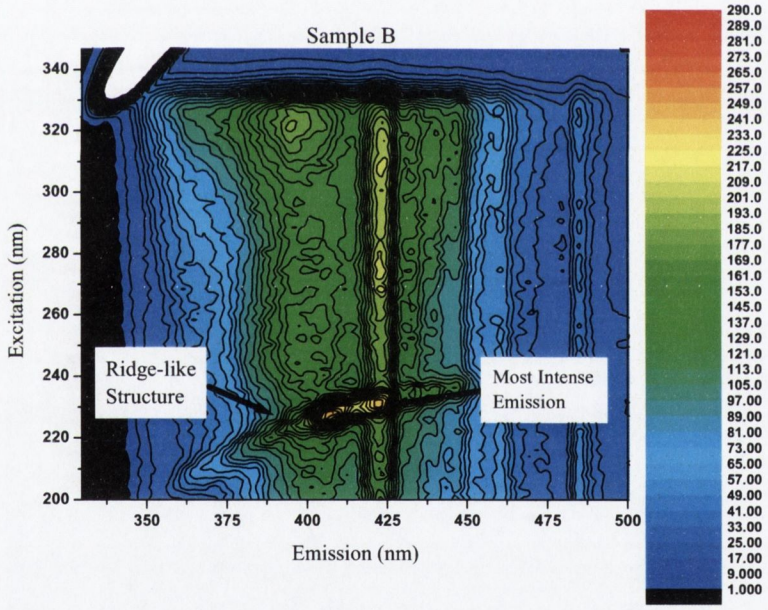

Figure 7.8: 3D PL graph, Pristine Sample B (i)

Figures 7.8 and 7.9 show the 3D PL spectra for Pristine Sample B. Emission occurred for excitation wavelengths between 200 nm and 345 nm (6.20 – 3.59 eV). Pristine Sample B exhibited a strong emission peak at 400 nm when excited at 323

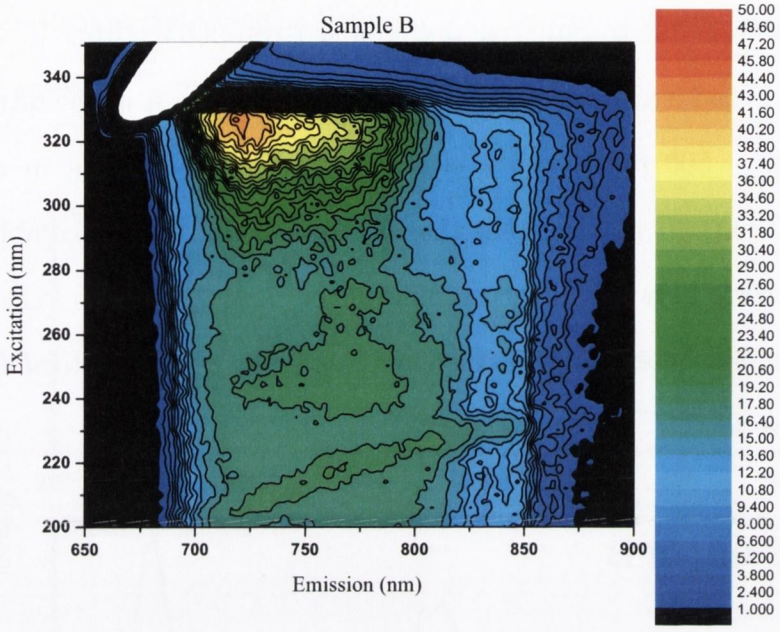

Figure 7.9: 3D PL graph, Pristine Sample B (ii)

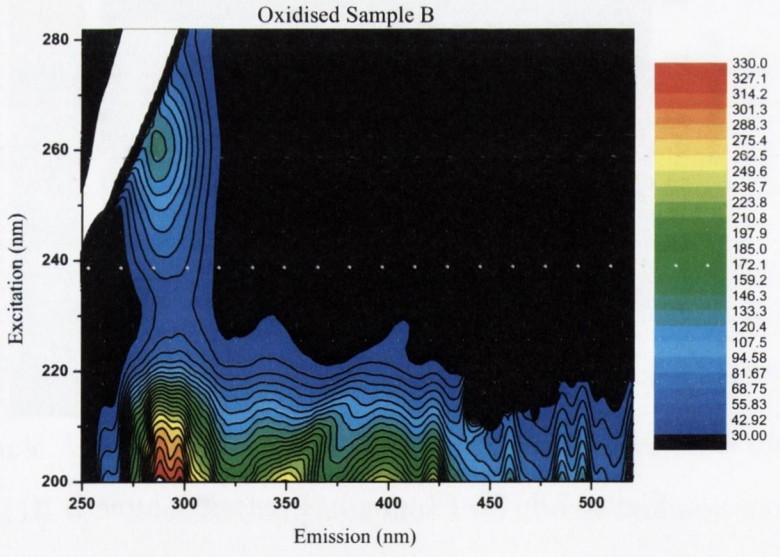

Figure 7.10: 3D PL graph, Oxidised Sample B (i)

nm, but its most intense peak in emission occurred at 423 nm, for a corresponding excitation wavelength of 231 nm. A ridge-like structure occurred across the 3D PL graph, and is evidence of an inhomogeneous size distribution of nanostructures.

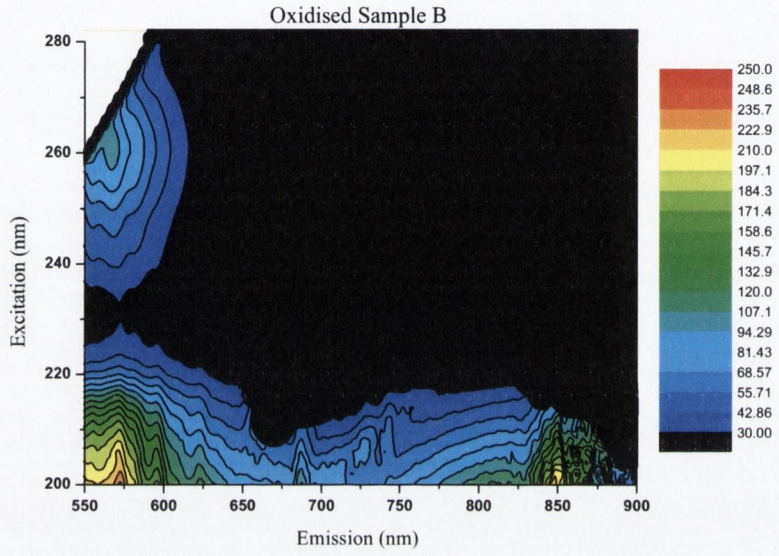

Figure 7.11: 3D PL graph, Oxidised Sample B (ii)

Figures 7.10 and 7.11 show the 3D PL spectra for Oxidised Sample B. Emission occurred for excitation wavelengths between 200 nm and 290 nm (6.20 – 4.38 eV). Strong, broad emission occurred in the ultra-violet region.

Figure 7.12 compares the PL of Pristine and Oxidised Sample B for excitation at 200 nm. PL occurred in the red region (700 – 800 nm) for both samples, with Oxidised Sample B producing more intense red PL. PL in this region is due to quantum confinement [4, 5, 6]. Oxidised Sample B produced intense luminescence in the ultra-violet region at energies corresponding to the direct recombination energies of bulk silicon. This is indicative of quantum confinement [7] and will be examined further in *Chapter 8: Linear Optical Characterisation - A Discussion.*

Oxidised Sample B also produced strong emission in the 500 – 600 nm region. This emission is due to radiative decay of self-trapped excitons [8, 5].

Strong broad emission occured for Pristine Sample B in the ultra- violet to violet region (350 – 500 nm), with a sizable component occurring in the visible region (above 400 nm). It is likely that the PL arises from direct recombination of carriers at the interface between the crystalline silicon nanoclusters and the oxide shell. This mechanism will be explored further in *Chapter 8: Linear Optical Characterisation - A Discussion.*

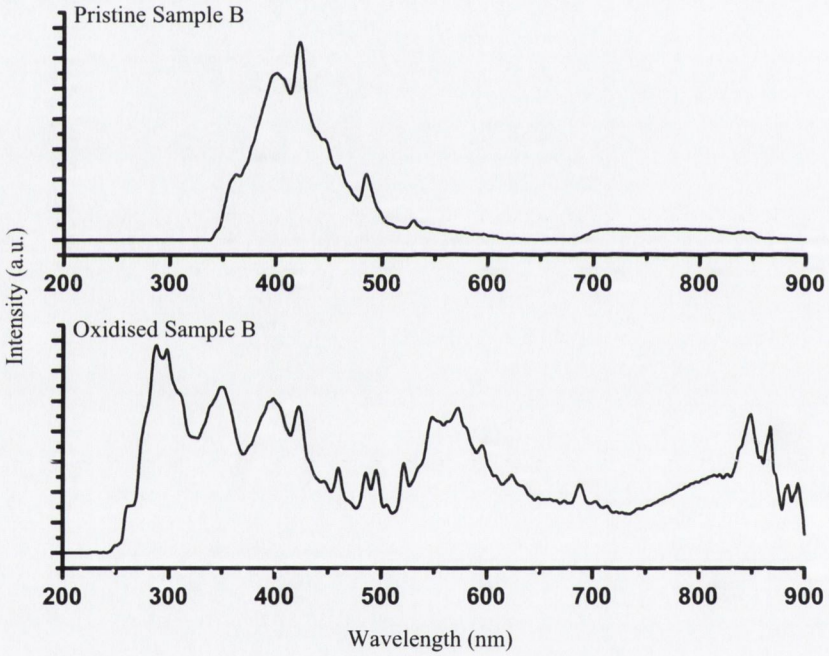

Figure 7.12: 2D PL graph for excitation at 200 nm, Sample B

7.4.3 Sample C

Figures 7.13 and 7.14 show the 3D PL spectra for Pristine Sample C. Emission occurred for excitation wavelengths between 200 nm and 320 nm (6.20 – 3.88 eV). Pristine Sample C exhibited a strong emission peak at 420 nm when excited at 200 nm, but its most intense peak in emission occurred in the red region. Emission in the red region is due to quantum confinement [4, 5, 6].

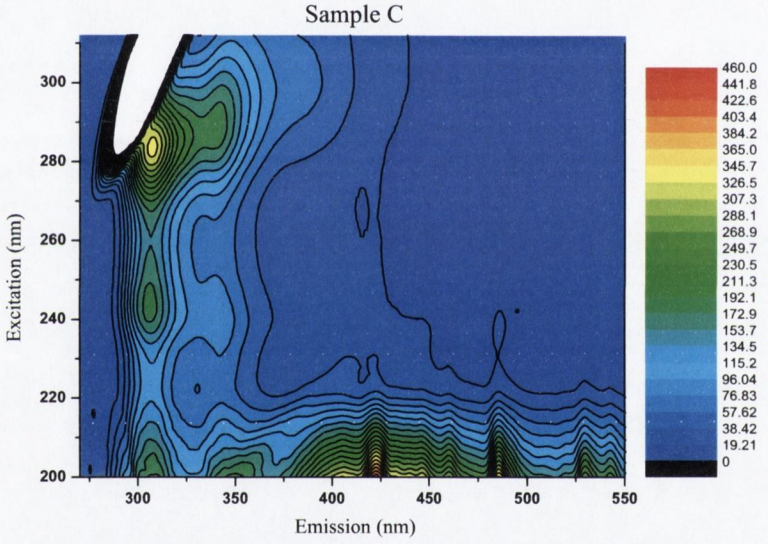

Figure 7.13: 3D PL graph, Pristine Sample C (i)

Figure 7.15 shows the 3D PL spectrum for Oxidised Sample C. Strong emission occurred for excitation wavelengths between 200 nm and 220 nm (6.20 – 5.64 eV). The most intense emission occurred in the violet region.

Figure 7.16 compares the PL of Pristine and Oxidised Sample C for excitation at 200 nm. Pristine Sample C exhibited strong PL in the red region, whereas Oxidised Sample C did not photoluminesce in this region. PL in the red region is due to quantum confinement [4, 5, 6].

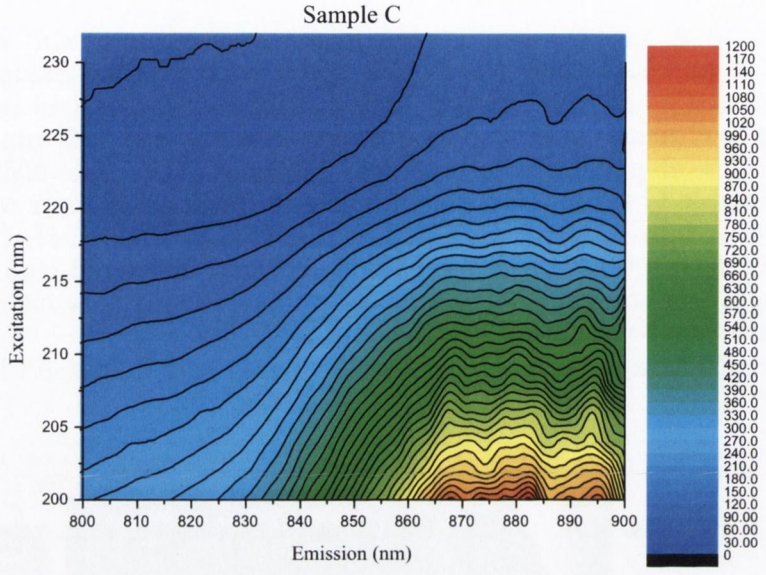

Figure 7.14: 3D PL graph, Pristine Sample C (ii)

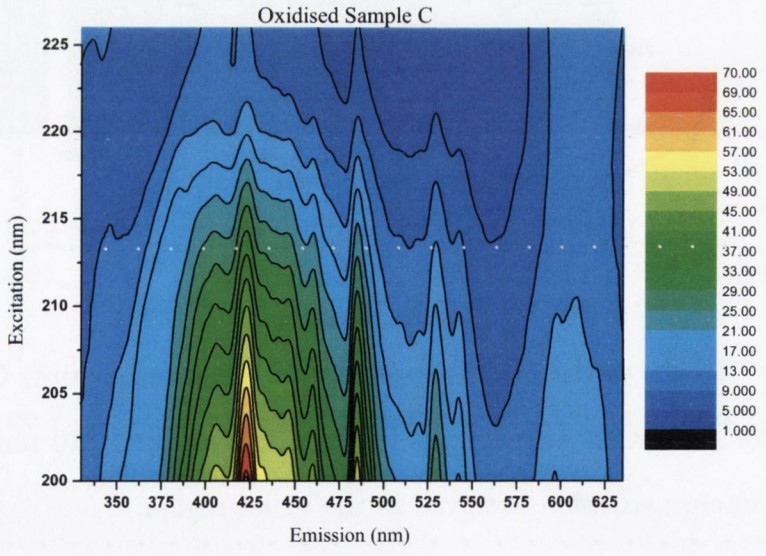

Figure 7.15: 3D PL graph, Oxidised Sample C

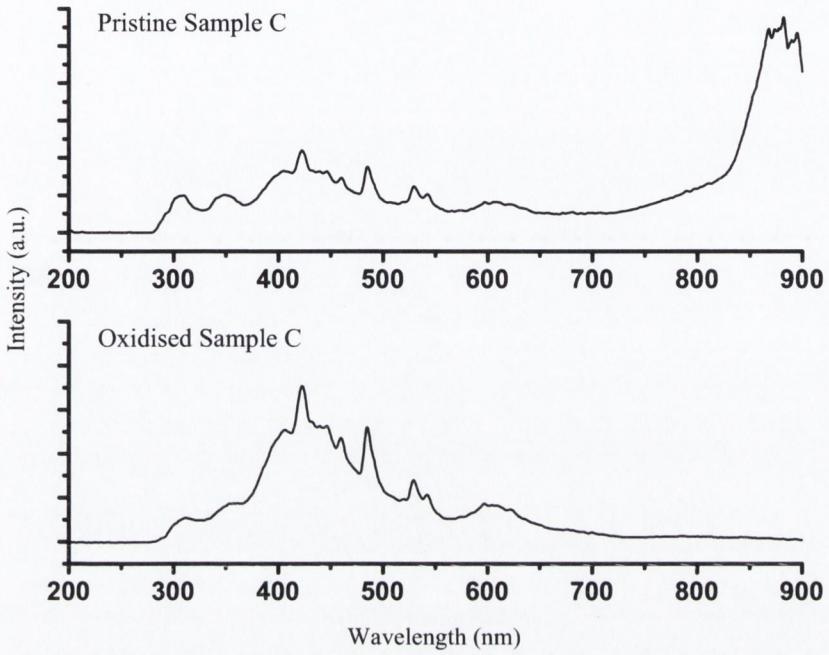

Figure 7.16: 2D PL graph for excitation at 200 nm, Sample C

Both samples displayed photoluminescence in the ultra violet – green regions. PL in the blue – green region is due to radiative decay of self-trapped excitons [8, 5]. Emission in the ultra violet – violet region is due to quantum confinement [7]. The pristine sample photoluminesced more strongly in this region than the oxidised sample did.

7.4.4 Sample D

Figure 7.17 shows the 3D PL spectrum for Pristine Sample D. Emission occurred for excitation wavelengths between 200 nm and 230 nm (6.20 – 5.39 eV). Pristine Sample D exhibited strong emission in the blue – green region, with the most intense emission peak occurring at 488 nm for excition at 200 nm. Emission in this region is due to

radiative decay of self-trapped excitons [8, 5].

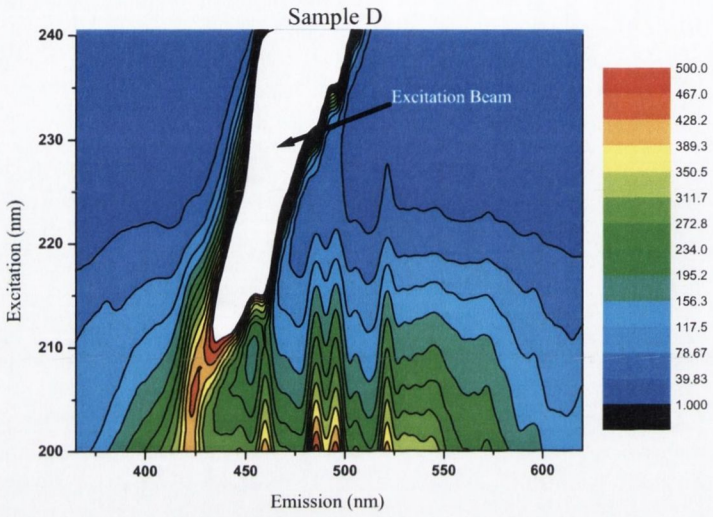

Figure 7.17: 3D PL graph, Pristine Sample D (i)

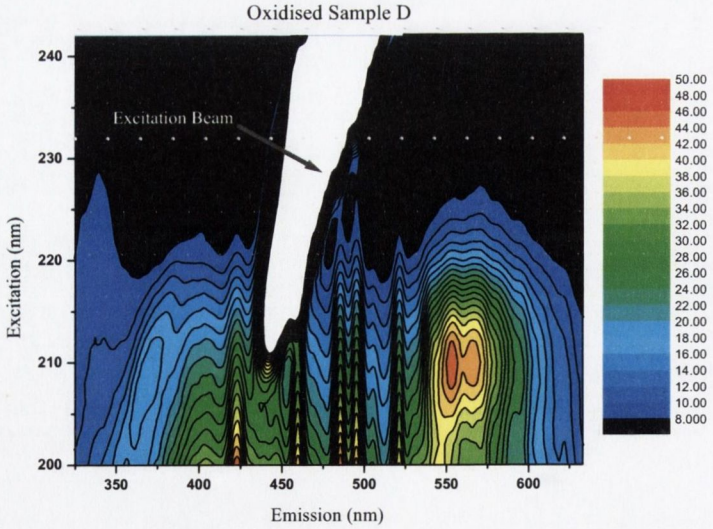

Figure 7.18: 3D PL graph, Oxidised Sample D

Figure 7.18 shows the 3D PL spectrum for Oxidised Sample D. Emission occurred for excitation wavelengths between 200 nm and 230 nm (6.20 – 5.39 eV). The emission is similar to that produced by Pristine Sample D, with the addition of strong emission occurring at 560 nm for excitation at 210 nm.

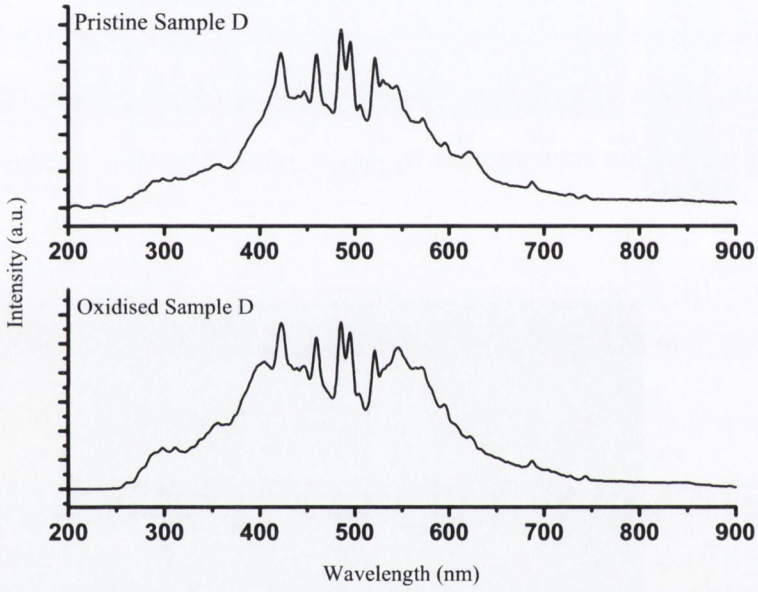

Figure 7.19: 2D PL graph for excitation at 200 nm, Sample D

Figure 7.19 compares the PL of Pristine and Oxidised Sample D for excitation at 200 nm. The pristine and oxidised samples produced similar emission spectra. The PL spectra for both samples is dominated by broad emission between 250 and 700 nm, with the most intense emission occurring around 500 nm. Hence the emission is dominated by the radiative decay of self-trapped excitons [8, 5].

7.4.5 Sample E

Figures 7.20 and 7.21 show the 3D PL spectra for Pristine Sample E. Emission occurred for excitation wavelengths between 200 nm and 230 nm (6.20 – 5.39 eV). Some weak emission was exhibited in the red region, between 700 and 800 nm, which is due to quantum confinement [4, 5, 6]. Pristine Sample E exhibited strong emission in the blue – green region. Emission in this region is due to the radiative decay of self-trapped excitons [8, 5]. It also emitted strongly in the ultra violet region, with Pristine Sample E's most intense emission occurring at 286 nm (4.34 eV) for excitation at 208 nm. This corresponds to direct recombination at the $X_4 - X_1$ (4.4 eV) point [7].

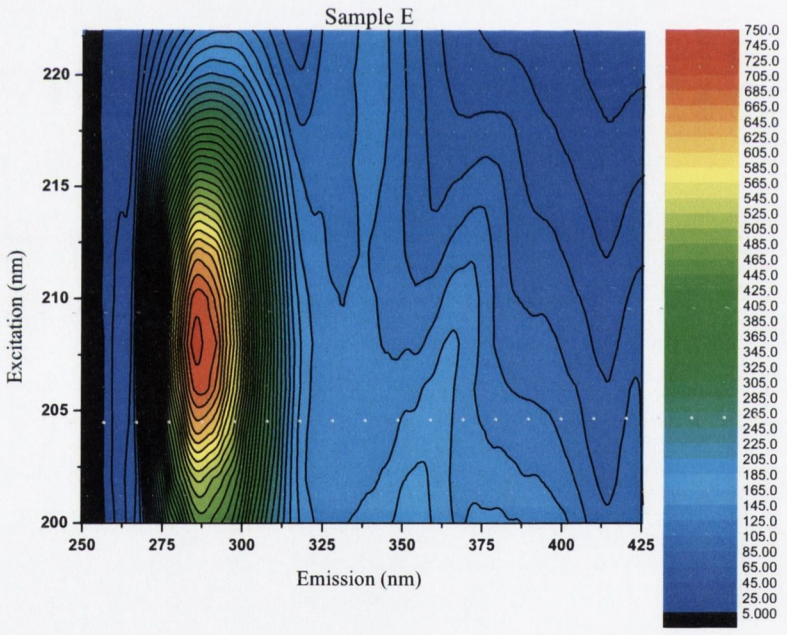

Figure 7.20: 3D PL graph, Pristine Sample E (i)

Figures 7.22 and 7.23 show the 3D PL spectra for Oxidised Sample E. Emission occurred for excitation wavelengths between 200 nm and 245 nm (6.20 – 5.06 eV).

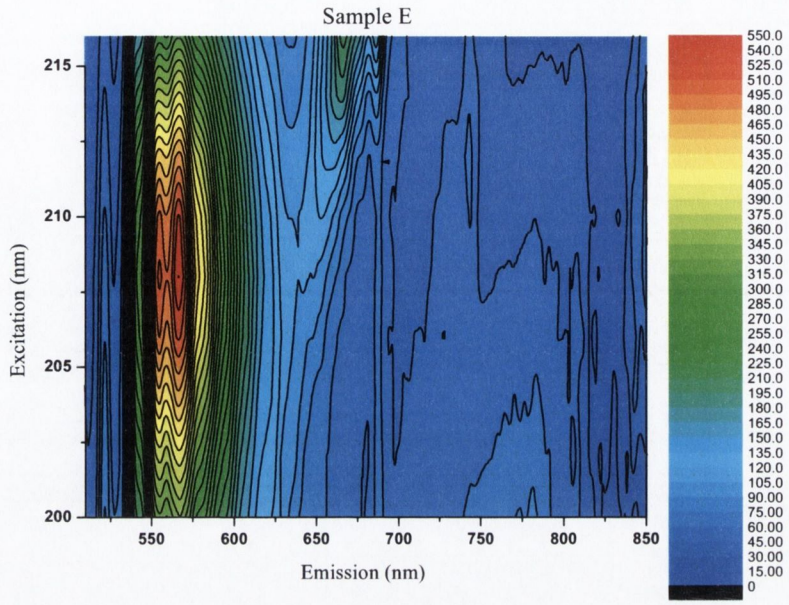

Figure 7.21: 3D PL graph, Pristine Sample E (ii)

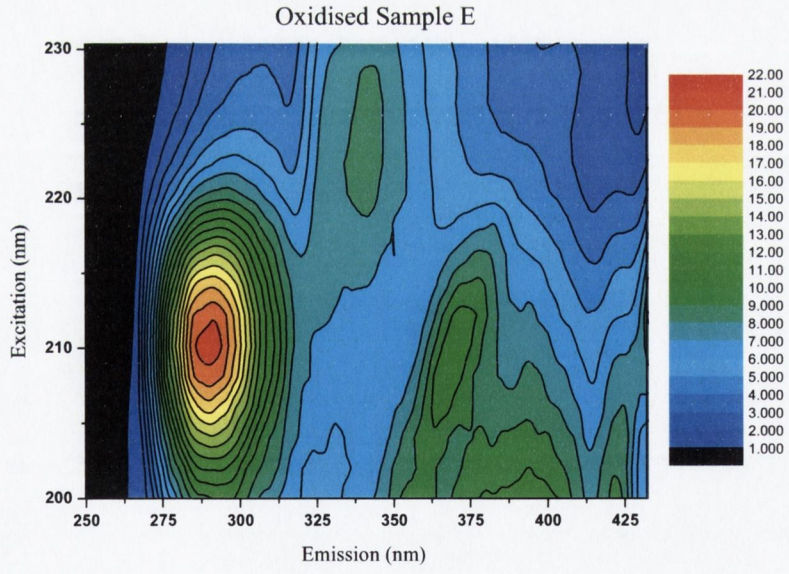

Figure 7.22: 3D PL graph, Oxidised Sample E (i)

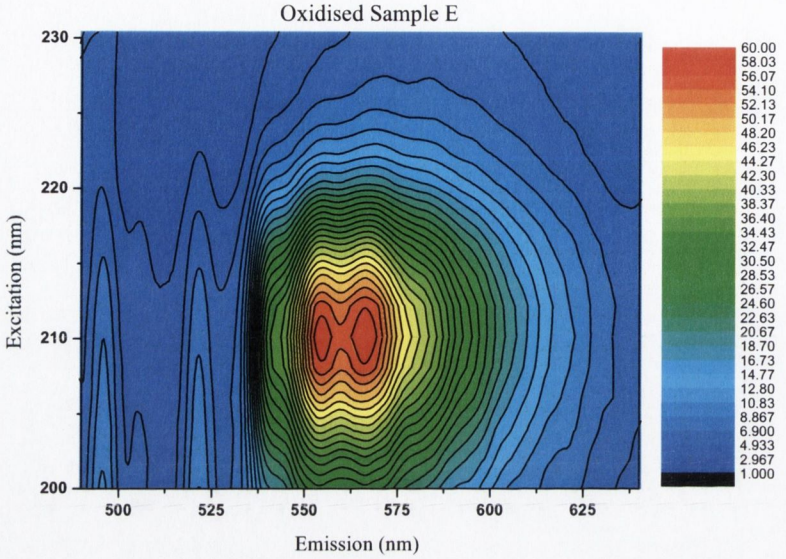

Figure 7.23: 3D PL graph, Oxidised Sample E (ii)

Oxidised Sample E exhibited its strongest emission in the blue – green region, at 555 and 565 nm, for excitation at 210 nm. Emission in this region is due to the radiative decay of self-trapped excitons [8, 5]. It also emitted in the ultra violet region, but with less intensity than in the blue – green region.

Figure 7.24 compares the PL of Pristine and Oxidised Sample E for excitation at 200 nm. Pristine Sample E emitted in the blue – green region, through the radiative decay of self-trapped excitons [8, 5]. It also showed evidence of PL due to quantum confinement effects. An emission band was evident between 700 and 800 nm, which is due to quantum confinement [4, 5, 6]. Also, the most intense emission for Pristine Sample E occurred at 286 nm (4.34 eV), which corresponds to direct recombination at the $X_4 - X_1$ (4.4 eV) point. This direct recombination is a consequence of quantum confinement [7].

Oxidised Sample E emitted most strongly in the blue – green region, and produced

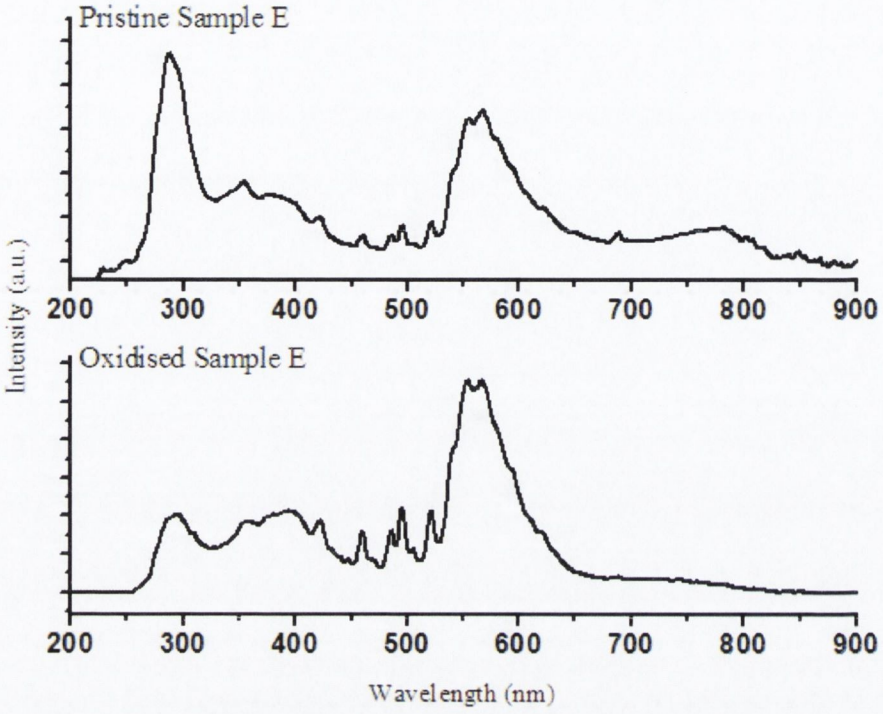

Figure 7.24: 2D PL graph for excitation at 200 nm, Sample E

emission that was dominated by the radiative decay of self-trapped excitons, rather than by quantum confinement. It showed negligible evidence of PL between 700 and 800 nm, and much weaker emission at 286 nm (4.34 eV), than Pristine Sample E.

7.5 Additional Technique: Lifetime measurements

Lifetime measurements were carried out on Pristine Sample A in order to elucidate the PL mechanisms that contributed to the strong, broad emission that occurred for Pristine Samples A and B (see Figures 7.3 and 7.8).

A solid piece of Pristine Sample A was dispersed in ultra-pure water by gentle agitation from a sonic tip. Lifetime analysis was carried out using a FluoTime 200 PicoQuant system, for excitation at 295 nm. This machine records fluorescence decay by means of time-correlated single photon counting. The instrument response function was less than 50 ps. The PL decay was recorded at 400 nm and 420 nm.

7.5.1 The FluoTime 200 PicoQuant Fluorimeter

The FluoTime 200 PicoQuant houses all of the optics and electronics needed for recording fluorescence decays by means of Time-Correlated Single Photon Counting (TCSPC). The set-up can be used with either a femtosecond or picosecond laser system. In this investigation, a pulsed laser diode of wavelength 295 nm was utilised. The system allows operation at more than 80 MHz repetition rate and count rates of up to several million counts per second.

The optical set-up achieves high sensitivity by using quartz collecting optics, along with vertical dispersion to maximise the overlap of the excitation beam and the detection volume within the sample. The monochromators are fitted with a stepper motor to enable Time-Resolved Emission Spectroscopy (TRES). TRES enables the fluorescence lifetime to be automatically recorded as a function of emission wavelength and facilitates detailed analysis of the decay. A complementary software analysis system for TRES (FluoPlot) is provided with the system.

A range of detectors are available, including standard photomultiplier tubes to extremely fast micro-channel plate photomultiplier tubes (MCP-PMT). MCP-PMT allow detection with an instrument response function of less than 50 ps. A MCP-PMT was used in this investigation. The data acquisition is done on a single PC-card, and is controlled by software which provides functions such as setup parameters and control of the measurement in the selected operation mode. Figure 7.25 [9] is a photograph of the FluoTime 200 PicoQuant device used in this study. Figure 7.26 [10] illustrates the basic set-up of a FluoTime PicoQuant system. The FluoTime 200 PicoQuant has additional features such as a choice of various detectors, and for spectral filtering, a choice of monochromators instead of cut-off filters [11].

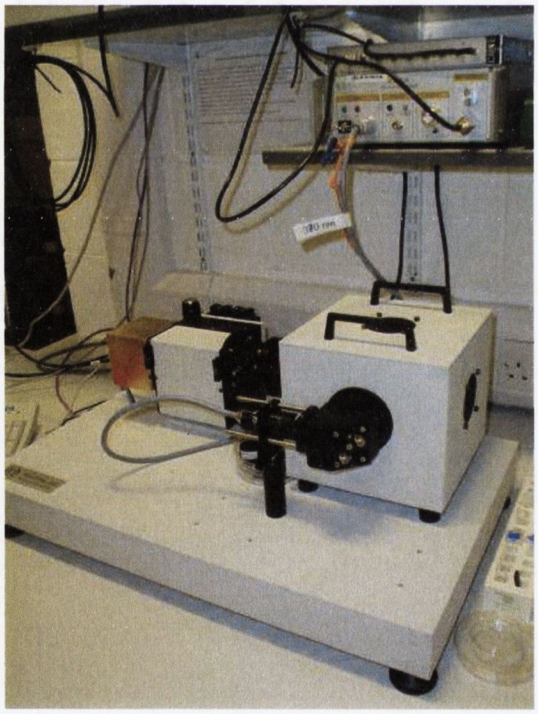

Figure 7.25: The FluoTime 200 PicoQuant system.

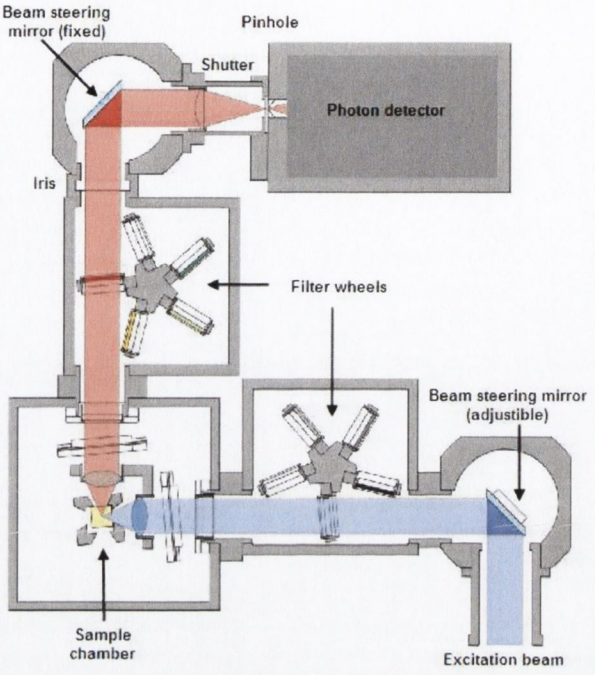

Figure 7.26: FluoTime PicoQuant components.

7.5.2 Results

Figures 7.27 and 7.28 show the fluorescence decay for emission at 400 nm and 420 nm respectively. The red lines correspond to the reference solvent, and the blue lines correspond to the sample dispersion. The initial peak intensity corresponds to excitation from the diode. The slower return to baseline intensity levels for the sample dispersion is due to photoluminescence.

The PL decay for emission at 400 nm and 420 nm were both best fit, in terms of χ^2, by a third order decaying exponential. This corresponds to three decay lifetimes. The residuals of these fits can also be seen in Figures 7.27 and 7.28. Ideally, residuals should show no pattern. Pattern in the residuals means that there is something that the model is not picking up. The residuals for the fits in Figures 7.27 and 7.28 are

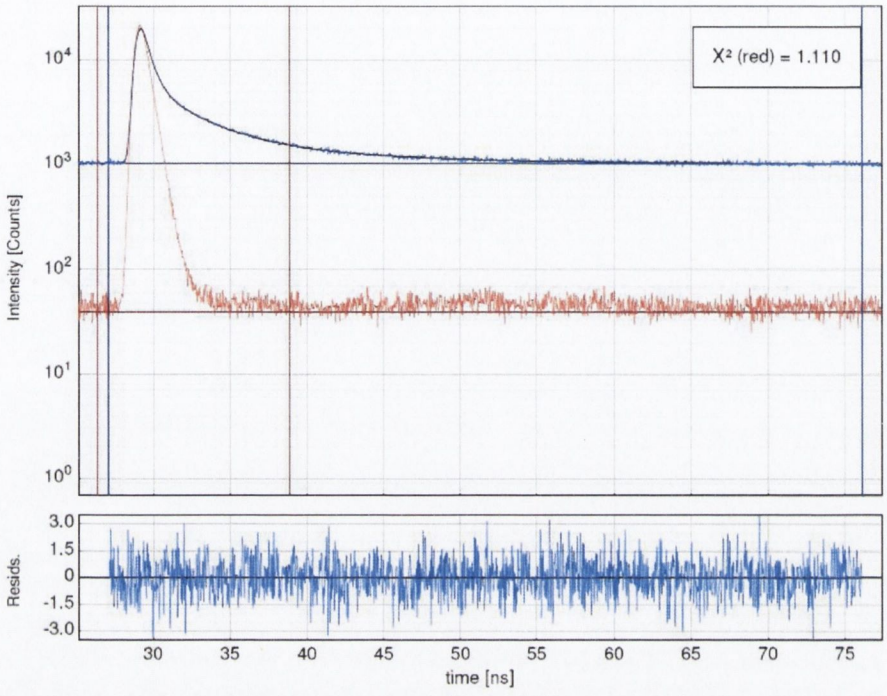

Figure 7.27: Plot of fluorescence decay for emission at 400 nm

good quality, and appear to show almost random variation around the mean. χ^2 for emission at 400 nm was 1.110, and for emission at 410 nm was 1.142. The good quality residuals and low values for χ^2 indicate that the third order decaying exponential was a good fit to the decays.

Figure 7.29 shows the fitted decay for emission at 400 nm, with Figure 7.30 showing the corresponding confidence intervals for the decay lifetimes. Figure 7.31 shows the fitted decay for emission at 420 nm, with Figure 7.32 showing the corresponding confidence intervals for the decay lifetimes.

The lifetimes were recorded at two different emission wavelengths, but corresponded well to each other (they are listed in Figures 7.29 and 7.31). The quickest, slowest, and middle decay lifetimes were averaged for the two emission wavelengths to

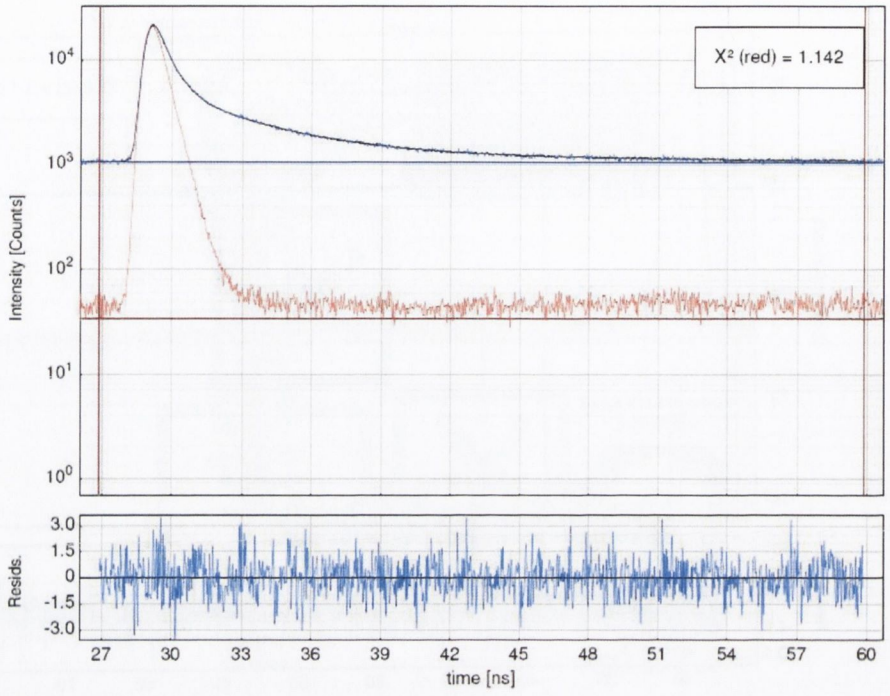

Figure 7.28: Plot of fluorescence decay for emission at 420 nm

give representative results. This gave average lifetimes of 0.466 ns, 2.903 ns and 7.950 ns. These short, nanosecond scale lifetimes are consistent with direct electron-hole recombination [12].

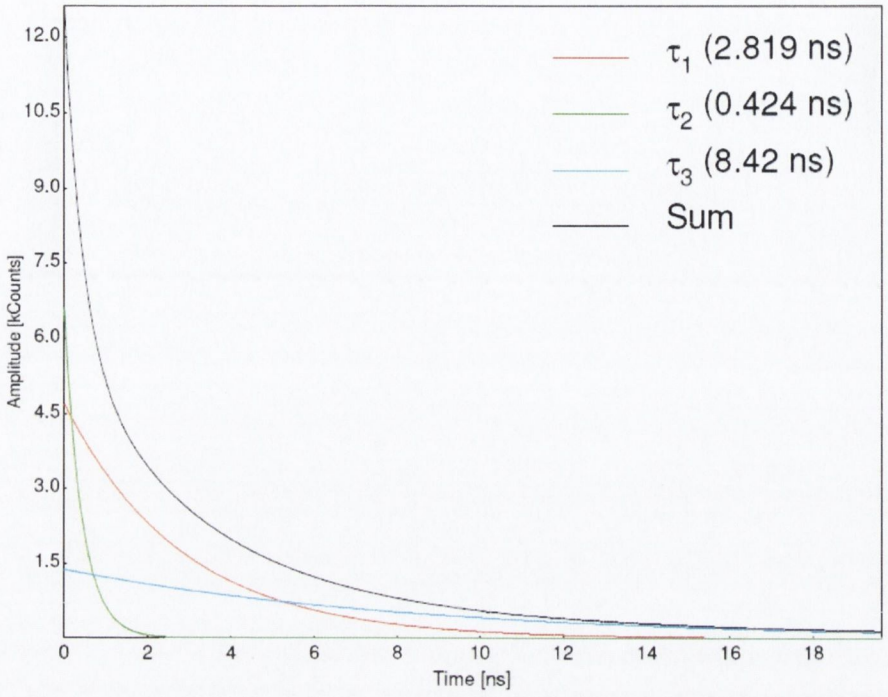

Figure 7.29: Fitted decay with exponential components for emission at 400 nm

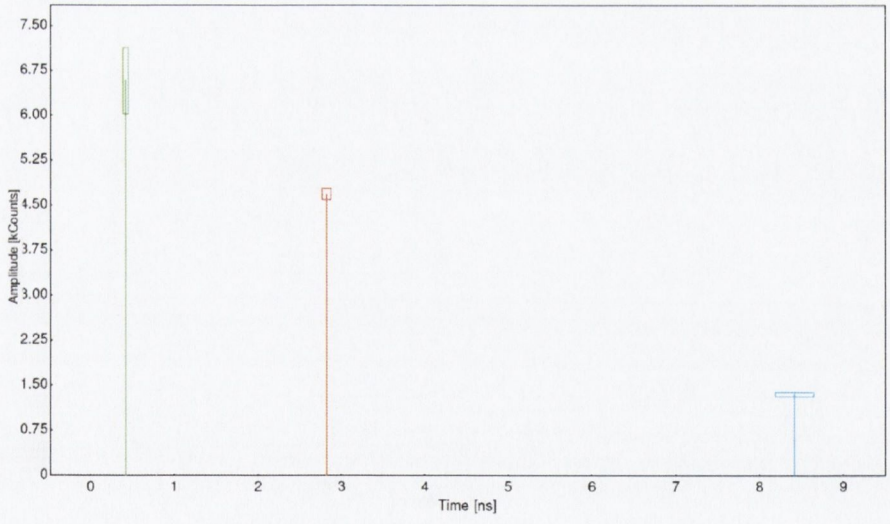

Figure 7.30: Confidence intervals of the decay lifetimes for emission at 400 nm

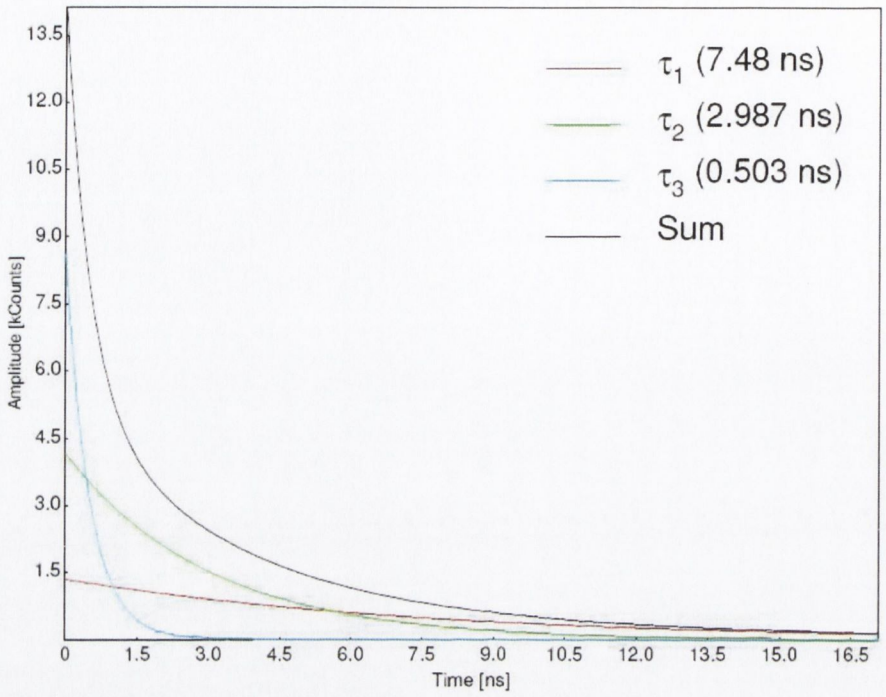

Figure 7.31: Fitted decay with exponential components for emission at 420 nm

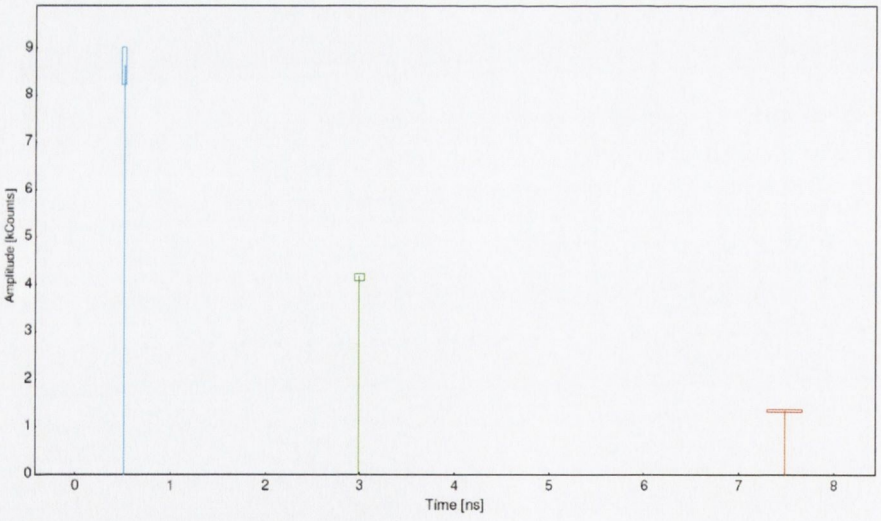

Figure 7.32: Confidence intervals of the decay lifetimes for emission at 420 nm

7.6 Summary

A photoluminescence study of the samples in pristine and oxidised states was carried out. This photoluminescence was due to quantum confinement and the radiative decay of self-trapped excitons. A more detailed analysis of the results is presented in *Chapter 8: Linear Optical Characterisation - A Discussion*, where absorption and morphology data are included in the analysis to ascertain morphology specific PL mechanisms.

Lifetime measurements were performed on Pristine Sample A to establish the nature of an interesting band of luminescence that occurred for Pristine Samples A and B in the violet region. The results indicated that the strong, broad emission that occurred for Pristine Samples A and B was the result of direct electron-hole recombination. This mechanism will be discussed further in *Chapter 8: Linear Optical Characterisation - A Discussion.*

Bibliography

[1] Chasteen, D. T. G. *Notes from Sam Houston State University* `http://www.shsu. edu/chemistry/chemiluminescence`, *accessed January 2007* .

[2] *Figure: Jablonski diagram* `http://www.shsu.edu/ chemistry/chemiluminescence/JABLON.GIF`, *accessed January 2007* .

[3] Herman, B., Frohlich, V., Lakowicz, J., Murphy, D., Spring, K., and Davidson, M. *Basic concepts in fluorescence (2005)* `http://www.olympusmicro.com/primer/techniques/fluorescence/fluorescenceintro.html`, *accessed January 2007* .

[4] Zhuravlev, K., Tyschenko, I., Vandyshev, E., Bulytova, N., Misiuk, A., Rebohle, L., and Skorupa, W. 2002 Siberian Russian Workshop on Electron Devices and Materials Proceedings (Cat. No.02EX518), p. 25–27 (IEEE, Altai, China, 2002).

[5] Bai, Z., Yu, D., Wang, J., and Zou, Y. *Materials Science & Engineering B (Solid-State Materials for Advanced Technology)* **72**, 117–120 (2000).

[6] Chen, X., Lu, Y., Tang, L., Wu, Y., Cho, B., Xu, X., Dong, J., and Song, W. *Journal of Applied Physics* **97**(1), 14913–1 (2005).

[7] Wilcoxon, J., Samara, G., and Provencio, P. *Physical Review B (Condensed Matter)* **60**(4), 2704–14 (1999).

[8] Qi, J., Belcher, A., and White, J. *Applied Physics Letters* **82**(16), 2616–18 (2003).

[9] *Photograph, Alan Ryder, NUI Galway* `http://www.nuigalway.ie/chem/AlanR/ARyderPage8.html` *accessed September 2007* .

[10] *FluoTime PicoQuant system,* `http://www.picoquant.com/_systems.htm` *accessed September 2007* .

[11] *FluoTime 200 PicoQuant system,* `http://www.picoquant.com/getfs.htm products/fluotime200/fluotime200.htm/` *accessed August 2007* .

[12] Wilcoxon, J. P. and Samara, G. A. *Applied Physics Letters* **74**(21), 3164–3166 (1999).

Chapter 8

Linear Optical Characterisation - A Discussion

8.1 Samples A and B

Pristine Samples A and B displayed strong emission centered around 400 nm, and some weaker emission in the red region. The red emission is due to quantum confinement [1, 2, 3], as per the models described in *Chapter 2*, section 2.4 *Luminescence from Silicon*, see subsections "Emission due to Quantum Confinement" and "The Effect of Oxidation on Quantum Confinement". Both Pristine Samples A and B exhibited a strong emission band in the violet region for a wide range of excitation energies, 6.20 – 3.59 eV (200 – 345 nm). This is in contrast to Pristine Samples C, D, and E, which only produced strong emission for a narrower range of high excitation energies.

In terms of sample morphology, Pristine Samples A and B contained spheres of crystalline silicon encased in oxide. This is in contrast to Pristine Samples C, D and E, which consisted of crystalline silicon nanowires encased in oxide. It is proposed

here that the strong, broad emission that occurred for a wide range of excitation energies is a consequence of the morphology of Pristine Samples A and B. The PL in the violet region could be influenced by a form of vibronic coupling between the crystal lattice and the terminating surface, silicon oxide.

Evidence of electronic sublevels resonantly coupled to surface vibrational modes has been reported for silicon nanocrystals in the strong confinement regime. It may be due to a polarisation field produced by coherent longitudinal polar vibrations. It is thought that the resulting efficient photoluminescence occurs due to the inhibition of non-radiative channels rather than the enhancement of radiative channels [4].

The diameters of the crystalline silicon spheres present in Pristine Samples A and B were too large to be influenced by quantum confinement. It may be that vibronic coupling is induced due to the spherical nature of the nanospheres which allows for increased contact between the crystalline silicon and the silicon oxide. Bulk silicon displays only weak vibronic phenomena [5, 6] whereas silicon dioxide has high ionicity [7]. Electronic states in the region of a crystalline silicon - silicon dioxide interface would be expected to exhibit properties influenced by both materials [8]. It has been shown that chain-like (silicon oxide embedded nanocrystals) nanowires exhibit a much stronger SiO_2 resonance in x-ray absorption than standard silicon nanowires. This has been attributed to a larger ratio of silicon oxide atoms to elemental silicon atoms in the chainlike wires [9].

In order to establish the nature of the emission in the violet region for Pristine Samples A and B, an additional technique was carried out. Lifetime measurements were performed on Pristine Sample A for emission in the violet region in order to establish a lifetime for the emitting species. Three lifetimes on the nano-scale were detected, which is consistent with direct electron-hole recombination [10]. It is pro-

posed here that this direct recombination is a consequence of vibronic coupling between the crystalline spheres and the oxide shell. Pristine Sample A's most intense emission occurred at 3.22 eV (384 nm), and Pristine Sample B exhibited a strong emission peak at 3.10 eV (400 nm). The broad emission could therefore arise from enhancement of the vibronically coupled $\Gamma_{25} - \Gamma_{15}$ (3.4 eV) transition.

Oxidised Samples A and B emitted most intensely in the ultra-violet. This emission only occurred for excitation at high energies. It is likely that upon oxidation of the pristine samples, the vibronically coupled state that existed breaks down. This could occur either through reduction in the lattice size to such an extent that its vibronic component is no longer strong enough to couple efficiently with the oxide layer, or through the destruction of the regularity of the lattice by the encroaching oxide.

For the oxidised samples, the most intense PL occurred at wavelengths corresponding to the direct energy gaps of bulk silicon, and is therefore the result of quantum confinement [11]. Oxidised Sample A displayed peaks at 352 nm and 294 - 288 nm (3.52 and 4.22 - 4.31 eV) and Oxidised Sample B displayed peaks at 350, 297 and 287 nm (3.54, 4.18 and 4.32 eV). This corresponds to direct electron hole recombination at the $\Gamma_{25} - \Gamma_{15}$ (3.4 eV) and $X_4 - X_1$ (4.4 eV) points. This quantum confined emission is the result of increased oxidation, as per the model described in *Chapter 2*, section 2.4 *Luminescence from Silicon*, subsection "The Effect of Oxidation on Quantum Confinement". PL intensity in the red region also increased upon oxidation. This red emission is also due to quantum confinement [1, 2, 3].

A broad band of blue – green emission occurred for the oxidised samples, which is due to self-trapped excitons located at defect centres in the SiO_x/Si interface, or in the amorphous silicon oxide layer [12, 2].

In summary, the emission for Pristine Samples A and B was dominated by strong emission in the violet region. Lifetime measurements showed that this emission was due to the direct recombination of excitons. There was also some weak emission in the red region, due to quantum confinement [1, 2, 3].

Upon oxidation, the strong emission in the violet region decreased greatly. The PL became dominated by emission at the direct transition energies of bulk silicon. Hence increased oxidation led to an increase in PL due to quantum confinement [11, 1, 2, 3], most likely through the model described in *Chapter 2*, section 2.4 *Luminescence from Silicon*, subsection "The Effect of Oxidation on Quantum Confinement".

The encroaching oxide also lead to the production of emission in the blue – green region due to self-trapped excitons [12, 2]. The PL results were in agreement with the absorption results, which showed weak evidence of quantum confinement for the pristine samples, but stronger evidence for the oxidised samples.

8.2 Sample C

The absorption spectra presented in Chapter 6 showed some evidence of quantum confinement in both Pristine and Oxidised Sample C due to the red-shift of the $\Gamma_{25} - \Gamma_{15}$ absorption onset [11, 13, 14]. The PL data indicated the presence of strong quantum confinement effects in Pristine Sample C, and weaker quantum confined effects in the oxidised sample.

Pristine Sample C exhibited an emission band in the blue – green region due to self-trapped excitons [12, 2]. It also displayed a peak in emission at 350 nm (3.54 eV) which is attributed to direct recombination at $\Gamma_{25} - \Gamma_{15}$ due to quantum confinement [11]. The dominant emission for the pristine sample occurred in the red region. This

intense emission is also due to quantum confinement [1, 2, 3].

Oxidised Sample C exhibited its dominant emission in the violet – blue region. Emission in the red region was negligible. The peak that had occurred at 350 nm for the pristine sample became a shoulder for the oxidised sample. The PL intensity at 350 nm was greatly reduced relative to the blue – green emission.

In summary, Pristine Sample C displayed emission due to self-trapped excitons, but was dominated by emission in the red region, which was due quantum confinement [1, 2, 3]. Evidence of quantum confinement also included emission at an energy corresponding to direct recombination in bulk silicon in the ultra-violet region [11].

Upon oxidation, it appears that the nanocrystallites that had been present and which were the source of the quantum confined emission, were greatly diminished (see *Chapter 2*, section 2.4 *Luminescence from Silicon*, subsection "The Effect of Oxidation on Quantum Confinement"). Emission due to quantum confinement in the red region became negligible, and the peak that had occurred at the $\Gamma_{25} - \Gamma_{15}$ transition energy in the pristine sample became a shoulder with greatly reduced intensity. The emission for Oxidised Sample C was dominated by surface states and self-trapped excitons, with a greatly reduced component arising from quantum confinement.

8.3 Sample D

The absorption spectra for Pristine and Oxidised Sample D indicated the possible presence of quantum confinement effects. However, the PL results indicated that the emission was dominated by oxide induced effects, and a measurable component did not arise due to quantum confinement.

The PL spectra for Pristine and Oxidised Sample D were very similar. No discern-

able alteration occurred to the PL spectrum of the sample upon oxidation. Strong emission occurred in the violet – green region, due to self-trapped excitons and surface states [12, 2].

In summary, the emission for Pristine and Oxidised Sample D was not discernably different. The emission for both samples was dominated by self-trapped excitons and surface states [12, 2]. There was no apparent contribution from quantum confinement effects.

8.4 Sample E

The PL data showed the presence of strong quantum confinement effects in Pristine Sample E, and weaker quantum confined effects in the oxidised sample.

Pristine Sample E exhibited an emission band in the blue – green region due to self-trapped excitons [12, 2]. Pristine Sample E also displayed a peak in emission at 352 nm (3.52 eV) which corresponds to direct recombination at $\Gamma_{25} - \Gamma_{15}$ due to quantum confinement [11]. The dominant emission for the pristine sample occurred at 287 nm (4.32 eV) which corresponds to direct recombination at $X_4 - X_1$. Emission also occurred in the red region, and is also due to quantum confinement [1, 2, 3].

Upon oxidation, self-trapped excitons became the dominant emission species [12, 2]. Emission in the red region and at the direct recombination energies of bulk silicon became less intense relative to emission in the blue – green region.

In summary, Pristine Sample E displayed some emission due to self-trapped excitons [12, 2]. The emission was dominated by quantum confinement effects. Evidence of quantum confinement included intense emission at energies corresponding to direct recombination in bulk silicon [11], and emission in the red region [1, 2, 3].

Upon oxidation, emission due to quantum confinement in the red region became negligible, and the peaks that had occurred at the direct transition energies in the pristine sample were greatly reduced. The emission for Oxidised Sample E was dominated by self-trapped excitons, with a greatly reduced component arising from quantum confinement. This is in agreement with the model described in *Chapter 2*, section 2.4 *Luminescence from Silicon*, subsection "The Effect of Oxidation on Quantum Confinement".

8.5 Absorption at $X_4 - X_1$

It has been reported in literature that quantum confinement causes a blue-shift of the $\Gamma - X$ ($E = 1.1$ eV) transition, a red-shift of the $\Gamma_{25} - \Gamma_{15}$ ($E = 3.4$ eV) transition [11, 13, 14], and a blue-shift of the $X_4 - X_1$ ($E = 4.4$ eV) transition [13, 14]. It became apparent during the course of this study that the occurrence of additional features such as peaks and shoulders in the energy region just above the $X_4 - X_1$ transition is indicative of extensive oxidation effects rather than quantum confinement.

A blue-shift of the absorption at $X_4 - X_1$ along with some absorption shoulders were apparent in only one of the pristine samples, namely Pristine Sample E. Pristine Sample E exhibited strong emission in the blue – green region, and was therefore strongly influenced by oxide effects (self-trapped excitons occur more frequently in regions of heavy oxidation and defects). What could be interpreted as blue-shift of the $X_4 - X_1$ absorption onset along with additional features occurred for Oxidised Samples A, B, D and E. Conclusions cannot be drawn from studying Oxidised Samples A and B alone. Upon oxidation their blue – green oxide related emission became intense, but there were also contributions from quantum confinement.

The study of the PL from Oxidised Samples D and E elucidates the situation. The PL line shape for Pristine and Oxidised Sample D were not discernibly different from each other, with emission dominated by self-trapped excitons. However, the oxidised sample displayed additional absorption peaks in the blue-shifted $X_4 - X_1$ region.

Pristine Sample E produced blue – green emission which arose from self-trapped excitons [12, 2], and emission due to quantum confinement [1, 2, 3]. The absorption spectrum contained some shoulders in the blue-shifted $X_4 - X_1$ region. The PL from Oxidised Sample E was dominated by self-trapped excitons, with a greatly diminished component arising due to quantum confinement. The corresponding absorption spectrum contained a series of peaks in the blue-shifted $X_4 - X_1$ region.

In summary, the common factor linking all of the samples which produced absorption features above the $X_4 - X_1$ transition energy was emission that was strongly influenced by self-trapped excitons, not quantum confinement effects as has been reported in literature [13, 14]. Hence, analysis of the "blue-shifted $X_4 - X_1$" absorption region could possibly be used to infer the extent of oxidation in a silicon sample.

8.6 Summary

The absorption and PL spectra from each sample in a pristine and oxidised state were recorded and studied. The observed emission species included quantum confinement, surface states and self-trapped excitons. Pristine Samples A and B displayed broad emission for a wide range of exciton energies, which was attributed to a form of vibronic coupling.

It became apparent that oxidation of the pristine samples did not just lead to an increase in oxide effects such as self-trapped excitons. Some of the oxidised samples

displayed emission due to quantum confinement. This behaviour is in agreement with the model described in *Chapter 2*, section 2.4 *Luminescence from Silicon*, subsection "The Effect of Oxidation on Quantum Confinement".

It had been reported in literature that quantum confinement causes a blue-shift of the $X_4 - X_1$ ($E = 4.4$ eV) transition [13, 14]. It became apparent during the course of this study that the occurrence of additional features such as peaks and shoulders in the energy region just above the $X_4 - X_1$ transition is indicative of extensive oxidation effects e.g. self-trapped excitons, rather than quantum confinement (which does not occur in the "extensively" oxidised regime, see *Chapter 2*, section 2.4 *Luminescence from Silicon*, subsection "The Effect of Oxidation on Quantum Confinement").

Bibliography

[1] Zhuravlev, K., Tyschenko, I., Vandyshev, E., Bulytova, N., Misiuk, A., Rebohle, L., and Skorupa, W. 2002 Siberian Russian Workshop on Electron Devices and Materials Proceedings (Cat. No.02EX518), p. 25–27 (IEEE, Altai, China, 2002).

[2] Bai, Z., Yu, D., Wang, J., and Zou, Y. *Materials Science & Engineering B (Solid-State Materials for Advanced Technology)* **72**, 117–120 (2000).

[3] Chen, X., Lu, Y., Tang, L., Wu, Y., Cho, B., Xu, X., Dong, J., and Song, W. *Journal of Applied Physics* **97**(1), 14913–1 (2005).

[4] Sa'ar, A., Reichman, Y., Dovrat, M., Krapf, D., Jedrzejewski, J., and Balberg, I. *Nano Letters* **5**(12), 2443–2447 (2005).

[5] Kleverman, M., Grimmeiss, H., Litwin, A., and Janzen, E. *Physical Review B* **31**(6), 3659–66 (1985).

[6] Chantre, A. and Bois, D. *Physical Review B (Condensed Matter)* **31**(12), 7979–88 (1985).

[7] Engstrom, O. and Grimmeiss, H. *Semiconductor Science and Technology* **4**(12), 1106–15 (1989).

[8] Gwyn, C. *Journal of Applied Physics* **40**(12), 4886–92 (1969).

[9] Sun, X., Wong, N., Li, C., Lee, S., and Sham, T. *Journal of Applied Physics* **96**(6), 3447–51 (2004).

[10] Wilcoxon, J. P. and Samara, G. A. *Applied Physics Letters* **74**(21), 3164–3166 (1999).

[11] Wilcoxon, J., Samara, G., and Provencio, P. *Physical Review B (Condensed Matter)* **60**(4), 2704–14 (1999).

[12] Qi, J., Belcher, A., and White, J. *Applied Physics Letters* **82**(16), 2616–18 (2003).

[13] Holmes, J., Ziegler, K., Doty, R., Pell, L., Johnston, K., and Korgel, B. *Journal of the American Chemical Society* **123**(16), 3743–3748 (2001).

[14] Rama Krishna, M. and Friesner, R. *Journal of Chemical Physics* **96**(2), 873–7 (1992).

Chapter 9

Conclusions

9.1 Results

Characterisation of the morphological and optical properties of various silicon nanowire structures was carried out. Stable suspensions of each nanowire type were obtained by the sedimentation method described by Nicolosi *et al.* [1], which allowed detailed three dimensional photoluminescence and z-scan based non-linear characterisation to be carried out.

Non-linear characterisation revealed that oxide coated silicon nanoclusters in an IPA suspension display good optical limiting properties, with nanowires that contain spherical inclusions (samples A and B) displaying enhanced optical limiting capabilities compared to that of standard, cylindrical silicon nanowires. The effective imaginary χ^3 values calculated for the samples were comparable to some optically limiting porphyrin based solutions. It is unlikely that the optical limiting arises from photoinduced refractive index mismatch, as previously reported [2]. Scattering induced optical limiting was apparent, and is attributed to laser induced breakdown of

the silicon oxide outer shell.

Absorption spectroscopy was carried out on the samples, in the pristine and oxidised states. Evidence of quantum confinement effects were exhibited by the samples in varying degrees. This evidence came in the form of a blue-shift of the $\Gamma - X$ onset energy and a red-shift of the $\Gamma_{25} - \Gamma_{15}$ transition energy [3, 4, 5]. The occurrence of additional features such as peaks and shoulders in the energy region above the $X_4 - X_1$ transition is indicative of extensive oxidation effects, rather than quantum confinement as reported elsewhere [4, 5].

A detailed photoluminescence study revealed emission due to a number of different mechanisms. Emission species included quantum confinement [6, 7, 8, 3], and effects such as surface states and self trapped excitons which occur at defect centres located at the SiO_x/Si interface or in the amorphous silicon oxide layer [9, 7]. Pristine Samples A and B displayed broad emission for a wide range of exciton energies, which lifetime measurements showed to be the result of direct electron-hole recombination. It is possible that this effect arose due to the spherical nature of the nanocrystals and the high ionisity of the silicon oxide shell producing a form of vibronic coupling [10, 11, 12]. Oxidation of the pristine samples lead to an increase in oxide effects such self-trapped excitons [9, 7], with some of the oxidised samples displaying emission due to quantum confinement [6, 7, 8, 3]. It is likely that this emission arose due to the encroaching oxide forming isolated crystalline grains, capable of undergoing quantum confinement (see *Chapter 2*, Section 2.4 *Luminescence from Silicon*, subsection "The Effect of Oxidation on Quantum Confinement").

9.2 Future work

9.2.1 Optical Limiting

The nanowires that contained spherical inclusions (samples A and B) displayed some very interesting features that may lead to real-world applications. One such feature is good optical limiting capabilities. The self-healing ability of solution based optical limiters makes them auspicious materials for real world applications, such as the protection of optical sensors from intense laser sources. As the optical limiting mechanism for these samples seems to arise mainly from a surface effect, i.e. non-linear scattering due to laser induced breakdown of the silicon oxide shell, optical limiting may endure even after oxidation of the sample has occurred. A simultaneous high resolution transmission electron microscopy study and z-scan characterisation carried out at regular intervals would elucidate any changes that occur to the optical limiting capabilities of the samples as a function of oxidation.

9.2.2 Biological Applications

Samples A and B exhibited strong broad emission in the violet region, for a wide range of excitation energies. A detailed three dimensional photoluminescence study carried out on a larger number of similar structures of various dimensions may be of importance for biological applications. The nanostructures studied here satisfy the conditions needed for use in the human body, i.e. they produce strong photoluminescence with a fast radiative recombination rate; the photoluminescence can be produced in water based solution; and as the nanospheres consist of silicon with a silicon oxide coating, they are non-toxic [13].

Nanomaterials are currently being studied for use in cell imaging and for targeting the destruction of cells. Some nanomaterials can be functionalised to interact with specific biological agents. The ability of some nanomaterials to fluoresce and/or absorb heat makes them auspicious components for the detection and destruction of diseased cells, such as cancer cells. One notable glycan is the Thomsen-Freidenreich disaccharide. This is readily detectable in 90% of all primary human carcinomas and their metastases [13]. Glycans can be exploited for medical imaging. It is possible to encapsulate a luminescent structure with target-specific glycans, which permits efficient imaging of the tissue to which the glycans bind with high affinity. The SiO_2 surface can be modified to attach to this glycan [13].

The majority of fluorescing nanodots which have so far been studied by other groups have diameters in the region of 10 nm or less, as the PL produced is usually due to a purely quantum confined effect, hence the need for small dot size with diameters less than the Bohr radius of the material being used [14]. This does not necessarily make the quantum dots useful for *in vivo* detection of cancerous sites.

The efficient delivery of quantum dots to the human body is problematic. Intravascular injection is very attractive because it offers the chance to detect every tumor in a patient's body [15]. Most solid tumors contain strongly permeable, badly organised vascular networks [16]. The use of small quantum dots in the human will likely be inefficient, as the vast majority of dots will pass through the body without attaching to a cancerous site.

Due to extravasation from the blood circulation, nanoparticles in the size range 60 – 400 nm preferentially accumulate within the solid tumors [17]. This is also called the Enhanced Permeability and Retention Effect [18]. Sample B contained photoluminescing nanospheres with an average diameter of 70 nm. Hence Sample B

contains nanospheres which may be an ideal candidate for intravascular injection. In summary, Sample B is the most promising candidate for biological application. It contains nanospheres which produce strong PL in the visible; have a fast radiative recombination rate; are water soluble; are non-toxic to humans; are functionalisable with cancer detecting glycons; and are of a size suitable for delivery into the human body by intravascular injection. It is therefore a possible candidate for use as a fluorescent marker in the human body.

Bibliography

[1] Nicolosi, V., Vrbanic, D., Mrzel, A., McCauley, J., O'Flaherty, S., McGuinness, C., Compagnini, G., Mihailovic, D., Blau, W. J., and Coleman, J. N. *Journal of Physical Chemistry B* **109**(15), 7124–7133 (2005).

[2] Joudrier, V., Bourdon, P., Hache, F., and Flytzanis, C. *Applied Physics B (Lasers and Optics)* **B70**(1), 105–9 (2000).

[3] Wilcoxon, J., Samara, G., and Provencio, P. *Physical Review B (Condensed Matter)* **60**(4), 2704–14 (1999).

[4] Holmes, J., Ziegler, K., Doty, R., Pell, L., Johnston, K., and Korgel, B. *Journal of the American Chemical Society* **123**(16), 3743–3748 (2001).

[5] Rama Krishna, M. and Friesner, R. *Journal of Chemical Physics* **96**(2), 873–7 (1992).

[6] Zhuravlev, K., Tyschenko, I., Vandyshev, E., Bulytova, N., Misiuk, A., Rebohle, L., and Skorupa, W. 2002 Siberian Russian Workshop on Electron Devices and Materials Proceedings (Cat. No.02EX518), p. 25–27 (IEEE, Altai, China, 2002).

[7] Bai, Z., Yu, D., Wang, J., and Zou, Y. *Materials Science & Engineering B (Solid-State Materials for Advanced Technology)* **72**, 117–120 (2000).

[8] Chen, X., Lu, Y., Tang, L., Wu, Y., Cho, B., Xu, X., Dong, J., and Song, W. *Journal of Applied Physics* **97**(1), 14913–1 (2005).

[9] Qi, J., Belcher, A., and White, J. *Applied Physics Letters* **82**(16), 2616–18 (2003).

[10] Engstrom, O. and Grimmeiss, H. *Semiconductor Science and Technology* **4**(12), 1106–15 (1989).

[11] Gwyn, C. *Journal of Applied Physics* **40**(12), 4886–92 (1969).

[12] Sun, X., Wong, N., Li, C., Lee, S., and Sham, T. *Journal of Applied Physics* **96**(6), 3447–51 (2004).

[13] Warner, J. H., Hoshino, A., Yamamoto, K., and Tilley, R. D. *Angewandte Chemie - International Edition* **44**(29), 4550–4554 (2005).

[14] Derfus, A. M., Chan, W. C. W., and Bhatia, S. N. *Nano Letters* **4**(1), 11–18 (2004).

[15] Jain, P., H., E.-S. I., and El-Sayed, M. A. *Nanotoday* **2**(1), 18–29 (2007).

[16] Dvorak, H. F., Nagy, J. A., Dvorak, J., and Dvorak, A. M. *American Journal of Pathology* **133**(1), 95–109 (1988).

[17] Ishida, O. *International Journal of Pharmacology* **190**, 49 (1999).

[18] Maeda, H. *Advances in Enzyme Regulation* **41**(1), 189–207 (2001).